High-pressure Synthesis and Crystal Chemistry of Multicomponent Transition Metal Nitride and Phosphide

多成分系の金属窒化物及び金属リン化物の高圧合成と結晶化学

A Thesis Submitted to Nagoya University
for the Degree of
Doctor of Science

by

Chung-Ching CHANG

Department of Materials Physics
Graduate School of Engineering
Nagoya University
2024

Acknowledgements

First and foremost, I would like to express my sincere gratitude to Professor Masashi Hasegawa, Professor Masao Tabuchi, Department of Materials Physics, Graduate School of Engineering, Nagoya University, Professor Chikara Ohtsuki, Department of Materials Chemistry, Graduate School of Engineering, Nagoya University, and Associate Professor Ken Niwa, Department of Materials Physics, Graduate School of Engineering, Nagoya University, for all their help, advise, support, and tutelage during the course of my PhD.

I would like to express my sincere thanks to Assistant Professor Takuya Sasaki, and Dr. Nico Alexander Gaida, Department of Materials Physics, Graduate School of Engineering, Nagoya University, for their mentorship and assistance. My gratitude extends to Professor Shunsuke Muto, Advanced Measurement Technology Center, Institute of Materials and Systems for Sustainability, Nagoya University, for the help in the transmission electron microscope analysis. Mr. Tatsuo Hikage of R-AXIS VII, X-ray supervisor in Nagoya University for the assistance of XRD usage.

I would like to thank my dear lab-mate and friend Shuto Asano for walking through all the happiness and tears of the doctoral course together. Special thanks to all my junior colleagues who decorated my life in Nagoya University. Also, to my friends on the other side of the sea, gang-wen, xie-xie, thanks in full hearty.

Finally, I give my deep gratefulness to my beloved parents for all the support and encouragement.

Contents

Chapter 1 General introduction

Recent advancements in materials science have brought attention to multicomponent materials that incorporate distinct element species within a single structure. The conventional method of doping a small amount of an element into a base material has long been the standard in material design and development. This approach of enhancing material property has made significant contributions to the science community. Examples include the development of $ln_xGa_{1-x}As$ or the $In_{1-x}Ga_xAs_yP_{1-y}$ [1], derived from solid solution alloys GaAs, InAs, InP, and GaP. Also, the design and research of superconducting copper oxide $La_{2-x}Sr_xCuO_4$（LSCO） solid solution based on so called perovskite-related copper oxide La_2CuO_4 [2].

However, this methodology primarily focuses on the 'corner' of the phase diagram, as illustrated in Figure 1-1. An alternative approach proposed by Cantor et al., involves moving from the 'corner' toward the 'center' of the phase diagram, exploring a field that is relatively less studied. This 'unconventional' composition region, i.e., the equimolar multicomponent materials had been presented to be useful in synthesizing materials with outstanding properties. Introduced by Cantor et al., the multicomponent alloy $Cr_{20}Co_{20}Fe_{20}Mn_{20}Ni_{20}$ demonstrate high strength and high toughness properties superior to most conventional alloys [3], attributed to a 'multicomponent effect'. This approach introduces a 'new material design' methodology by combining an equimolar number of different elements. Yeh et al. attributed this design process and phenomenon to an 'entropy stabilized' effect [4]. Despite ongoing debates about this concept, this category of material is commonly referred to as either "high-entropy" alloy or “entropy-stabilized” alloy.

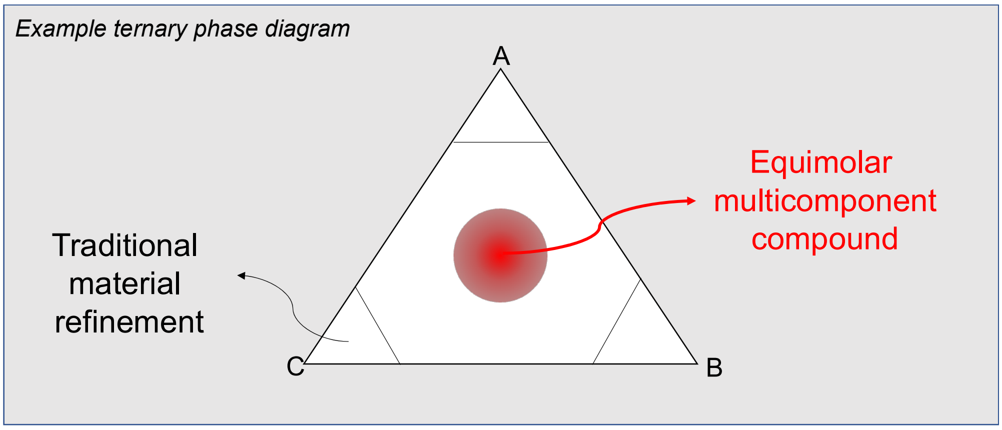

Figure 1-1 The example of a ternary phase diagram showing how ‘new materials design’ is different from traditional material refinement.

Meanwhile, the alloy system is limited to the structure types of simple cubic, BCC, and FCC structures. There has been significant interest in exploring the application of this design concept to ceramic materials, given that ceramics can adopt various structures such as rock-salt, spinel, and perovskite structures, etc. These diverse structures hold great potential for scientific and engineering applications. In 2015, Rost et al. successfully demonstrate that this idea of designing new alloy can be expanded to oxides [5]. Since then, there has been extensive exploration of new compounds within the equimolar multicomponent ceramic family.

Within the extent of exploring multicomponent ceramics around the center of the phase diagram, numerous synthesis processes have been established. Conventional sintering process, spark plasma sintering, physical vapor deposition are some examples. However, the synthesis method using high-pressure technique are less reported.

High-pressure technique offers several advantages. Due to the nature of the process, the sample is compressed to a high-density condition in which atoms are forced to get close together that is effective for solid state reactions. The sample is sealed inside cell parts or pressure chamber during synthesis, allowing reactions among starting materials with different melting points. Additionally, this technique enables the synthesis of materials with high vapor-pressure. Consequently, high-pressure technique favors chemical reactions among elements with different characteristics, making it suitable for synthesizing multicomponent ceramics. Nitrides and phosphides are particularly of interest due to their superior material properties and the synthesis challenges under ambient pressure. Their details on these will be introduced in later chapters.

Nevertheless, sample size in high-pressure experiments is limited, resulting in fewer product amounts compared to ambient pressure synthesis. Consequently, analysis and characterization of the product are confined to techniques that do not require a large sample. At the same time, the search for multicomponent ceramic using high-pressure technique is an area that is largely unexplored. The variable concerning pressure in the synthesis process makes finding the optimal synthesis conditions more challenging, with no guarantee of synthesizing single-phase multicomponent product. Given these challenges, an accurate evaluation measurement method is required, with synchrotron X-ray diffraction (XRD) technique being the most suitable.

Synchrotron XRD technique is capable of measuring small samples, including those with low symmetry structures and impurity inclusion. For example, a sample with a main phase of monoclinic symmetry is shown in Figure 1-2. Accurate lattice and volume information can be retrieved from the XRD pattern. Furthermore, the measurement can be done at various temperature and pressure conditions. *In-situ* low-temperature and compression measurements can be used to calculate thermal expansion and compression behaviors.

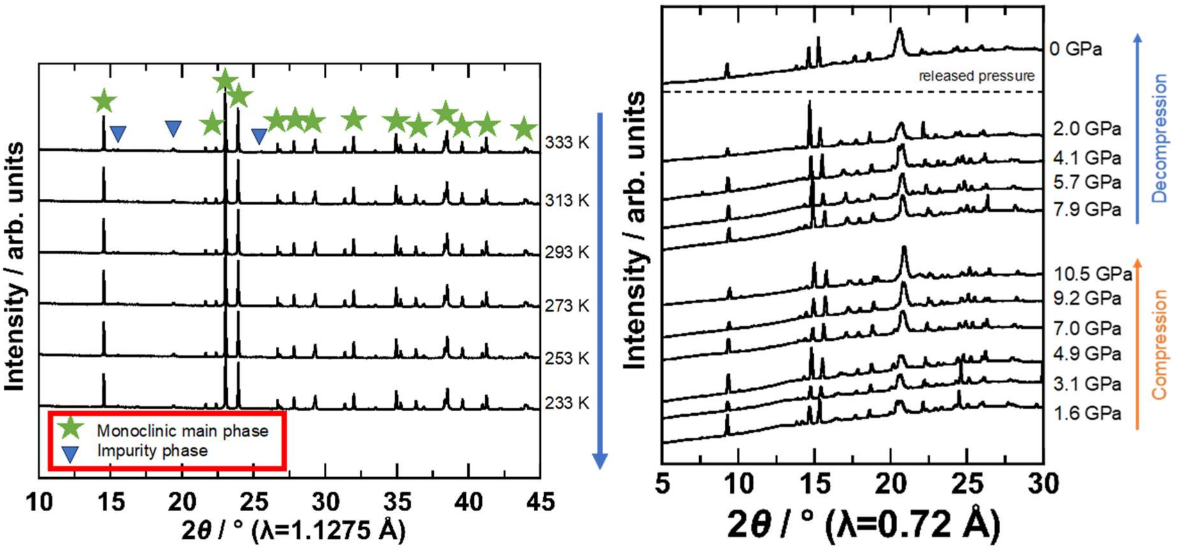

Figure 1-2 Example *in-situ* low-temperature (left) and compression (right) synchrotron XRD pattern of a monoclinic sample. Synchrotron XRD technique can measure complicated structure even with the presence of impurity phase.

Thermal expansion and compression behavior are fundamental material properties crucial for engineering applications. For instance, significant differences in thermal expansion between materials joined together can lead to catastrophic failure in electronic components, jet turbine engines, and other applications. The compressibility of materials is closely related to hardness, a critical factor in the performance of hard materials such as drills and machining tools.

Given these considerations, the objective of this thesis is to synthesize equimolar multicomponent ceramics using high-pressure techniques and establish the optimal synthesis conditions. Furthermore, in evaluating the synthesized multicomponent ceramics, the multicomponent effect is explored by comparing the experimental values with the weighted average values of the constituent endmembers. The multicomponent effect on lattice parameters, coefficient of thermal expansion (CTE), and bulk modulus is examined.

Chapter 2 Experimental procedure

2.1 High-pressure technique

In this thesis, high-pressure synthesis was conducted using a 250-ton DIA-type cubic multi-anvil large volume press (LVP), as depicted in Figure 2-1. The LVP has a height of about 2 meters. The sample container, or cell part, is illustrated in Figure 2-2, with dimensions of about 8×8×8 mm^3. It is hand-crafted for each experiment. The BN capsule serves as the container for the sample. Insulated heating was achieved using carbon. Finally, the cell part is compressed by anvils in six directions simultaneously.

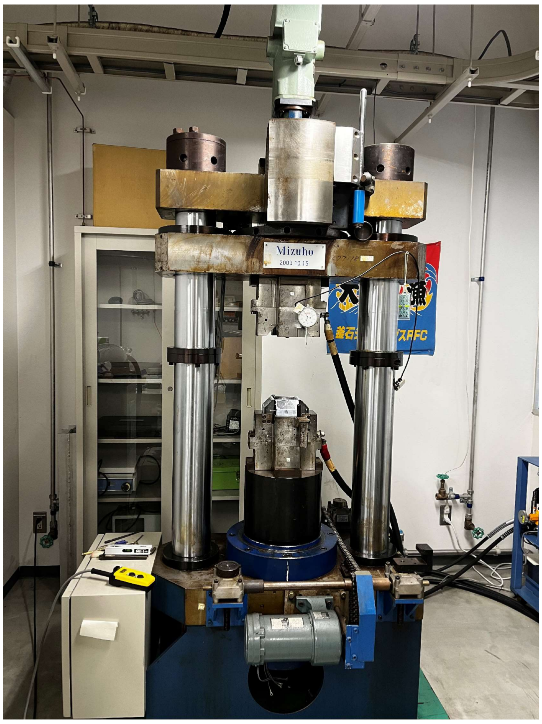

Figure 2-1 250-ton DIA-type cubic multi-anvil large volume press.

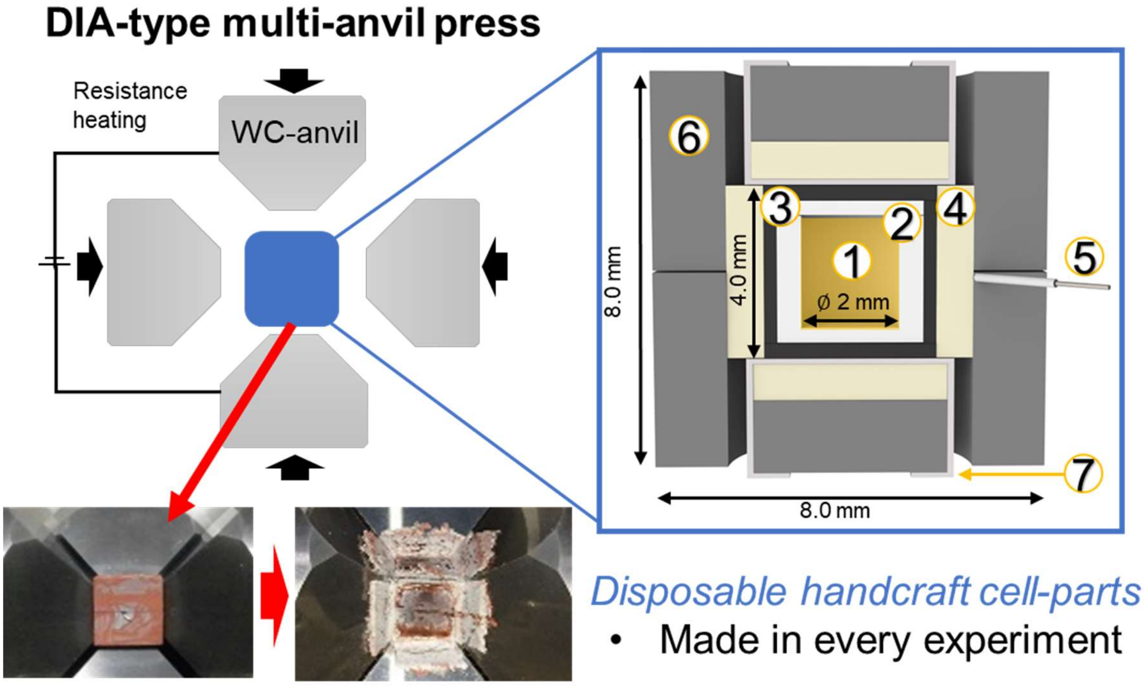

Figure 2-2 Schematic view of the DIA-type multi-anvil press with the handcraft cell-parts for the high-pressure experiment. The cell-parts are being compressed by the anvils from 6-directions simultaneously. The picture in the bottom left is the actual experiment before compression (left) and after compression (right). The cell-part is constructed by (1) sample chamber, (2) *h*-BN, (3) carbon resistance heater, (4) ZrO_2 thermal insulation, (5) R-type thermocouple, (6) pyrophyllite pressure medium, and (7) Mo foil electrode.

In the compression experiments, a diamond anvil cell (DAC) was used (Figure 2-3). The sample chamber used a SUS gasket with a pre-indented hole (~160 μm in diameter). The diamonds used had a culet size of 350 μm. The pressure medium was liquid mixture of methanol/ethanol (4:1) which enables quasi-hydrostatic conditions up to 10 GPa [6]. Ruby was employed for pressure determination [7].

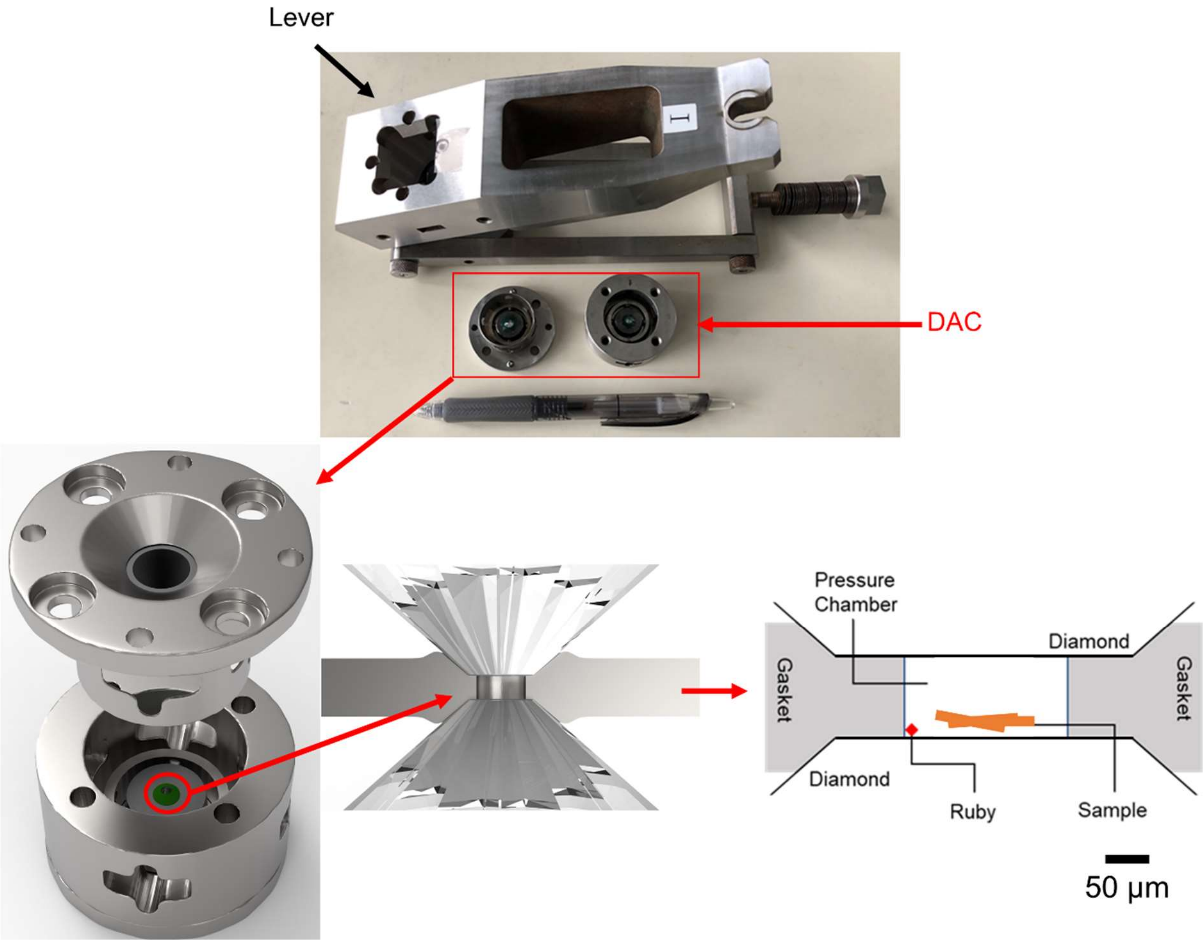

Figure 2-3 The schematic figure of diamond anvil cell.

2.2 Starting materials

As will be introduced in the later chapters, the starting materials involved in this study are separated into multicomponent oxide, nitride, and phosphides for discussion. The starting materials are made using the following commercial chemical products as listed in Table 2-1, Table 2-2, and Table 2-3.

Table 2-1 The chemicals used in multicomponent oxide experiments.

Chemical	Maker	Purity	Form
MgO	Rare Metallic Co., Ltd.	99.99%	Powder
NiO	Wako Pure Chemical Industries Ltd.	99.90%	Powder
CuO	Kojundo Chemical Laboratory. Co., Ltd.	99.99%	Powder
CoO	Kojundo Chemical Laboratory. Co., Ltd.	99.90%	Powder
ZnO	Rare Metallic Co., Ltd.	99.999%	Powder

Table 2-2 The chemicals used in multicomponent nitride experiments.

Chemical	Maker	Purity	Form
V	Mitsuwa Chemicals Co., Ltd.	99.90%	Piece
Cr	Nilaco Co.	99.90%	Chunk
Nb	Hiranoseizaemon Shoten Co., Ltd.	99.90%	Piece
Mo	Nilaco Co.	99.95%	Chunk
Ta	Kojundo Chemical Laboratory. Co., Ltd.	99.90%	Chunk
NH_4Cl	Sigma-Aldrich	99.99%	Powder

Table 2-3 The chemicals used in multicomponent phosphide experiments.

Chemical	Maker	Purity	Form
V	Japan Metal Service Co., Ltd.	99+%	Powder
Cr	Kojundo Chemical Lab. Co., Ltd.	99.9%	Powder
Mo	Kojundo Chemical Lab. Co., Ltd.	99.9%	Powder
Mn	Kojundo Chemical Laboratory. Co., Ltd.	99.9%	Powder
V	Mitsuwa Chemicals Co., Ltd.	99.90%	Piece
Cr	Nilaco Co.	99.90%	Chunk
Mo	Kojundo Chemical Lab. Co., Ltd.	99.90%	Chip
Mn	Nilaco Co.	99.999%	Chunk
Red phosphorus	Kojundo Chemical Laboratory. Co., Ltd.	99.99%	Powder

2.3 Characterizations

2.3.1 XRD and SEM-EDS

The synthesized products were first characterized by powder X-ray diffraction (XRD) pattern taken at Nagoya University. RINT-2500, RIGAKU Corp., with Cu radiation was used. The voltage of X-ray tube and current are 50 kV, and 160 mA, respectively. Due to the sample size, part of the product was determined using RAXIS VII, RIGAKU Corp., with a Cu radiation. The voltage of X-ray tube and current are 45 kV, and 45 mA, respectively. The two-dimensional patterns were converted to one-dimensional profiles using Fit2D program [8,9].

Synchrotron XRD patterns were taken at Aichi Synchrotron Radiation Center. The ambient condition (room temperature and ambient pressure) patterns were taken at BL5S2, with a monochromatic wavelength of $\lambda = 1.127$ Å pre-calibrated using CeO_2 standard before measurement. The *in-situ* low-temperature XRD patterns were also taken at BL5S2. The *In-situ* cooling and heating were done using a cooling system (airflow of nitrogen gas). The sampling temperature was pre-calibrated using thermal couple and determined from the relationship between gas flow nozzle point and the sampling point. The sample was first cooled down to 113 K and data were collected at intervals of 20 K from 113 K to 333 K. The heating speed was 50 K/min, and the sample was kept at the temperature for 120 seconds before each data measurements.

In-situ compression experiments were mainly conducted in Aichi Synchrotron

Radiation Center, BL2S1 (λ = 0.72 Å) [10]. Compression experiments were performed using LVP synthesized products and reloaded into a DAC (setup described in Chapter 2.1). The measurement time was set to $t = 300$ s. Camera length was calibrated by using CeO_2 standard. Two-dimensional diffraction profiles were converted to one-dimensional profiles using IPAnalyzer [11].

Part of the *in-situ* high-pressure experiments were conducted using laboratory *in-situ* Mo-radiation X-ray with voltage of X-ray tube and current of 60 kV, and 300 mA, respectively. The measurement time was about 12 hours per pattern. The camera length was calibrated using CeO_2 standard. The two-dimensional patterns were converted to one-dimensional profiles using Fit2D program [8,9].

XRD pattern peak fittings were performed by using PDIndexer software [11]. Crystal structures refinements were done by Rietveld analysis using the RIETAN-FP program [12]. Crystal structures are illustrated with VESTA [13].

Product surface morphology and element constituents were analyzed by scanning electron microscopy and energy dispersive X-ray spectroscopy (FlexSEM 1000 II, Hitachi High-Tech Corporation, accelerating voltage: 15 kV). A scanning transmission electron microscope (JEM-ARM200 STEM, accelerating voltage: 200 kV) was used to study the crystal structure as well as the atomic-scale homogeneity of the products.

2.3.2 Weighted average method

The weighted average method is employed for the discussion of the individual constituent effect in the multicomponent compounds. The lattice parameter of multicomponent compounds can be approximated by following equation:

$$a_{comp.} = \sum_{i=1}^{N} c_{EDS,i} a_{idividual\ compound} \qquad \text{Equation 1}$$

Where the individual component c (constituent) has a contribution to the total lattice parameter a.

2.3.3 Coefficient of thermal expansion

When calculating the coefficient of thermal expansion (CTE), it is typical for most metals and ceramics at elevated temperatures (e.g., above 298 K) to exhibit a linear behavior that can be effectively estimated using straightforward linear equations. At low temperatures (e.g., below 298 K) the CTE tends to change more and follows a curved trend because theoretically the CTE will become 0 at 0 K [14,15]. Thus, in this study, the coefficient of thermal expansion (CTE) is calculated by using a second-degree polynomial [16]:

$$V(T) = V\,(1 + a_1 T + a_2 T^2) \qquad \text{Equation 2}$$

Where parameters V, a_1, and a_2 can be determined by fitting experiment volume-temperature data. Then, from the definition of thermal expansion, $\alpha(T)$ (CTE) is:

$$\alpha(T) = \frac{1}{V(T)}\left(\frac{\partial V}{\partial T}\right) \qquad \text{Equation 3}$$

From Equation 2 and Equation 3, the volumetric CTE at each experiment temperature can be calculated, and similarly, the CTE for each axis and bond angle can be calculated in the same way.

2.3.4 Bulk modulus

The zero-pressure bulk modulus is calculated by fitting the second-order Birch-Murnaghan equation of state (BM-EOS, Equation 4). The fitting parameters are evaluated using the relation between zero-pressure bulk modulus (K_0) and its zero-pressure derivative, the normalized pressures F in Equation 5 as a function of Eulerian strain f in Equation 6 are calculated and plotted for each compression experiment.

$$P = \frac{3K_0}{2}\left(\frac{V}{V_0}\right)^{-\frac{5}{3}}\left[\left(\frac{V}{V_0}\right)^{-\frac{2}{3}} - 1\right]$$

Equation 4

$$F = \frac{P}{3f(2f+1)^{\frac{5}{2}}} = K_0[1 + \frac{3}{2}(K_0' - 4)f]$$

Equation 5

$$f = \frac{\left(\frac{V}{V_0}\right)^{-\frac{2}{3}} - 1}{2}$$

Equation 6

Chapter 3 NaCl-type multicomponent compounds

3.1 Introduction

As a starting point in the synthesis of multicomponent ceramics, a simple NaCl-type multicomponent nitride is selected. Binary transitional metal nitrides are famous for their high hardness and ultrahigh bulk modulus (e.g., VN, NbN) [17,18], chemical inertness (e.g., CrN) [19], super- and semi- conductivity (e.g., MoN, Ta_3N_5) [20,21], or ferromagnetism (e.g., Fe_4N) [22]. Therefore, it is anticipated that by combining multiple components, nitrides could exhibit even enhanced material properties.

However, among multicomponent ceramics, multicomponent nitrides are less reported. The majority of them have been synthesized in thin film forms with a NaCl-type structure, such as (Ti,Hf,Zr,V,Nb)N [23], (Ti,V,Cr,Zr,Hf)N [24], and (Al,Cr,Mo,Ta,Ti,Zr)N [25]. The synthesis of bulk multicomponent nitrides remains largely unexplored [26]. This is primarily due to the fact that nitrides typically require extended synthesis duration at elevated temperature for nitrogen molecules to undergo decomposition and react with the metals. But such high-temperature conditions can lead to the decomposition of the resulting nitrides.

Recently, high-pressure synthesis technique has proven to be feasible for synthesizing novel transitional metal nitrides [27–30], providing a fast and safe route for nitride synthesis. Consequently, there is considerable interest in synthesizing novel bulk multicomponent nitrides. In the meanwhile, high-pressure experiment using NH_4Cl as a nitrogen source and solvent have reported successful synthesis of nanowire tantalum nitride

[31] and single crystal tungsten nitride [32].

For comparison and examination of multicomponent compounds, the well-known multicomponent NaCl-type oxide (MgCoNiCuZn)O (i.e. $(Mg_{0.2}Co_{0.2}Ni_{0.2}Cu_{0.2}Zn_{0.2})O$) [5] was firstly synthesized under ambient pressure to compare with the NaCl-type multicomponent nitride. Thermal expansion and compression behaviors are discussed. Subsequently, the synthesis of multicomponent NaCl-type nitride (V,Cr,Mo,Nb,Ta)N using high-pressure technique is re-examined with additional composition adjusted experiment and compression, as well as thermal expansion experiments, to investigate the multicomponent effects between different ceramic systems.

3.2 Multicomponent oxide

3.2.1 Synthesis of NaCl-type (MgCoNiCuZn)O

The synthesis of NaCl-type (MgCoNiCuZn)O was conducted by weighting and mixing the equimolar amounts of MgO, NiO, CuO, CoO, and ZnO powders. The mixed powders were then pressed into pellets and fired in the air using a muffle furnace. The firing process involved heating to 1000 °C, maintaining the temperature for 12-16 hours, and quenching by immediately depositing the pellet onto a copper plate. This firing-and-quenching process was repeated three times, with each repetition involving powdering the sample pellet, mixing it with ethanol, and recompressing it into a pellet for firing.

Figure 3-1 shows the synchrotron XRD pattern of the (MgCoNiCuZn)O. Previous reports on the lattice constant of the NaCl-type (MgCoNiCuZn)O have provided values of a = 4.1993 (5) Å [5], a = 4.2307 (2) Å [33], a = 4.235 Å [34], a = 4.241 Å [35]. The synthesized (MgCoNiCuZn)O can be well explained by a cubic rock-salt structure. The lattice constants and cell volume are a = 4.23689(3) Å and V = 76.057(2) Å^3, which are consistent with the previous research. The SEM image of the sample is presented in Figure 3-2, and EDS images in Figure 3-3 confirm uniform dispersion of Mg, Co, Ni, Co, and Zn. According to EDS point analysis, the composition is $(Mg_{0.18}Co_{0.19}Ni_{0.18}Cu_{0.22}Zn_{0.23})O$ and is nearly equimolar.

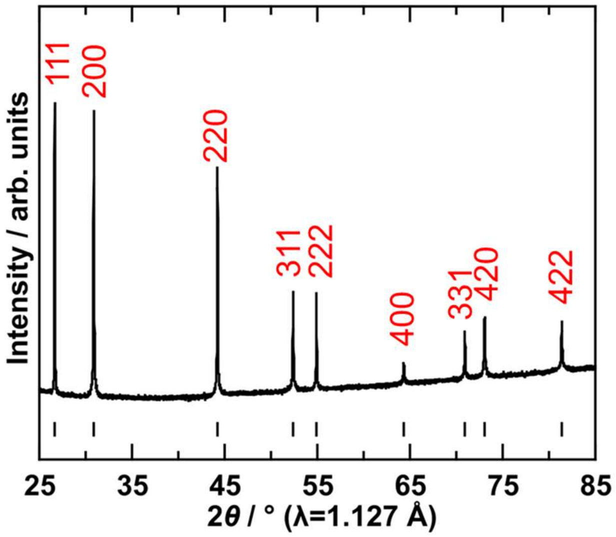

Figure 3-1 The synchrotron X-ray pattern of the (MgCoNiCuZn)O synthesized at 1273 K and ambient pressure. The marker corresponds to NaCl-type structure, and the peaks are indexed.

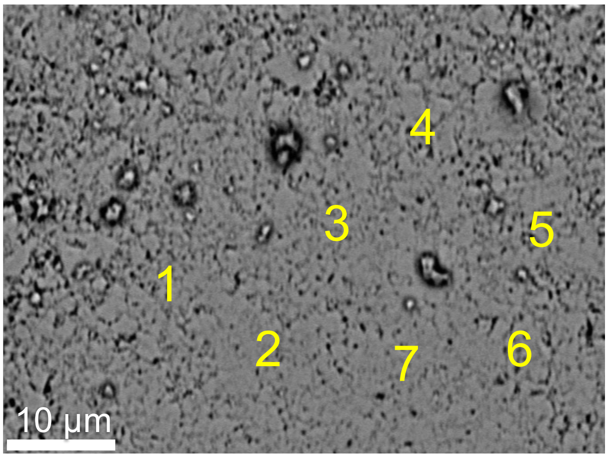

Figure 3-2 The scanning electron microscopy images of the (MgCoNiCuZn)O. The sample powders were pressed into pellet for SEM-EDS characterizations. The numbers represent EDS point mapping, and the data are shown in Table 3-1.

Table 3-1 The point analysis result of (MgCoNiCuZn)O correspond to Figure 3-2.

Point	Mg/at.%	Co/at.%	Ni/at.%	Cu/at.%	Zn/at.%
1	17.20	19.82	19.35	21.20	22.43
2	18.12	18.59	17.71	22.09	23.49
3	18.51	18.94	17.81	21.85	22.89
4	18.04	18.34	17.56	22.38	23.68
5	18.10	18.25	17.99	22.18	23.48
6	18.15	18.49	18.75	21.55	23.06
7	17.54	18.79	18.14	22.08	23.45
Avg.	17.95	18.75	18.19	21.90	23.21
Std. Dev.	0.40	0.49	0.59	0.38	0.41

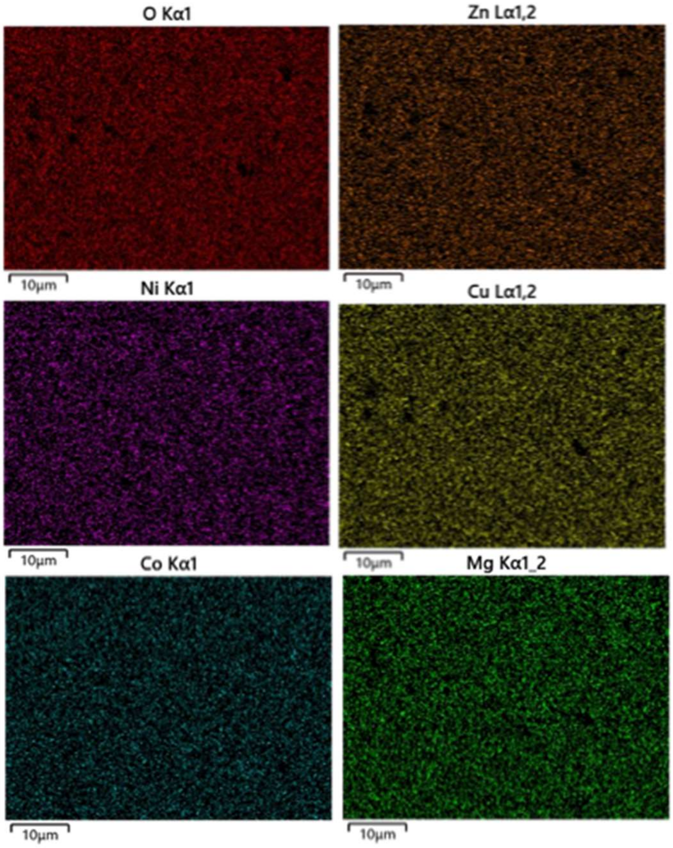

Figure 3-3 The Energy-dispersive X-ray spectroscopy images of the (MgCoNiCuZn)O. From the result of EDS mappings, it has homogeneous distribution of the elements.

The cell volume of the endmembers of (MgCoNiCuZn)O is also listed in Table 3-2. Since not all endmembers of (MgCoNiCuZn)O are NaCl-type structure, the multicomponent effect in (MgCoNiCuZn)O is compared among the volume of the endmembers. The cell volume of the (MgCoNiCuZn)O is almost the same as the weighted average calculated from the endmember oxides.

Table 3-2 The cell volume of the (MgCoNiCuZn)O and its endmember oxides.

		Volume / $Å^3$
MgO [36]		75.14
CoO [37]		77.31
NiO [38]		73.03
CuO [39]		80.37
ZnO [40]		95.62*
(MgCoNiCuZn)O	Exp. value	76.057(2)
	Weighted avg.	80.29

* The structure of ZnO is hexagonal with Z=2 and has a volume of 47.81 $Å^3$. For comparison with other oxider (Z=4) the volume of ZnO is doubled.

3.2.2 Thermal expansion and compression behavior

The low-temperature XRD patterns of (MgCoNiCuZn)O and the constituent oxides (MgO, CoO, NiO, CuO, ZnO) were taken and shown in Figure 3-4, and Figure 3-5. Throughout the experimental temperature range, (MgCoNiCuZn)O exhibited no additional peaks and remained stable down to 113 K. Notably, CoO underwent a temperature-induced phase transformation from a cubic structure to tetragonal/monoclinic symmetry just below room temperature (T ≈ 289K) [41,42]. The low-temperature peak fittings of CoO were done using the tetragonal phase, and data above 273K were excluded from the comparison. Figure 3-6a illustrates the temperature-dependent volume ratio changes for the constituent oxides and (MgCoNiCuZn)O. The volume of the (MgCoNiCuZn)O changed smoothly. No discontinuity in the volume-temperature curve was observed during cooling, indicating no phase transformation in this temperature range. Figure 3-6b displays the normalized change in axis ration with respect to temperature, with CoO exhibiting the largest change. Further details will be discussed later.

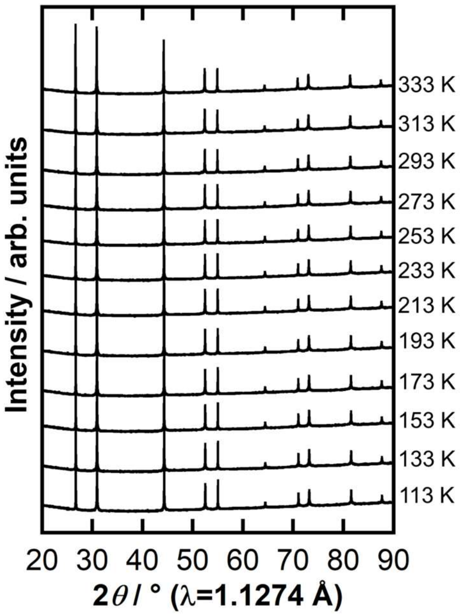

Figure 3-4 Temperature-dependent synchrotron XRD pattern of the (MgCoNiCuZn)O from low (113 K, bottom) to high temperature (333 K, top).

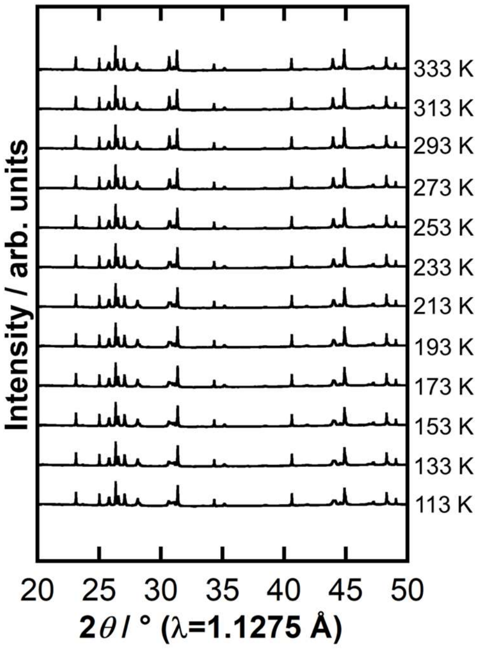

Figure 3-5 Low-temperature synchrotron XRD pattern taken on mixed constituent oxide powders from 113 K (bottom) to 333 K (top).

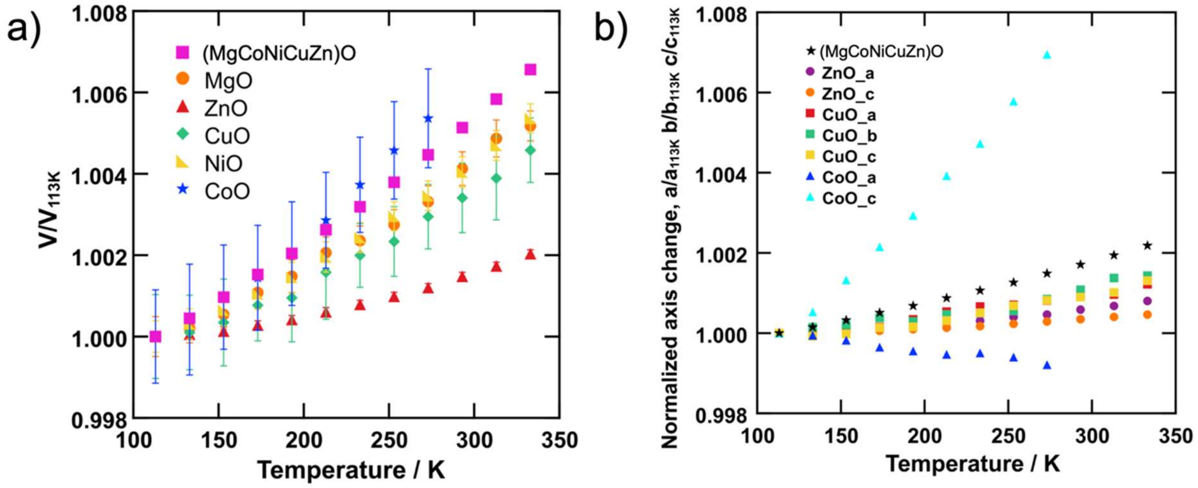

Figure 3-6 a) Normalized change of volume ratio of each oxide and the (MgCoNiCuZn)O with respect to the temperature. b) Normalized change of axis ratio with respect to the temperature.

From the low-temperature XRD pattern, the volume of (MgCoNiCuZn)O at each temperature can be derived. The coefficient of thermal expansion (CTE) was calculated from the volume-temperature data using the equations described in Chapter 2.3. The CTE has a linear relationship with temperature, which can be expressed by a general equation. The CTE at each temperature are summarized in Table 3-3 and plotted in Figure 3-7. The general equations are summarized in Table 3-4. Throughout the experimental temperature range, (MgCoNiCuZn)O exhibits higher CTE values than the average. Above 133 K, CoO has the highest CTE, which is related to the Jahn-Teller effect as mentioned below. However, below 133 K, it should be noted that the (MgCoNiCuZn)O has the highest CTE among all the constituent oxides. These results indicate that (MgCoNiCuZn)O has a smaller temperature dependency than all endmember binary oxides.

Table 3-3 The result of calculated thermal expansion at each experimental temperature.

Temperature (K)	CTE, α_V (K^{-1}) $\times 10^{-5}$					
	(MgCoNiCuZn)O	CoO	NiO	MgO	CuO	ZnO
113	2.28	1.95	1.52	1.55	1.14	0.34
133	2.40	2.31	1.69	1.71	1.32	0.45
153	2.52	2.67	1.85	1.87	1.49	0.55
173	2.65	3.04	2.02	2.03	1.67	0.66
193	2.77	3.40	2.18	2.19	1.85	0.77
213	2.89	3.76	2.35	2.35	2.03	0.88
233	3.01	4.12	2.51	2.51	2.21	0.99
253	3.14	4.48	2.68	2.67	2.39	1.10
273	3.26	4.84	2.84	2.83	2.56	1.20
293	3.38	-	3.01	2.99	2.74	1.31
313	3.50	-	3.17	3.14	2.92	1.42
333	3.62	-	3.33	3.30	3.10	1.53

Table 3-4 General volumetric CTE equation based on the experiment data.

(MgCoNiCuZn)O	$\alpha = 1.5901(11) \times 10^{-5} + 6.105(5) \times 10^{-8} \times T$
CoO	$\alpha = -8.7(3) \times 10^{-7} + 1.8043(15) \times 10^{-7} \times T$
NiO	$\alpha = 5.8990(14) \times 10^{-6} + 8.246(6) \times 10^{-8} \times T$
MgO	$\alpha = 6.555(13) \times 10^{-6} + 7.952(6) \times 10^{-8} \times T$
CuO	$\alpha = 1.321(13) \times 10^{-6} + 8.907(5) \times 10^{-8} \times T$
ZnO	$\alpha = -2.748(3) \times 10^{-6} + 5.4174(15) \times 10^{-8} \times T$

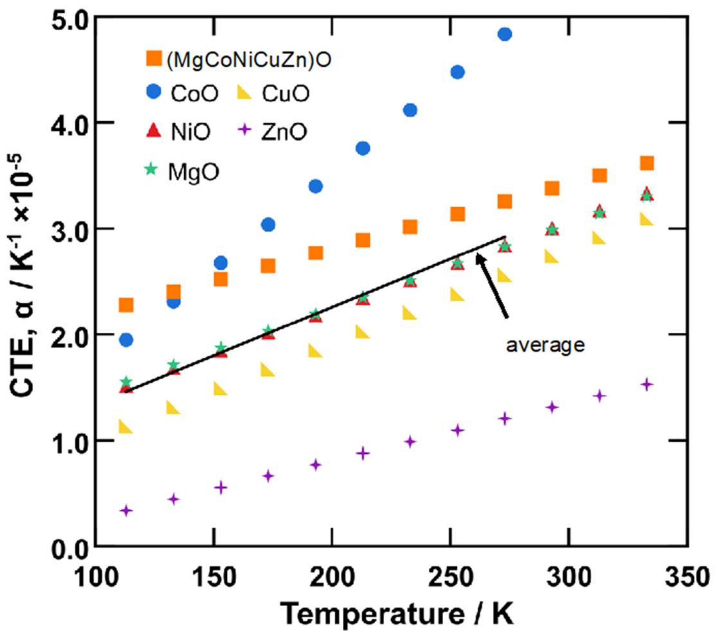

Figure 3-7 Temperature-dependent volumetric CTE change of the (MgCoNiCuZn)O and all constituent oxides. The line is the average volumetric CTE value calculated from the binary oxides.

The crystal structures of (MgCoNiCuZn)O, CoO, ZnO, and CuO are depicted in Figure 3-8 and the *β*-angle of CuO is summarized in Table 3-5. The axis ratios of the (MgCoNiCuZn)O, ZnO, CuO, and CoO with respect to the temperature are shown in Figure 3-6, enabling a comparison of the axis anisotropic relationship among these oxides. A small negative slope is observed for the *a*- axis of CoO, and the *c*- axis of CoO showed a significant change (large positive slope) even compared to other oxides. This substantial anisotropy arises from the fact that CoO_6 octahedra undergo Jahn-Teller distortions, as reported in papers [41–43]. Although it remains unclear how the Jahn-Teller effect in the CoO_6 octahedra can impact the structure of (MgCoNiCuZn)O at low temperatures, at higher temperatures (293-1273 K), it has been reported that CuO_6 octahedra can induce a local lattice distortion in (MgCoNiCuZn)O due to the Jahn-Teller effect [44,45]. Thus, it is plausible that the Jahn-Teller effect in the CoO_6 octahedra may also affect the structure of (MgCoNiCuZn)O at low temperatures.

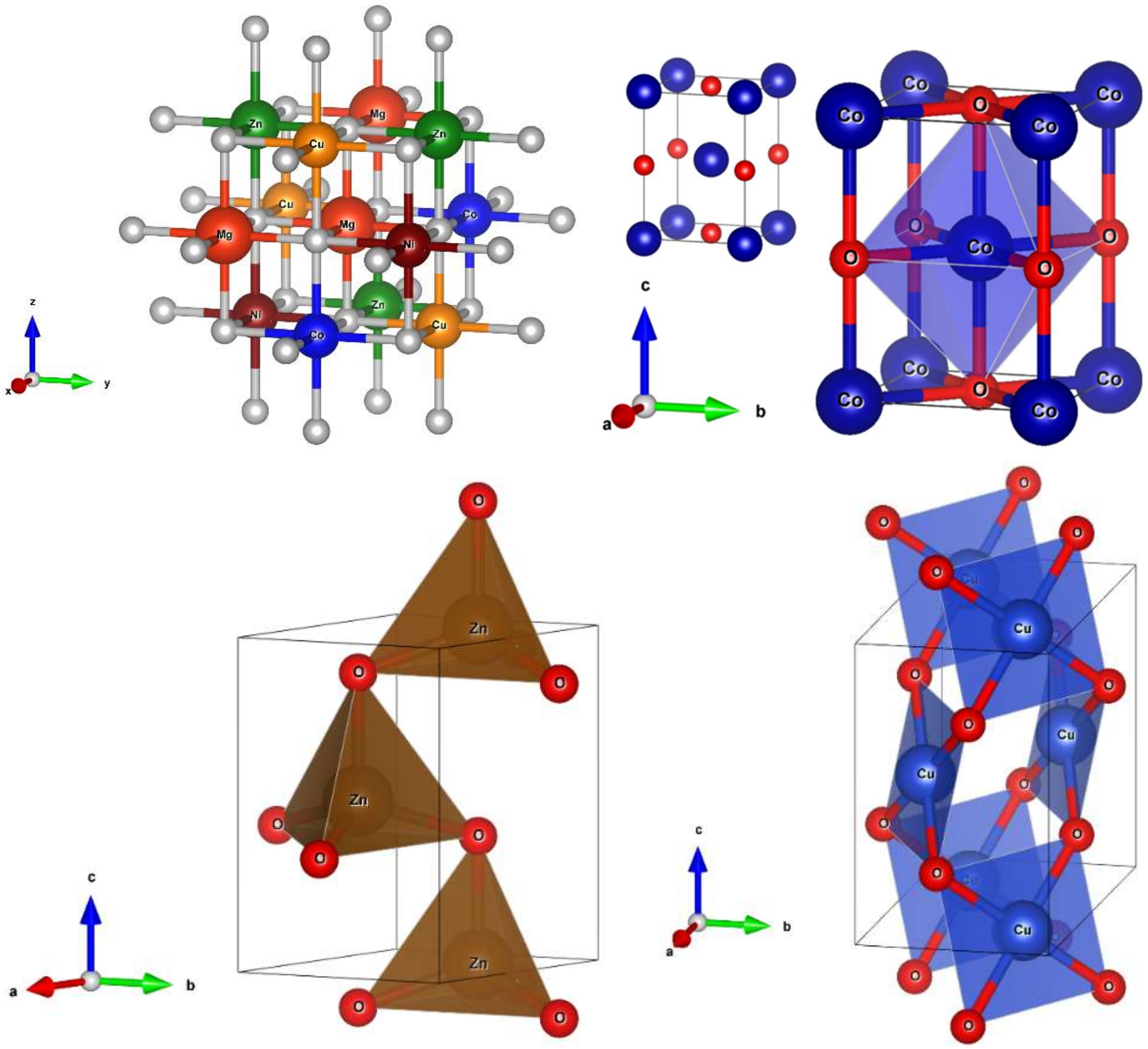

Figure 3-8 The crystal structures of (MgCoNiCuZn)O, CoO, ZnO, and CuO at 113 K. (MgCoNiCuZn)O is a NaCl-type structure, CoO is tetragonal, CuO is monoclinic, and ZnO is hexagonal. The Jahn-Teller elongation in the *c*- axis of CoO caused a phase transformation in CoO from cubic above room temperature to tetragonal below room temperature.

Table 3-5 The β-angle of CuO from 113 K to 333 K.

Temperature (K)	β (°)
113	99.640(7)
133	99.634(6)
153	99.605(8)
173	99.610(5)
193	99.596(8)
213	99.560(10)
233	99.536(3)
253	99.521(5)
273	99.496(3)
293	99.480(5)
313	99.466(8)
333	99.436(3)

A compression experiment was also conducted, and the bulk modulus of synthesized (MgCoNiCuZn)O was derived. The normalized volume with respect to pressure data is plotted in Figure 3-9, with the inset showing the normalized pressure F vs. Eulerian strain f plot. The bulk modulus obtained from the fitting using the Birch-Murnaghan EOS result in a value (142(7) GPa) lower than the one obtained from the F-f plot (174(18) GPa). While there are points that deviate largely from the fitting equation, the high-f region in the F-f plot is constant. Thus, the value of 174(18) GPa (with K_0'= 4.0 fixed) obtained from the F-f plot, is used for comparison. This value is also close to the value reported in previous study of 176 GPa [33]. The bulk modulus of endmember oxides is summarized in Table 3-6. (MgCoNiCuZn)O has almost the same value of bulk modulus as the weighted average of its endmembers.

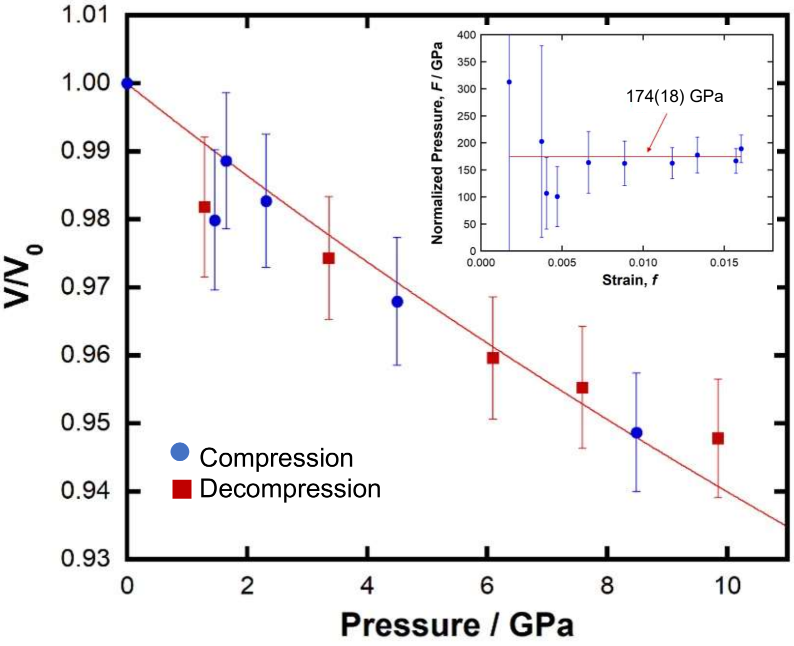

Figure 3-9 The compression behavior of (MgCoNiCuZn)O from pressures of 0 to 10 GPa. It should be noted that the compression behavior was taken using a laboratory Mo radiation X-ray, and the cell volume was calculated by fitting 3 peaks in the X-ray pattern. The bulk modulus of the (MgCoNiCuZn)O determined by fitting the second-order Birch-Murnaghan equation of state result in a zero-pressure bulk modulus of K_0= 142(7) GPa (K_0'= 4.0 fixed, red-line). The red-square markers represent compression data, and the blue-circle markers represent decompression data. The inset is the plot of the relation between normalized pressure F vs. Eulerian strain f. The fitting with K_0'= 4.0 fixed is shown in red line. The high-f region is constant, and the result gives a value of 174(18) GPa.

Table 3-6 The bulk modulus of the (MgCoNiCuZn)O and its endmember oxides.

Oxides		Bulk modulus / GPa
MgO [46]		179.0
CoO [47]		270
NiO[48]		187
ZnO [49]		183(7)
CuO [46]		81.0
$(Mg_{0.18}Co_{0.19}Ni_{0.18}Cu_{0.22}Zn_{0.23})O$	Exp. value	174(18)
	ref. [33]	176
	Weighted avg.	177

3.3 Multicomponent nitride

3.3.1 High-pressure synthesis of multicomponent (VCrMoNbTa)N

A multicomponent nitride was synthesized using a high-pressure technique combined with the use of NH_4Cl as the nitrogen source. The alloy starting material of multicomponent nitride was prepared by mixing equimolar amount of bulk V, Cr, Mo, Nb, and Ta using an arc-melting process. The SEM-EDS characterization of the alloy is shown in Figure 3-10.The elements are uniformly distributed, with an XRD pattern showing a single BCC phase (Figure 3-11). The alloy was then powdered and mixed with NH_4Cl inside a glove box for 1 hour at a ratio of alloy to NH_4Cl =1: 2. The final product was synthesized using a large volume press mentioned in Chapter 2.1.

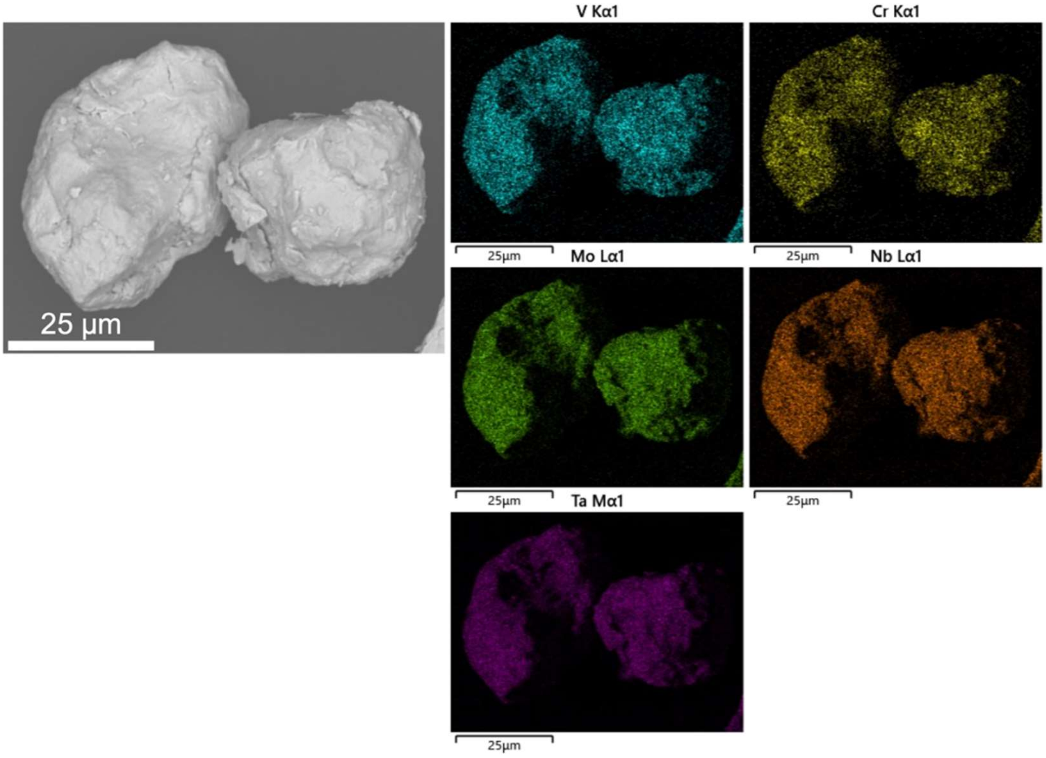

Figure 3-10 The SEM and EDS mapping of VCrMoNbTa alloy. The constituents have an average of V = 24.14 at.%, Cr = 15.29 at.%, Mo = 21.13 at/%, Nb = 21.00 at.% and Ta = 18.44 at.%.

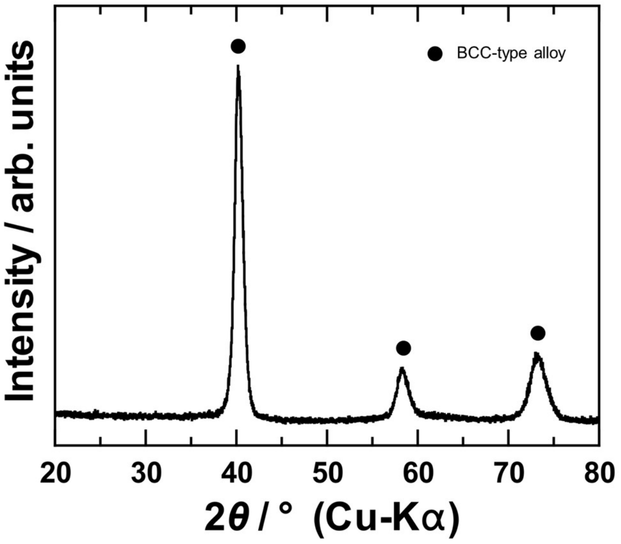

Figure 3-11 Powder XRD pattern of V-Cr-Mo-Nb-Ta alloy. The pattern shows single phase BBC-type alloy.

The high-pressure synthesized sample under the conditions of $P = 6$ GPa, $T = 1200$ °C, and $t = 1$ hour is presented in Figure 3-12. The main phase is a NaCl-type nitride with a minor phase of WC -type nitride and an impurity of Ta_2O_5. The presence of the Ta oxide impurity may result from a reaction with moisture (H_2O) in NH_4Cl. Despite the careful preparation of the sample inside a glovebox, small amounts of oxide impurity were formed. The lattice parameter and cell volume of NaCl-type nitride have been determined to be $a = 4.3087(2)$ Å and $V = 80.06(2)$ Å^3.

SEM characterization results are shown in Figure 3-13, revealing many micrometer-sized crystals. The cubic morphology of the crystals aligns with the NaCl-type structure observed in the XRD pattern (Figure 3-12). The EDS point analysis result of the sample is shown in Figure 3-14 and Table 3-7. It should be noted that V and Cr are less included in the structure, and the calculated constituent are $(V_{0.087}Cr_{0.005}Nb_{0.321}Mo_{0.344}Ta_{0.243})N$. These results indicate that NH_4Cl is quite useful for growing multicomponent metal nitride crystals under high pressure, similar to the reported binary ones such as W-N and Ta-N nitrides [31,32].

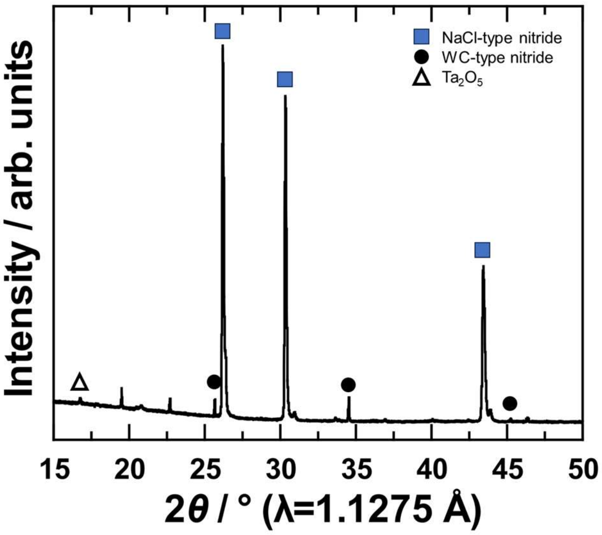

Figure 3-12 Synchrotron X-ray diffraction (XRD) pattern of the product synthesized at high pressure.

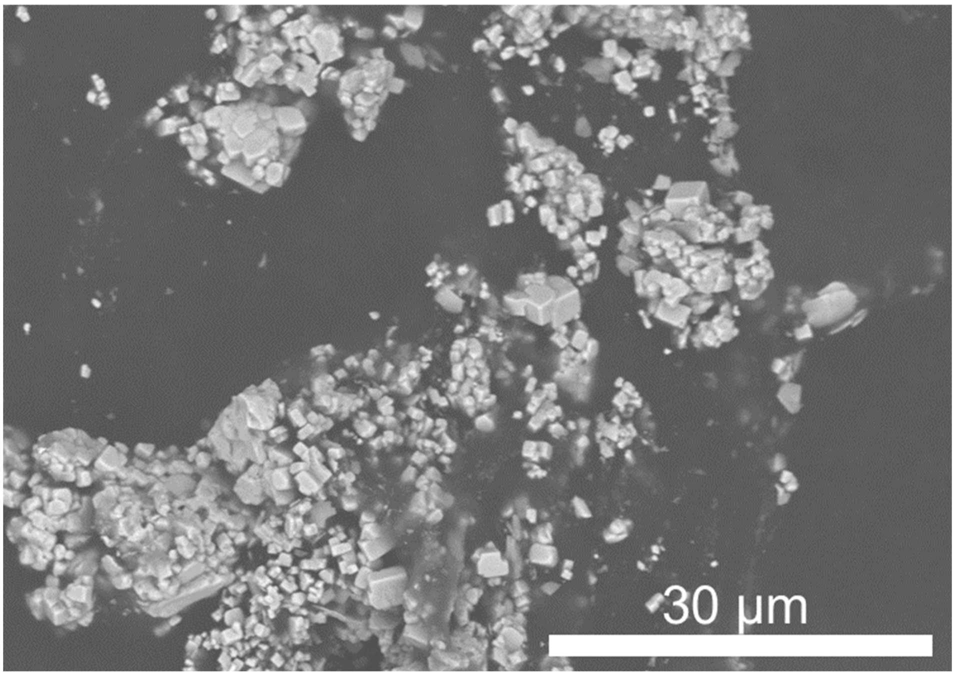

Figure 3-13 The SEM images of the synthesized nitride reveal a cubic crystal habitus. The constituent of the cubic crystal were calculated to be $(V_{0.087}Cr_{0.005}Nb_{0.321}Mo_{0.344}Ta_{0.243})N$ from EDS characterization.

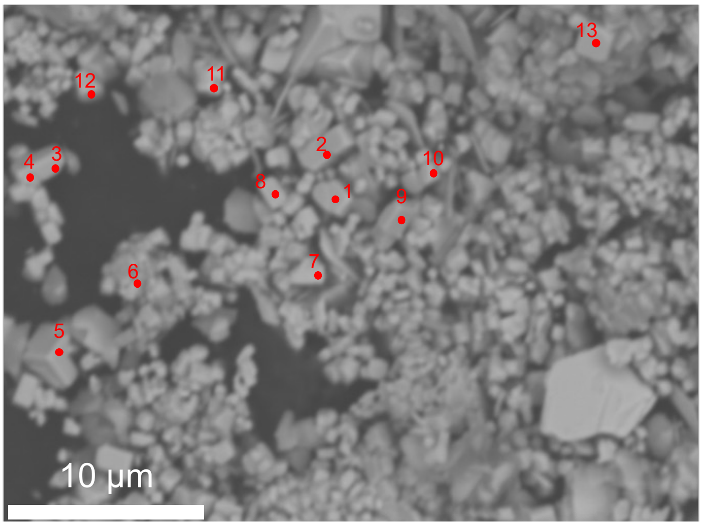

Figure 3-14 The SEM image with the EDS analysis point marked red in the figure. The point analysis results are show in Table 3-7.

Table 3-7 The EDS point analysis result correspond to Figure 3-14.

Point	V/at.%	Cr/at.%	Nb/at.%	Mo/at.%	Ta/at.%
1	9.48	0.49	35.59	28.68	25.76
2	8.33	0.39	34.23	32.29	24.75
3	9.86	0.51	31.29	34.58	23.75
4	9.32	0.46	34.11	31.77	24.34
5	11.35	0.23	33.51	27.72	27.18
6	6.76	1.42	31.46	37.69	22.67
7	8.79	0.55	29.37	35.81	25.48
8	9.30	0.48	29.58	37.36	23.28
9	7.72	0.45	30.86	37.44	23.52
10	6.57	0.45	29.26	42.68	21.05
11	6.88	0.17	31.47	37.39	24.10
12	10.16	0.03	33.50	30.57	25.75
13	8.64	0.43	33.06	33.72	24.15
Avg.	8.70	0.47	32.10	34.44	24.29
Std. Dev.	1.65	2.12	1.55	1.14	0.83

Assuming the cubic crystals are a NaCl-type nitride, the individual binary nitride endmembers reported with NaCl -type structure are summarized in Table 3-8. Using the weighted average method, the calculated value *a* = 4.30 Å is consistent with the experimental XRD result of *a* = 4.3087(2) Å for the synthesized multicomponent NaCl -type nitride.

Table 3-8 The lattice parameters of V, Cr, Nb, Mo, Ta binary nitrides.

NaCl -type nitrides	Lattice parameter / Å	*ref.*
VN	4.28	[50]
CrN	4.1499(7)	[51]
NbN	4.3934	[52]
MoN	4.212	[53]
TaN	4.32	[54]
(V,Cr,Nb,Mo,Ta)N	4.3087(2)	Exp. value
	4.30	Weighted avg.

The relatively lower content of V and Cr in the crystals may be attributed to the formation of chlorides during the high-pressure and high-temperature reaction with NH_4Cl. Figure 3-15 shows the SEM and the EDS mapping of the synthesized product before washing with distilled water. Three separate areas can be observed: the area that is rich in Nb, Mo, and Ta; the area enriched in V, Cr, and Cl; and the area with Cl along. The area enriched in Nb, Mo, and Ta is expected to be the nitride phase, and the Cl-enriched area is the NH_4Cl residuals. The area of V, Cr, and Cl has barely any inclusion of Nb, Mo, and Ta, suggesting that this area is the phase of V- and Cr-chlorides. Since transitional metal chlorides can be readily removed by distilled water, the V- and Cr-chlorides were washed away during the process. This led to fewer V and Cr inclusions in the SEM-EDS results presented earlier (Figure 3-13).

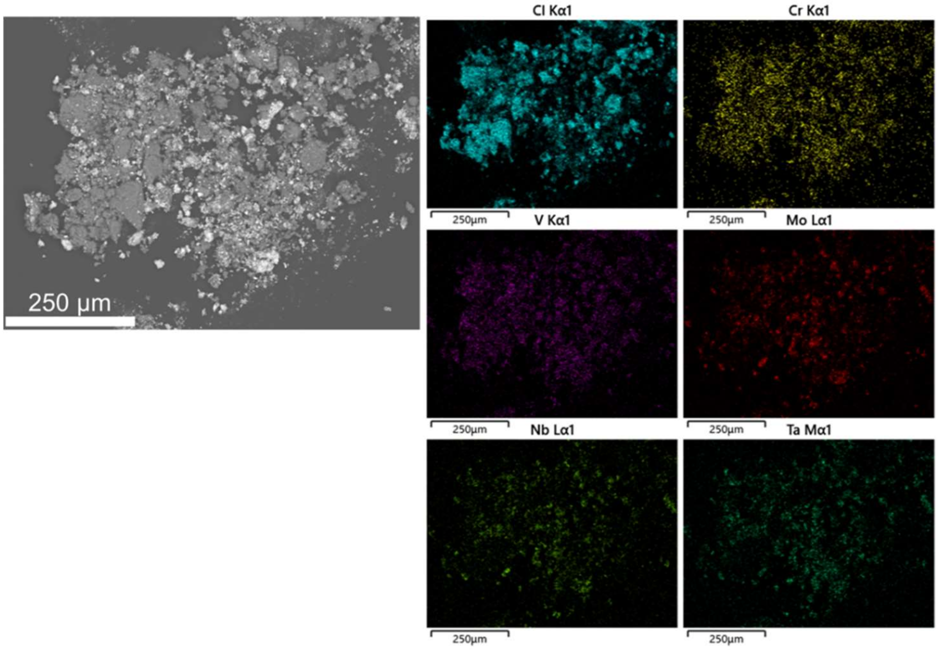

Figure 3-15 The SEM and EDS mapping of synthesized product prior to being washed with distilled water.

From the results mentioned above, it indicates that the addition of an excess amount of V and Cr may be required to achieve equimolar multicomponent product. Hence, another experiment was done to confirm this idea. The transition metal ratio of V: Cr: Mo: Nb: Ta = 3: 3: 1: 1: 1 was made into alloy. The polished fracture surface of the alloy was examined by SEM-EDS and shown in Figure 3-16. In the examined sample part, V and Cr is in excess. The alloy was then mixed with NH_4Cl at a ratio of alloy to NH_4Cl = 1:2. The synthesis was done under the same conditions described previously.

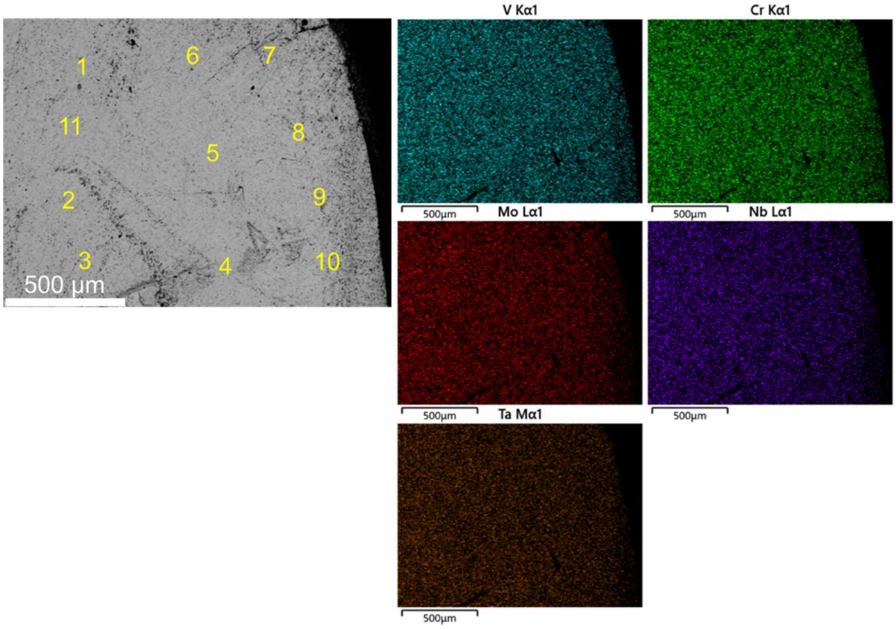

Figure 3-16 The SEM and EDS mapping of the V- and Cr-rich VCrMoNbTa alloy. The characterization was taken on a polished fracture surface of the alloy ball.

Table 3-9 The EDS point analysis result that corresponds to the points shown in Figure 3-16.

Point	V/at.%	Cr/at.%	Mo/at.%	Nb/at.%	Ta/at.%
1	43.02	37.38	7.89	5.04	6.67
2	37.81	41.04	4.87	8.34	7.93
3	39.01	38.83	6.25	8.06	7.86
4	40.8	33.72	10.29	6.63	8.56
5	39.65	35.22	8.49	7.82	8.82
6	38.51	37.85	6.95	8.1	8.6
7	41.11	34.07	9.57	6.33	8.92
8	40.86	37.8	7.61	6.39	7.34
9	38.08	39.37	5.41	8.48	8.66
10	39.02	36.41	7.58	7.33	9.65
11	37.2	37.39	7.03	9.11	9.27
Avg.	39.55	37.19	7.45	7.42	8.39
Std. Dev.	1.65	2.12	1.55	1.14	0.83

Figure 3-17 and Figure 3-18 present the XRD results of the synthesized product before and after being washed with distilled water. Peaks around 32 and 40° that greatly decrease in intensity after washing may be the chlorides. The SEM-EDS characterizations before and after washing are shown in Figure 3-19 and Figure 3-20, respectively. The corresponding EDS point analysis results are presented in Table 3-10 and Table 3-11. From Figure 3-18, the product can be described as a NaCl-type nitride with a lattice parameter of a = 4.226(6) Å close to the result discussed in Figure 3-12 (a= 4.3087(2) Å). However, from the SEM-EDS characterization shown in Figure 3-20, no cubic crystal habitus was observed. The EDS mapping before washing (Figure 3-19) shows that the sampling area is rich in Cl, V, and Cr. After washing (Figure 3-20) some Cl rich areas remained (point 5 and 6), and these areas are also rich in V and Cr. The rest (point 1, 2, 3, and 4) are rich in Mo, Nb, and Ta. After washing, most V and Cr disappear, meaning that even with the excess amount of V and Cr inclusions, most V and Cr had formed chlorides and washed away.

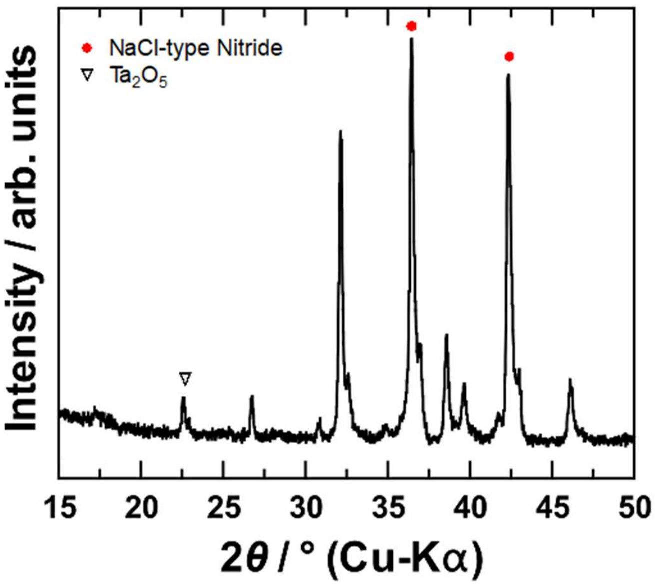

Figure 3-17 The XRD pattern of the V- and Cr-rich multicomponent nitride product, the pattern was taken before washed with distilled water.

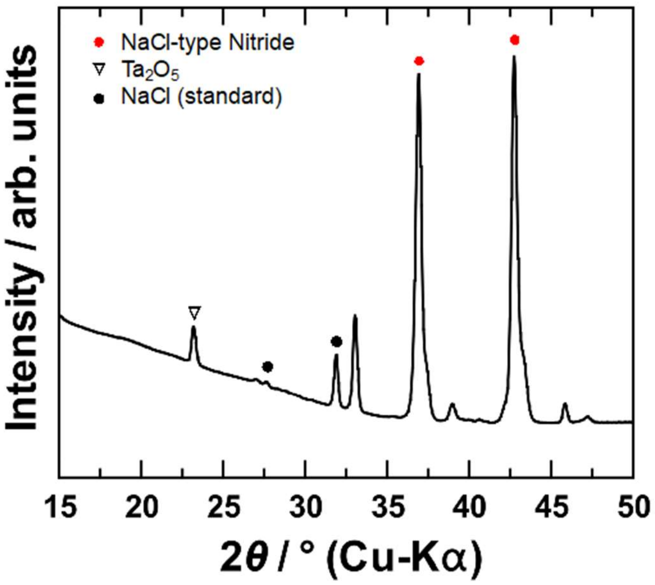

Figure 3-18 The XRD pattern of the V- and Cr -rich multicomponent nitride, the pattern was taken after washed with distilled water.

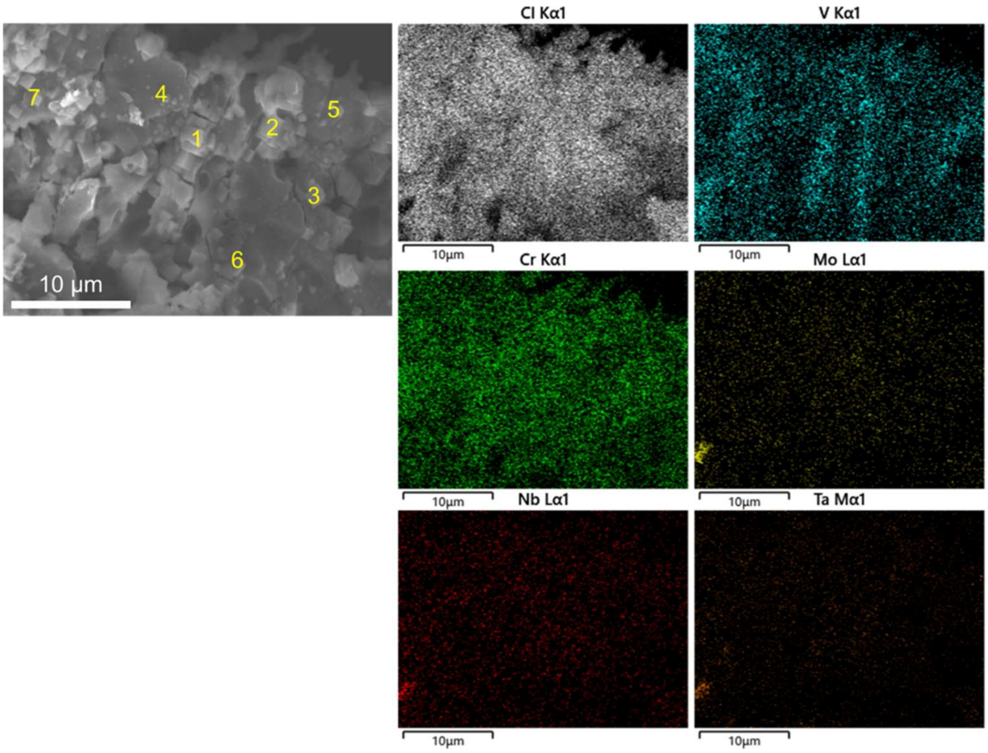

Figure 3-19 SEM and EDS mapping of the V- and Cr-rich multicomponent nitride before washed with distilled water.

Table 3-10 The EDS point analysis result. The points correspond to Figure 3-19.

Point	V/at.%	Cr/at.%	Mo/at.%	Nb/at.%	Ta/at.%	Cl/at.%
1	8.31	22.05	0.10	0.02	0.36	69.16
2	6.39	23.30	0.03	0.04	0.10	70.14
3	9.69	23.86	0.08	0.14	0.07	66.16
4	5.69	18.22	0.16	0.09	0.14	75.69
5	7.33	20.72	0.08	0	0.11	71.76
6	6.62	22.12	0.04	0	0.10	71.12
7	9.81	26.19	0.08	0.20	0.87	62.86

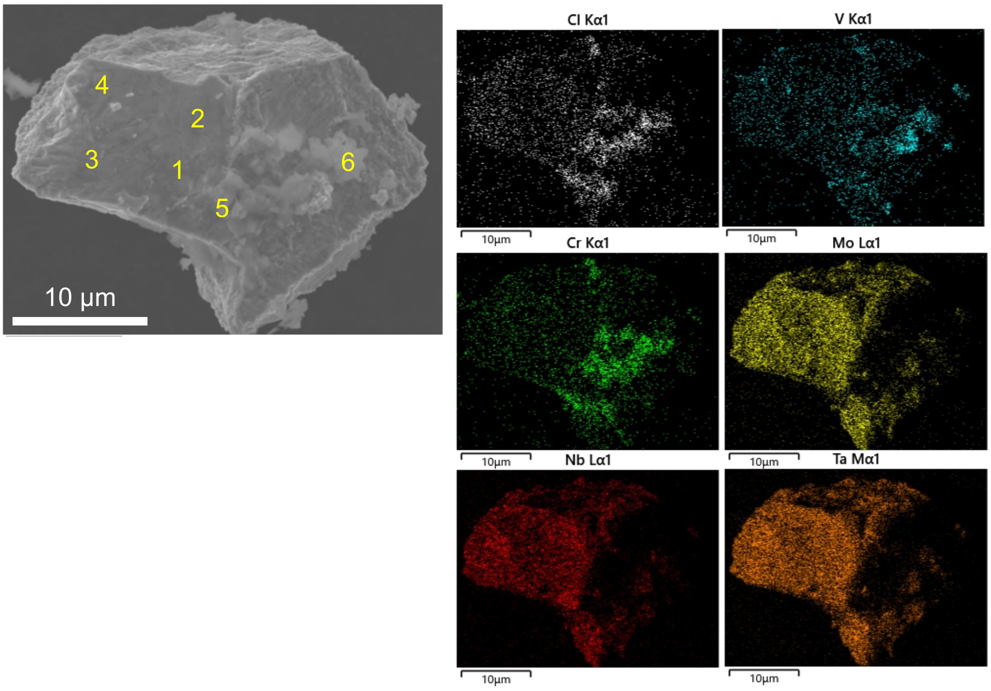

Figure 3-20 SEM and EDS mapping of the V- and Cr-rich multicomponent nitride after washed with distilled water.

Table 3-11 The EDS point analysis result. The points correspond to Figure 3-20.

Point	V/at.%	Cr/at.%	Mo/at.%	Nb/at.%	Ta/at.%	Cl/at.%
1	0.30	0.41	35.11	30.68	33.41	0.09
2	0.27	0.96	34.99	28.00	35.70	0.08
3	0.00	0.21	32.36	30.95	35.98	0.50
4	0.45	0.90	38.56	22.05	37.64	0.40
5	21.00	27.26	12.07	10.84	15.27	13.56
6	19.92	52.16	6.02	5.93	7.17	8.80

The inclusion of an excess amount of V and Cr did not solve the problem of V and Cr depletion in the final product. The formation of stable chlorides over nitride affects the final constituent in the multicomponent nitride. This suggests that for the synthesis of an equimolar five-element multicomponent nitride, whether the nitrogen source of NH_4Cl, i.e., chloride, should be replaced or the high potential chloride formation elements (such as V and Cr) should not be used. Nevertheless, the multicomponent nitride synthesized using an equimolar amount of each metal had a well-crystalline structure, and the following examinations in the next chapters are discussed using the $(V_{0.087}Cr_{0.005}Nb_{0.321}Mo_{0.344}Ta_{0.243})N$ described in Figure 3-12.

3.3.2 Thermal expansion and compression behaviors

3.3.2.1 Low temperature stability and thermal expansion behavior

The temperature dependent stability and expansion behavior of the multicomponent nitride have been examined. The low temperature XRD patterns are shown in Figure 3-21. No additional peak was detected, and $(V_{0.087}Cr_{0.005}Nb_{0.321}Mo_{0.344}Ta_{0.243})N$ did not undergo a phase transformation at low temperatures, indicating the stability of this nitride under such conditions.

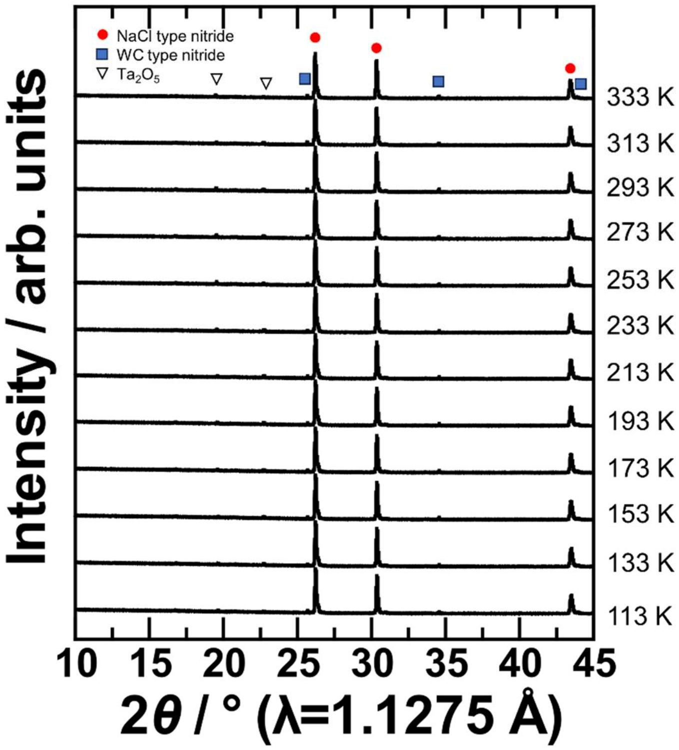

Figure 3-21 The low temperature XRD pattern of the synthesized multicomponent nitride from 333 K to 113 K. No extra peak is observed to low temperature.

The calculated CTE are shown in Table 3-12, and the general equations are present in Table 3-13. Figure 3-22 displays the plotted CTE figure for the NaCl-type multicomponent nitride $(V_{0.087}Cr_{0.005}Nb_{0.321}Mo_{0.344}Ta_{0.243})N$, and NaCl-type binary nitride NbN. The volumetric CTE at 293 K for $(V_{0.087}Cr_{0.005}Nb_{0.321}Mo_{0.344}Ta_{0.243})N$ is $\alpha_v = 1.70 \text{ x}10^{-5} \text{ K}^{-1}$. In comparison to the CTE of NbN ($\alpha_v = 1.85 \text{ x}10^{-5} \text{ K}^{-1}$ at 293 K), $(V_{0.087}Cr_{0.005}Nb_{0.321}Mo_{0.344}Ta_{0.243})N$ has smaller CTE value. However, due to the lack of data in the binary nitride, especially that MoN and TaN do not crystalized into NaCl-type structure at ambient pressure, it was unclear whether a multicomponent effect takes place in the $(V_{0.087}Cr_{0.005}Nb_{0.321}Mo_{0.344}Ta_{0.243})N$ and lowers the CTE.

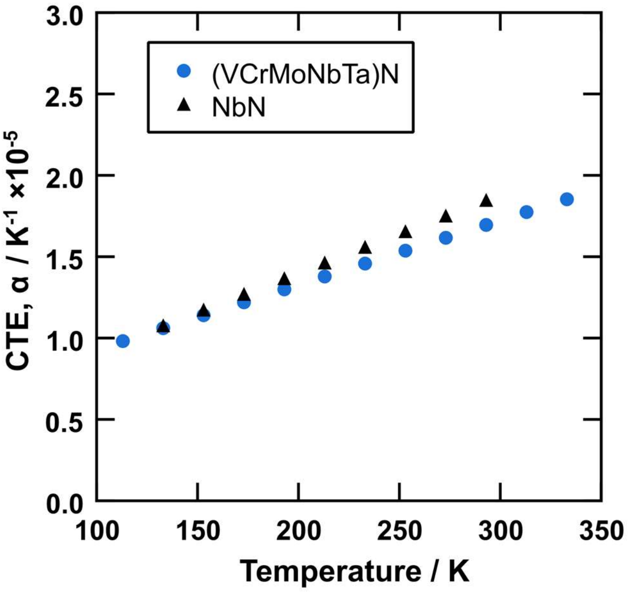

Figure 3-22 Temperature dependent volumetric CTE change of the high pressure synthesized multicomponent nitride $(V_{0.087}Cr_{0.005}Nb_{0.321}Mo_{0.344}Ta_{0.243})N$ using equimolar metal element alloy starting material. The binary NaCl-type nitride NbN is also potted in the figure.

Table 3-12 The calculated CTE at each temperature point for the NaCl-type ($V_{0.087}Cr_{0.005}Nb_{0.321}Mo_{0.344}Ta_{0.243}$)N and NbN. The data of NbN was measured by Ikoma (master thesis, 2019).

Temperature / K	CTE, α_v x 10^{-5} K^{-1}	
	($V_{0.087}Cr_{0.005}Nb_{0.321}Mo_{0.344}Ta_{0.243}$)N	NbN
113	0.98	-
133	1.06	1.08
153	1.14	1.18
173	1.22	1.27
193	1.30	1.37
213	1.38	1.46
233	1.46	1.56
253	1.54	1.66
273	1.62	1.75
293	1.70	1.85
313	1.77	-
333	1.85	-

Table 3-13 The general CTE equation of ($V_{0.087}Cr_{0.005}Nb_{0.321}Mo_{0.344}Ta_{0.243}$)N and NbN.

($V_{0.087}Cr_{0.005}Nb_{0.321}Mo_{0.344}Ta_{0.243}$)N	$\alpha_V = 5.341(4) \times 10^{-6} + 3.962(2) \times 10^{-8} \times T$
NbN	$\alpha_V = 4.381(4) \times 10^{-6} + 4.816(2) \times 10^{-8} \times T$

3.3.2.2 Pressure stability and compression behavior

Typically, nitrides exhibit high stability under pressure. resulting in a high bulk modulus. The compressibility of $(V_{0.087}Cr_{0.005}Nb_{0.321}Mo_{0.344}Ta_{0.243})N$ has been studied. The *in-situ* high-pressure synchrotron XPD patterns of the multicomponent NaCl-type nitride are shown in Figure 3-23. No additional peaks are observed in the patterns. The compression behavior of $(V_{0.087}Cr_{0.005}Nb_{0.321}Mo_{0.344}Ta_{0.243})N$ is shown in Figure 3-24, the multicomponent nitride is stable to 10 GPa. The normalized pressures F as a function of Eulerian strain f were also calculated to evaluate the fitting parameters and the result is shown in the inset of Figure 3-24.

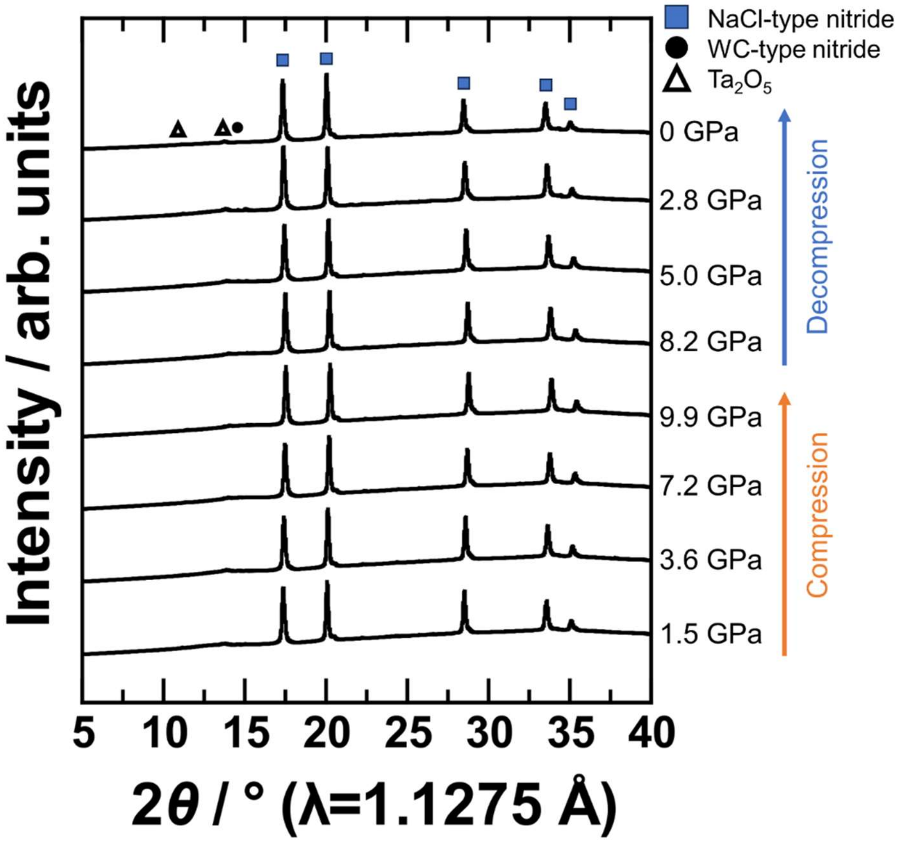

Figure 3-23 *In-situ* compression XRD pattern of $(V_{0.087}Cr_{0.005}Nb_{0.321}Mo_{0.344}Ta_{0.243})N$.

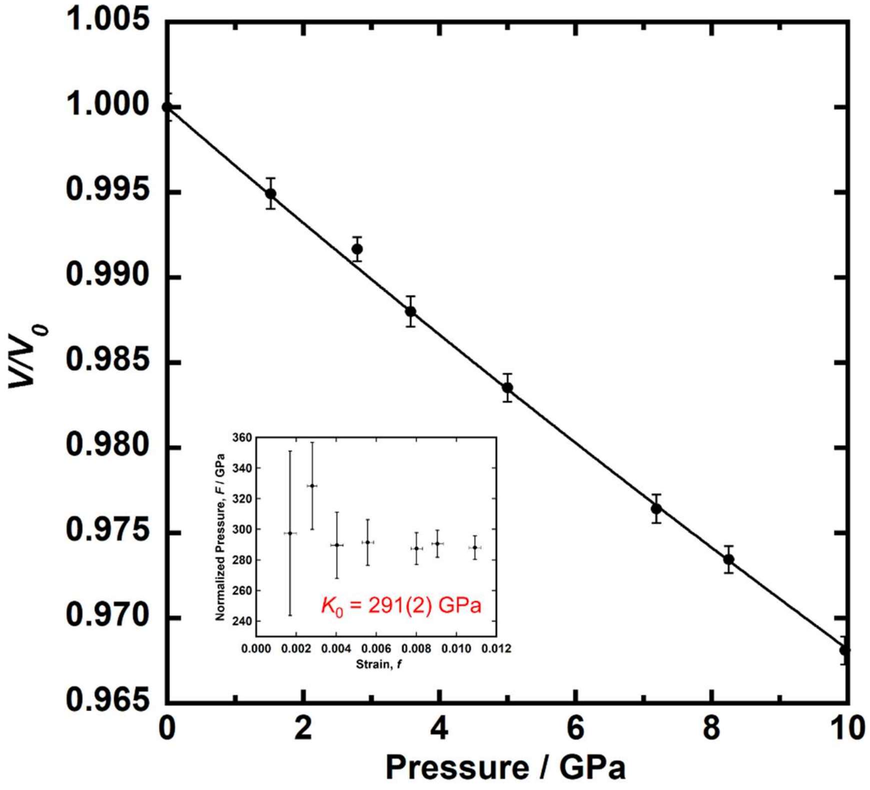

Figure 3-24 The volumetric compression result for the $(V_{0.087}Cr_{0.005}Nb_{0.321}Mo_{0.344}Ta_{0.243})N$ NaCl -type nitride. The inset is the plot of the relation between normalized pressure F vs. Eulerian strain f. The line is the fitting of the second-order Birch-Murnaghan equation of state (BM-EOS) with a result of K_0 = 290 (2) GPa (with K'_0 fixed to 4).

The bulk modulus of $(V_{0.087}Cr_{0.005}Nb_{0.321}Mo_{0.344}Ta_{0.243})N$ was calculated to be K_0 = 290(2) GPa. This is almost the same with the value calculated by the weighted average: 306 GPa using the reported bulk modulus for the according binary nitrides (Table 3-14).

Table 3-14 The bulk modulus of V, Cr, Nb, Mo, Ta binary nitrides.

NaCl -type nitrides	Bulk modulus / GPa	*Ref.*
VN	265(5)	[55]
CrN	257(5)	[56]
NbN	323(1)	[17]
MoN	307	[57]
TaN	295(1)	[54]
(V,Cr,Nb,Mo,Ta)N	290(2)	Exp. value
	306	Weighted avg.

3.4 Conclusion

In Chapter 3.2, the famous multicomponent oxide (MgCoNiCuZn)O was examined. The synthesis of (MgCoNiCuZn)O was carried out under ambient pressure, and the low-temperature thermal expansion and compression behaviors were discussed. The lattice parameter of (MgCoNiCuZn)O can be approximated by the weighted average of its endmembers. The results of coefficient of thermal expansion (CTE) revealed that the constituent oxide CoO has the highest CTE above 153K. However, it is found that (MgCoNiCuZn)O exhibits the highest CTE below 133K. Comparing the axis anisotropy behavior of the constituent oxides, CoO is observed to undergo a significant change due to a Jahn-Teller distortion. It is plausible that the CoO_6 octahedra may influence the local structure of (MgCoNiCuZn)O, similar to the reported Jahn-Teller distortion of the CuO_6 octahedra above room temperature. The bulk modulus of (MgCoNiCuZn)O is almost the same as the weighted average calculated from its endmember oxides.

Multicomponent nitrides were synthesized using a large volume press, and crystal growth with a cubic habitus was observed. The feasibility of high-pressure synthesis using NH_4Cl was demonstrated. However, only a small amount of V and Cr was found in the $(V_{0.087}Cr_{0.005}Nb_{0.321}Mo_{0.344}Ta_{0.243})N$ due to the formation of chlorides. Despite incorporating extra amount of V and Cr into the starting material in an attempt to create an equimolar multicomponent nitride, the product still exhibited depletion in V and Cr. Nevertheless, the thermal expansion and compression behaviors of $(V_{0.087}Cr_{0.005}Nb_{0.321}Mo_{0.344}Ta_{0.243})N$

were examined. The lattice parameter and bulk modulus of $(V_{0.087}Cr_{0.005}Nb_{0.321}Mo_{0.344}Ta_{0.243})N$ represent the average of its endmembers.

The multicomponent effect in oxide and nitride are summarized:

1) The (MgCoNiCuZn)O has almost the same value of bulk modulus as the weighted average of its endmembers. The lattice parameter of $(V_{0.087}Cr_{0.005}Nb_{0.321}Mo_{0.344}Ta_{0.243})N$ is also the same as the weighted average of its endmembers.
2) The thermal expansion behavior of (MgCoNiCuZn)O is above the average of its endmembers. The multicomponent effect in the thermal expansion behaviors of the $(V_{0.087}Cr_{0.005}Nb_{0.321}Mo_{0.344}Ta_{0.243})N$ need further information on its endmembers.
3) The bulk modulus of both the multicomponent oxide and nitride are the same as the weighted average of their endmembers.

Thus, the multicomponent oxide demonstrates a clear multicomponent effect in thermal expansion behavior, while the multicomponent nitride does not exhibit obvious multicomponent effects. The observed multicomponent effect in the thermal expansion behavior of the multicomponent oxide may originate from the Jahn-Teller effect in CoO, influencing the local Co octahedra in the structure of (MgCoNiCuZn)O during cooling.

Chapter 4 Multicomponent phosphides

4.1 Introduction

Transition metal phosphides constitute a class of inorganic compounds that has garnered substantial attention due to its distinctive physical and chemical properties, holding promise for various applications including catalysis, energy storage, and electronics [58–61]. These compounds exhibit a broad range of stoichiometry and structure, with reported composition varying from metal-rich [62] to phosphorus-rich [63]. Metal-rich phosphides, or those with phosphorus-poor compositions, have been extensively studied, revealing intriguing metallic electrical properties and magnetic phenomena. Examples include Fe_3P, Ni_2P, and Cr_3P [64–66]. Incorporating multiple metal species into these compounds has yield superior properties, such as superconductivity (e.g., MoRuP) [67,68], catalyst (e.g., CoMnP) [69], and supercapacitor [70] (e.g., ZnNiCoP). In contrast, phosphorus-rich compounds are less reported. They have shown potential for applications in thermoelectric material (NiP_2) [71], reversible lithium-ion battery (MnP_4, CoP_3) [72,73], and solar energy conversion material (FeP_4) [74]. Besides, combining both factors of phosphorus-rich and multiple-transition-metal-species within a single phosphide in addition to the phosphorus-rich factor represents a largely unexplored avenue.

Similar to the challenges encountered in the synthesis of multicomponent nitrides mentioned in Chapter 3.1, the synthesis of phosphides poses difficulties. For instance, phosphorus has high vapor pressure, while transition metals have high melting point. In order to overcome these problems, earlier studies used highly reactive starting materials like yellow phosphorus [75], though this substance ignites spontaneously in air, producing toxic and corrosive byproducts. Alternatively, some researchers have employed flux methods involving tin (Sn) and prolonged annealing periods of over a week for synthesis [76,77].

Taking advantage of high-pressure technique, previously shown to be feasible in synthesizing multicomponent nitride as discussed in the previous chapter, multicomponent phosphides are studied because they can crystalize in more complicated structures. The ability of high-pressure technique in the synthesis of multicomponent compounds with complicated anisotropic structure is of interest. Historically, CrP_4 was synthesized under high-pressure [78]. Starting with the base of the binary phosphide CrP_4, transition metal elements were added in to CrP_4. The elements that were considered were vanadium, manganese, and molybdenum surrounding chromium on the periodic table. Vanadium and manganese are 3d transitional metals that are the same as chromium, and they have similar atomic size. In contrast, molybdenum, a 4d transition metal, is larger in size. Also, VP_4, and MoP_4 were reported to crystalize into the same CrP_4-type structure while MnP_4 is described to be the stacking variant of CrP_4. Considering the synthesis challenges, the multicomponent phosphide experiments began with the synthesis of (V,Cr)-phosphide. Then expanding subsequently to (V,Cr,Mn)-phosphide and (V,Cr,Mo)-phosphide. The synthesis conditions and the multicomponent effect on lattice parameters, compression and thermal expansion behaviors are discussed.

4.2 High-pressure synthesis and homogeneity

4.2.1 (V,Cr)P_4

The initial sample was made by using transition metal powders. Each transition metal powder was directly mixed with red phosphorus inside glove box for 30 min. Then, the mixed powder sample underwent synthesis under conditions of $P = 5$ GPa, $T = 1100$ °C and a heating time of 1 hour. After heating, the sample was quenched by turning off the heater power and then recovered at ambient pressure. The XRD pattern of the final product is presented in Figure 4-1, with the enlargement of the 110 peak in the inset displaying asymmetrical peak shapes. This asymmetric peak shape suggests the possibility of individual reactions between each transition metal and phosphorus, resulting in an inhomogeneous multi-phase product.

The result of the mixed powder starting sample underscores the importance of mixing mixed at the atomic scale before high-pressure synthesis. Drawing from the nitride synthesis experience described in Chapter 3.3.1, the transition metals were alloyed before mixing with red phosphorus. Another starting sample was prepared using V-Cr alloy. The starting V-Cr alloy was prepared by liquid quenching bulk vanadium and chromium metals using a quartz tube. Then, the alloy was powdered and mixed with red phosphorus inside the glove box with a ratio of alloy to phosphorus= 1: 4 for 30 minutes. The high-pressure synthesis was carried out at conditions of $P = 5$ GPa, and heating at $T = 1100$ °C for 1 hour. The sample recovery followed the previously mentioned process.

The synthesized product was characterized by synchrotron X-rays diffraction measurements. Figure 4-2 displays the room temperature (293K) XRD pattern, indicating a predominantly single-phase product. The peak shapes are sharp and symmetrical compared to Figure 4-1, emphasizing the importance of utilizing and alloy as the starting material. The pattern corresponds to a CrP_4 -type structure. Applying Vegard's law in $(V_xCr_{1-x})P_4$ (Figure 4-3), the composition of the synthesized pseudo-binary phosphide is calculated to be $x = 0.51$ in $(V_xCr_{1-x})P_4$, i.e., almost equimolar, which is the average of the endmember binary phosphides. The composition was further examined using SEM-EDS and the results are shown in Figure 4-4 and Table 2-1. V and Cr are spread uniformly throughout the product with a point analysis result of metal to phosphorus ratio approximately 1:4, indicating the homogeneity of transition metals within the CrP_4-type structure.

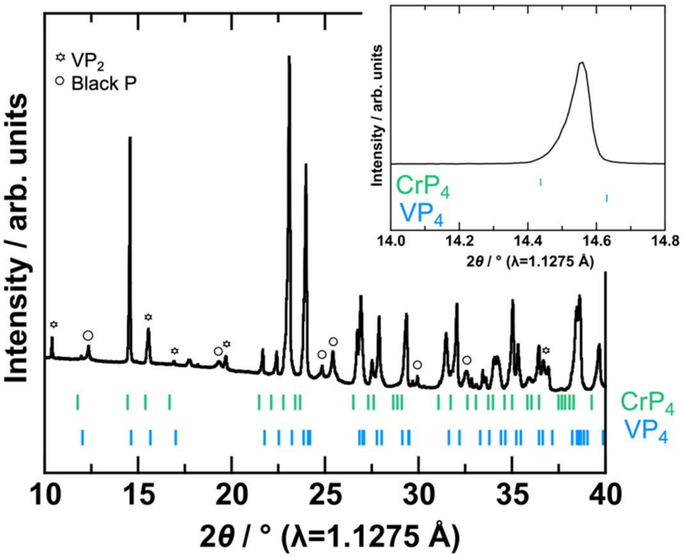

Figure 4-1 Synchrotron XRD of mixed powder V, Cr, P synthesized under high-pressure. The inset is the enlarged pattern showing the 110 peak. The markers show the peak positions for CrP_4 (green) and VP_4 (blue).

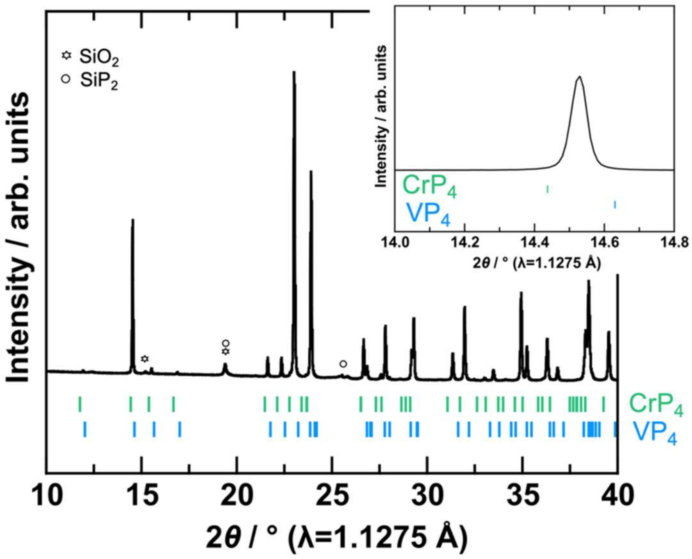

Figure 4-2 Synchrotron XRD of (V,Cr)-alloyed phosphide product synthesized under high-pressure. The inset is the enlarged pattern showing the 110 peak. The markers show the peak positions for CrP_4 (green) and VP_4 (blue).

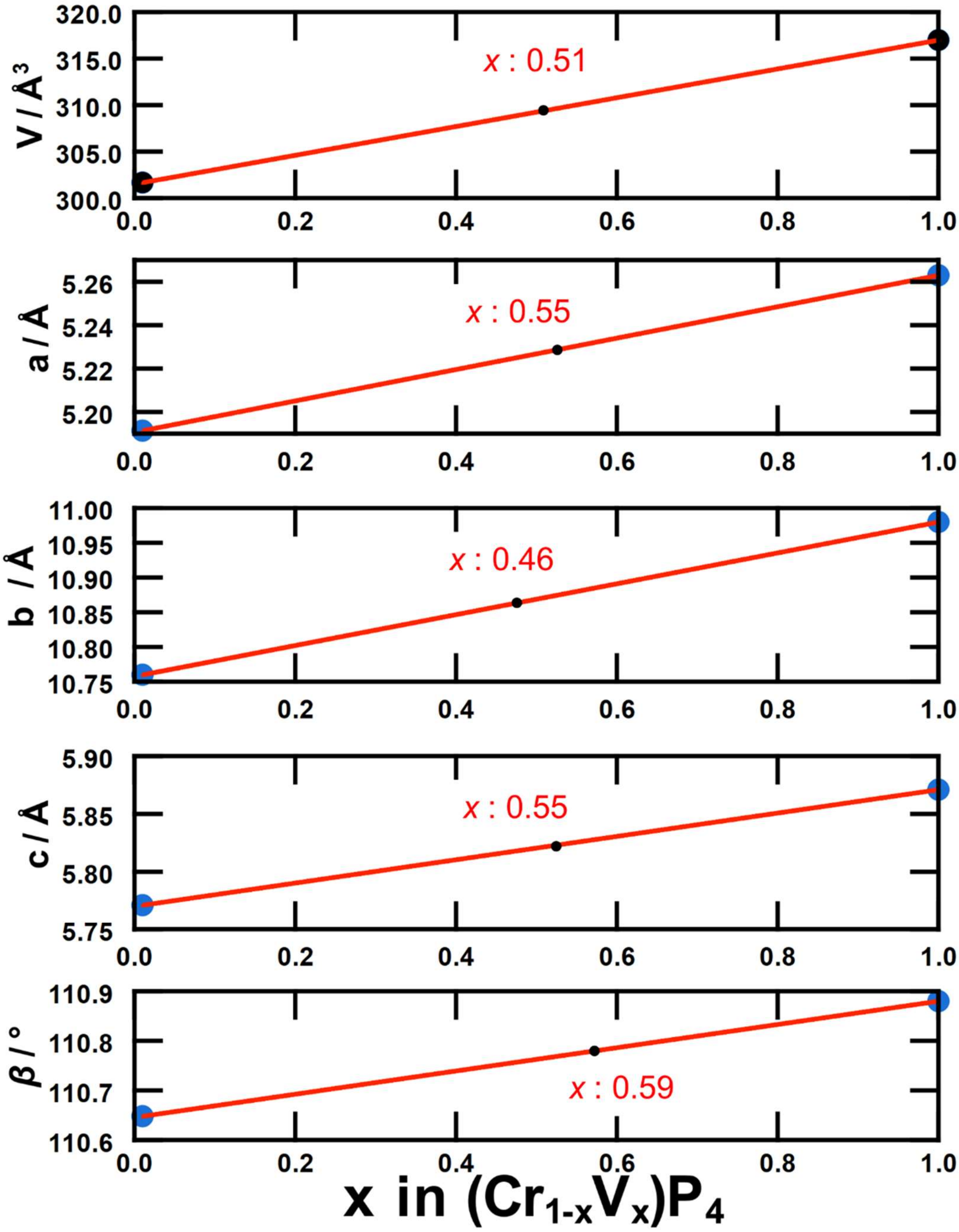

Figure 4-3 Plot of Vegard's law with the calculated values for lattice parameters *a, b, c*, *β* and cell volume of $(Cr_{1-x}V_x)P_4$ as a function of vanadium composition. The end members are CrP_4 and VP_4 with reported lattice parameters of *a* = 5.1914(5) Å, *b* = 10.7600(8) Å, *c* = 5.7712(6) Å, *β* = 110.648(6) °, *V* = 301.67 (6) Å^3 and *a* = 5.263 Å, *b* = 10.98 Å, *c* = 5.871 Å, *β* = 110.88 °, *V* = 316.99 Å^3, respectively.

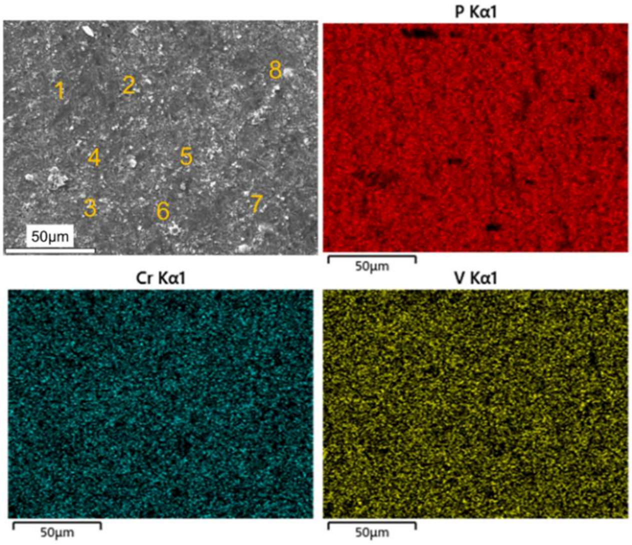

Figure 4-4 The SEM and EDS mappings of a piece of synthesized sample, the surface of the sample was polished. V and Cr are uniformly spread throughout the structure and the point analysis result is shown in Table 4-1.

Table 4-1 The EDS point analysis result correspond to Figure 4-4.

Point	V/at.%	Cr/at.%	P/at.%
1	10.56	11.78	77.66
2	9.71	10.28	80.01
3	9.99	9.49	80.51
4	10.25	10.62	79.13
5	9.35	10.48	80.17
6	9.92	11.49	78.60
7	10.97	11.24	77.79
8	8.94	10.29	80.77
Avg.	9.96	10.71	79.33
Std. Dev.	0.61	0.70	1.14

The XRD pattern was successfully refined using Rietveld methods, as presented in Figure 4-5. The calculated and observed diffraction profile exhibit reliability factors of R_{wp} = 3.012%, R_{p} = 2.712%, R_{B} = 1.427%, and R_{F} = 0.557% with goodness of fit (GOF) S = 5.3497. Less than 3% of impurity phases are presented in the product. The refinement details are shown in Table 4-2. The atomic coordinates, occupancies, and isotropic atomic displacement parameters are listed in Table 4-3. The Rietveld refinement results show low values of reliability factors, confirming that the synthesized sample is an equimolar CrP_4-type phosphide.

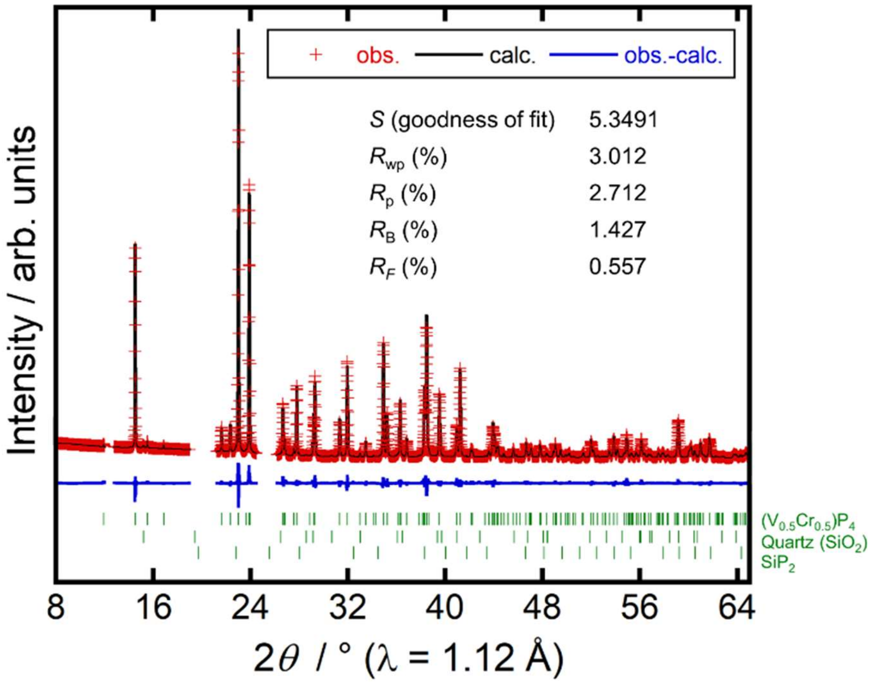

Figure 4-5 Rietveld refinement of the synchrotron XRD pattern at room temperature 293K. The 2*θ* region of 12.0-12.80, 19.0-21.20 and 24.50-26.15° corresponding to unassigned peaks were eliminated. The green markers from top to down represent $(V_{0.5}Cr_{0.5})P_4$, SiO_2, and SiP_2 respectively. Their mass fractions are $(V,Cr)P_4$, 96.9%; SiO_2, 2.6%; SiP_2, 0.5%. The Si contamination comes from quartz tube during liquid quenching process.

Table 4-2 Cell Parameters and Reliability Factors for the Rietveld-refined $(V_{0.5}Cr_{0.5})P_4$.

Compound	$(V_{0.5}Cr_{0.5})P_4$
Formula Weight (g*mol^{-1})	175.364
Space Group	*C2/c* (No.15)
a (Å)	5.23133 (5)
b (Å)	10.86133 (8)
c (Å)	5.82576 (6)
β (°)	110.7800 (6)
V (Å^3)	309.483 (5)
Z	4
D_{calc} (g*cm^{-3})	3.763684

Table 4-3 Atomic position, occupancies, and isotropic atomic displacement parameters for $(V_{0.5}Cr_{0.5})P_4$.

Atom	Site	Occ.^{a}	x	y	z	B (Å^2)
P1	8f	1	0.22577(13)	0.41053(6)	0.32353(13)	0.277(19)
P2	8f	1	0.27502(12)	0.22228(6)	0.18938(12)	0.078(19)
V/Cr	4e	0.5/0.5	0	0.06243(6)	1/4	0.084(16)

4.2.2 (V,Cr,Mn)P_4

The pseudo-binary (V,Cr)P_4 was successfully synthesized previously, prompting further exploration with the addition of Mn. Mn, being a 3d transition metal with close atomic size to V and Cr, was chosen. Experiments aimed at incorporating Mn into (V,Cr)P_4 were conducted, and a summary of various experimental conditions is presented in Table 4-4. In run21, (V,Cr,Mn)-phosphide was synthesized under conditions of P = 4 GPa, temperature, T = 1200 °C, and t = 1 hour. The synchrotron XRD pattern is shown in Figure 4-6, revealing a main phase corresponding to a monoclinic (C2/c) symmetry with a CrP_4-type structure. However, the XRD pattern displayed spottiness, resulting in unsharp peak shape as shown in the inset of Figure 4-6. The SEM-EDS characterization shown in Figure 4-7, reveals crystal-like habitus. These small crystals may be the cause of the observed peak shape irregularities in the XRD pattern. This factor makes it unable to be refined using the Rietveld method. Despite this, EDS mappings demonstrate uniform inclusion of V, Cr, and Mn in the crystals, with the surrounding composition being predominantly phosphorus (almost 100% in composition). The point analysis results for the crystals are detailed in Table 4-5, indicating nearly equimolar transition metal constituents with a metal to phosphorus ratio of approximately 1:4.

Table 4-4 List of different experiment conditions done for finding the best synthesis condition for (V,Cr,Mn)-phosphide.

run#	starting metal form	metal:phosphorus ratio	pressure / GPa	temperature / °C	time / hour
13	mixed powder	1:5	5	1000	1
14	mixed powder	1:5	5	1200	1
18	mixed powder	1:5	5	1200	3
21	alloy	1:6	5	1200	1
22	alloy	1:6	5	1200	2
23	alloy	1:6	5	1000	1
24	alloy	1:6	4	1000	1
29	alloy	1:6	4	1000	0.5
35	alloy	1:6	5	1200	0.5
36	alloy	1:6	4	1200	1

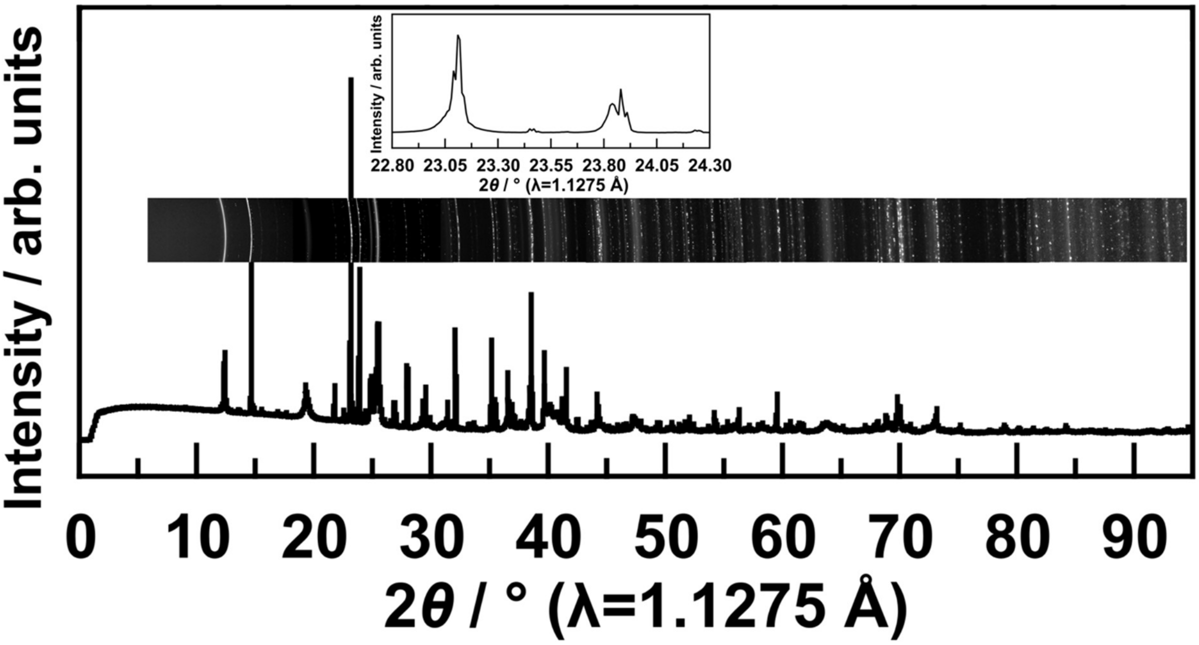

Figure 4-6 The synchrotron XRD pattern of (V,Cr,Mn)-phosphide product. The inset is the enlarged pattern on the two most intense peaks range from 22.8 to 24.3°.

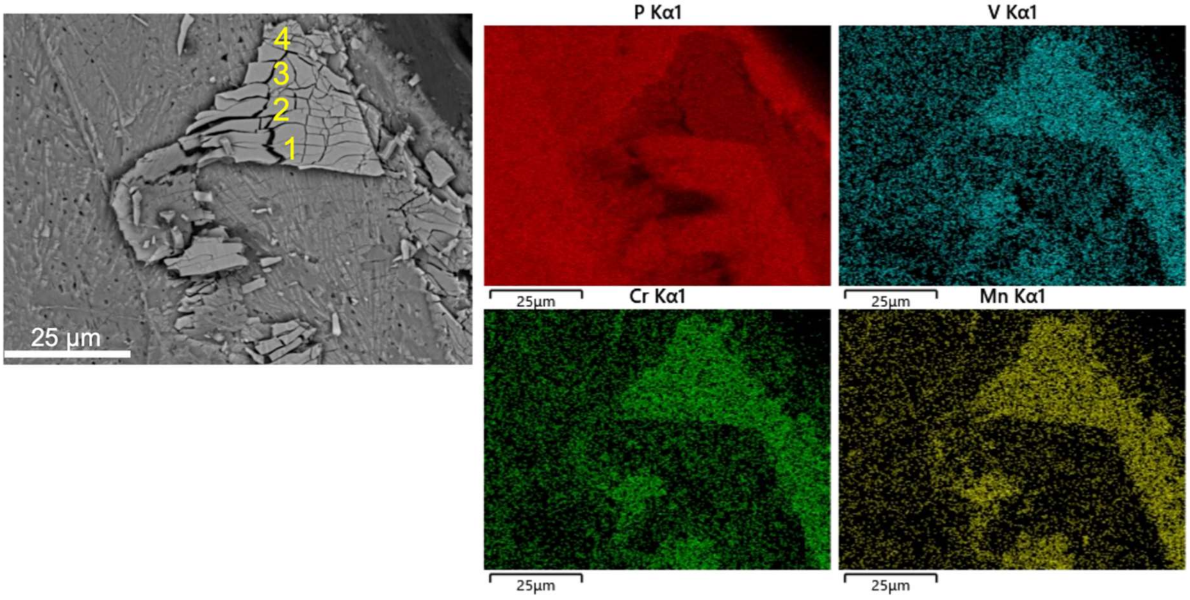

Figure 4-7 SEM and EDS mapping of the (V,Cr,Mn)-phosphide product. The numbers in the SEM image correspond to the EDS point analysis result shown in Table 4-5.

Table 4-5 The point analysis of (V,Cr,Mn)-phosphide correspond to Figure 4-7.

Point	V/at.%	Cr/at.%	Mn/at.%	P/at.%
1	7.97	5.81	7.53	78.68
2	8.18	5.96	7.36	78.50
3	7.72	5.79	7.01	79.49
4	7.67	5.48	7.16	79.69
Avg.	7.89	5.76	7.27	79.09

A high-resolution HAADF-STEM image of the (V,Cr,Mn)-phosphide on the [1-10] projection is presented in Figure 4-8. In this image, the brighter dots are metal elements, while the neighbor dimmer ones represent phosphorus. It should be noted that the sample drifted during the beam scan, which slightly distorted the observed STEM images. Nevertheless, the TEM analysis presents that the product can be explained well by a CrP_4-type structure and is consistent with XRD and SEM-EDS results. Although it was not possible to distinguish between different metal sites because of the close atomic numbers, and V, Cr, and Mn having almost the same atomic radius are expected to be mixed randomly in the structure based on the aforementioned results in the $(V,Cr)P_4$. The result strongly indicate that a pseudo-ternary phosphide of $(V,Cr,Mn)P_4$ can be synthesized using high pressure technique. To delve deeper into the effects of temperature and pressure on the lattice parameters, further investigation into the synthesis condition for this phosphide may be necessary.

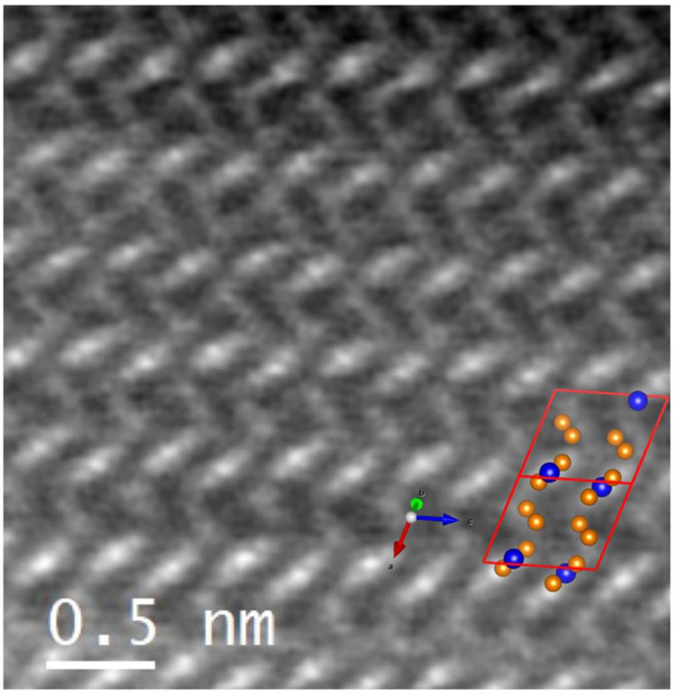

Figure 4-8 HAADF-STEM image of the (V,Cr,Mn)-phosphide on the [1-10] projection. The CrP_4-type crystal structure corresponding to the projected direction is also included in the figure (orange: phosphorus; blue: transition metals).

4.2.3 (V,Cr,Mo)P_4

Molybdenum, being the same group with chromium, but with larger atomic size is selected to examine how larger elements can affect the structure and behavior. The synthesis of (V,Cr,Mo)-phosphide under different conditions is detailed in Table 4-6. The tri-metal component (V,Cr,Mo)-phosphide was synthesized using mixed metal powder, similar to the case discussed in the previous section on pseudo-binary phosphide. Figure 4-9 presents the synchrotron X-ray diffraction pattern of V-Cr-Mo-P products prepared at P = 4 GPa, T = 1000 °C and t = 1 hour using the mixed powder in run26. From the inset of Figure 4-9, the enlarged pattern clearly shows three corresponding peaks close to the 110 peaks of MoP_4, VP_4, and CrP_4, respectively. This indicates a phase separation in the synthesized phosphide, even though it exhibits a CrP_4-type structure. It suggests that each transition metal in the mixed-metal-powder sample reacts with phosphorus individually, resulting in an inhomogeneous multi-phase product. This finding confirms the possible reason for the asymmetrical peak observed in the previous section (Figure 4-1). Therefore, similar to the synthesis of pseudo-binary phosphide discussed previously, the use of a transition metal alloy as the starting material is necessary.

Table 4-6 List of different experiment conditions done for finding the best synthesis condition for (V,Cr,Mo)-phosphide.

run#	starting metal form	metal:phosphorus ratio	pressure / GPa	temperature / °C	time / hour
10	mixed powder	1:4	5	1200	1
15	mixed powder	1:4	5	1200	1
16	mixed powder	1:5	6	1200	1
19	mixed powder	1:5	4	1200	1
20	mixed powder	1:5	4	1000	1
25	alloy	1:6	4	1100	1
26	alloy	1:6	4	1000	1
27	alloy	1:6	4	1000	2
28	alloy	1:6	4	900	0.5

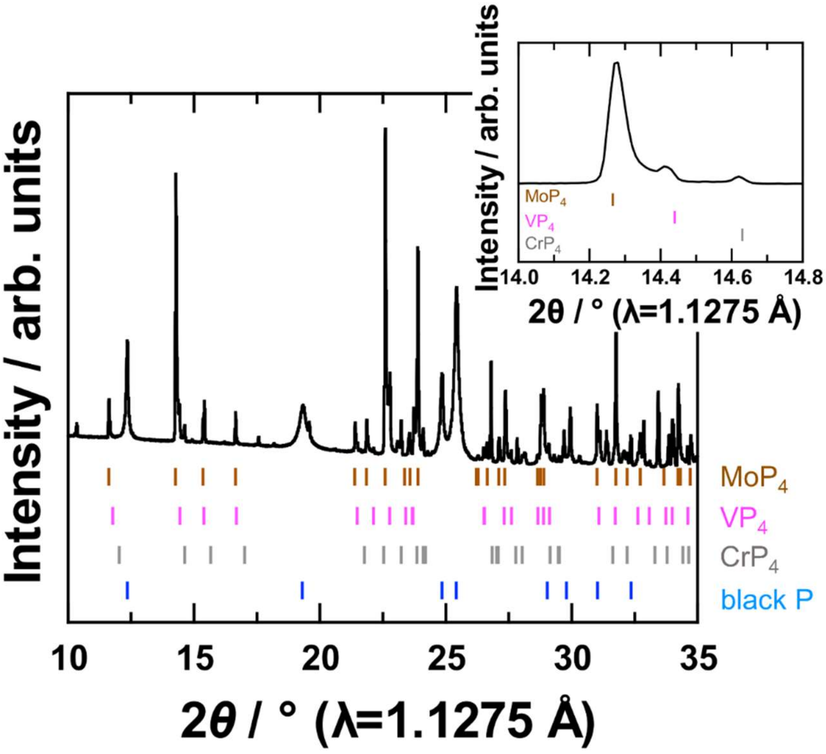

Figure 4-9 The synchrotron XRD pattern of starting materials V-Cr-Mo-P was made using simple mixing of the V, Cr, and Mo powders with red phosphorus. The synthesis conditions are mixed-metal-powder: P = 1: 5, P = 4 GPa, T = 1000 ℃ and t = 1 hour. The inset is the enlarged figure showing phase separation of the sample, the markers in the inset represent the 110 peaks of MoP_4, VP_4 and CrP_4.

The V-Cr-Mo alloy was characterized by SEM-EDS. Figure 4-10 taken at the polished alloy surface present that the elements are uniformly distributed (EDS point result correspond to Figure 4-10 is shown in Table 4-7). Then, the alloy was further treated by liquid quenching apparatus to produce rapidly solidified alloy ribbons. The alloy ribbons were then powdered and mixed with red phosphorus inside a glove box with a molar ratio of alloy: phosphorus =1: 6 for 30 minutes.

Several synthesis conditions for the (V,Cr,Mo)-phosphide were explored. Figure 4-11 depicts the conditions at P = 4 GPa and T = 1000 °C, with varying heating time. Run26 was heated for t = 1 hr. and run27 was heated for t = 2 hrs. The main phase of all different synthesis conditions is consistent with a CrP_4-type phosphide structure. However, with an extended heating time, the amount of black phosphorus remaining in the sample increased. The red arrows in the figure point to two of the peaks of black phosphorus, showing an increase of intensity with prolonged heating time. Additionally, in run26 and run27, especially run27, peaks corresponding to a BCC phase appear. SEM-EDS characterization of run27 is presented in Figure 4-12. V, Cr, and Mo rich areas with no phosphorus inclusion are found in the EDS mappings, showing a clear phase separation. This suggests that with a longer heating time, (V,Cr,Mo)-phosphide began to decompose, and it appears that the compound is not stable at high temperatures.

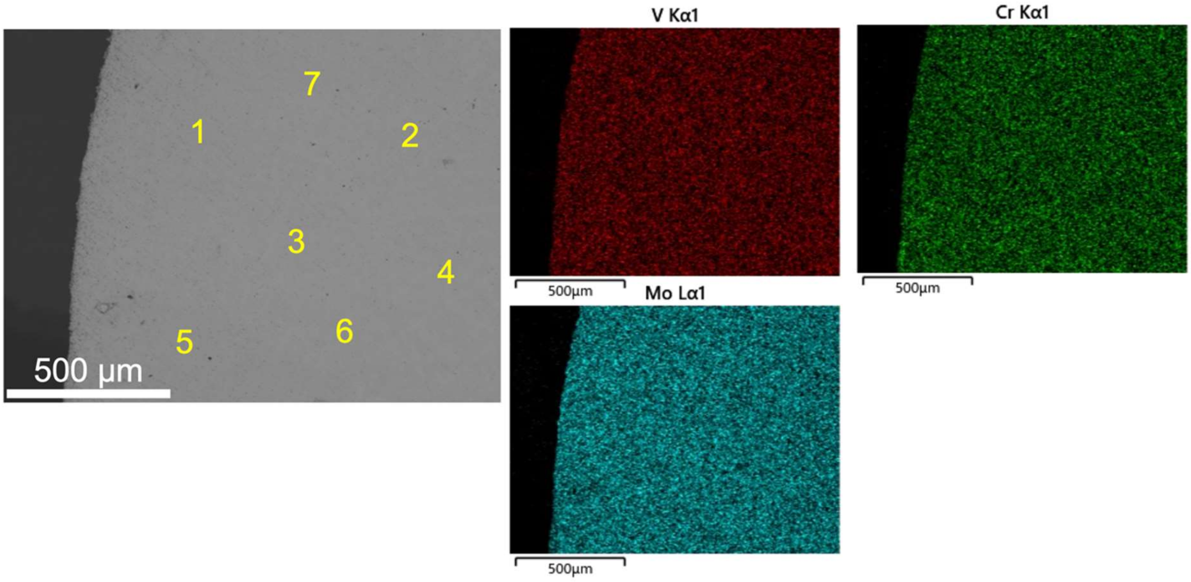

Figure 4-10 The SEM and EDS mapping of V-Cr-Mo alloy. The numbers correspond to EDS point analysis shown in Table 4-7.

Table 4-7 The EDS point analysis of the V-Cr-Mo alloy refer to Figure 4-10.

Point	V/at.%	Cr/at.%	Mo/at.%
1	35.09	30.65	34.26
2	35.12	30.08	34.80
3	35.15	28.94	35.90
4	35.69	31.06	33.26
5	35.77	29.50	34.72
6	35.41	31.89	32.70
7	34.65	28.42	36.94
Avg.	35.27	30.08	34.65
Std. Dev.	0.39	1.22	1.46

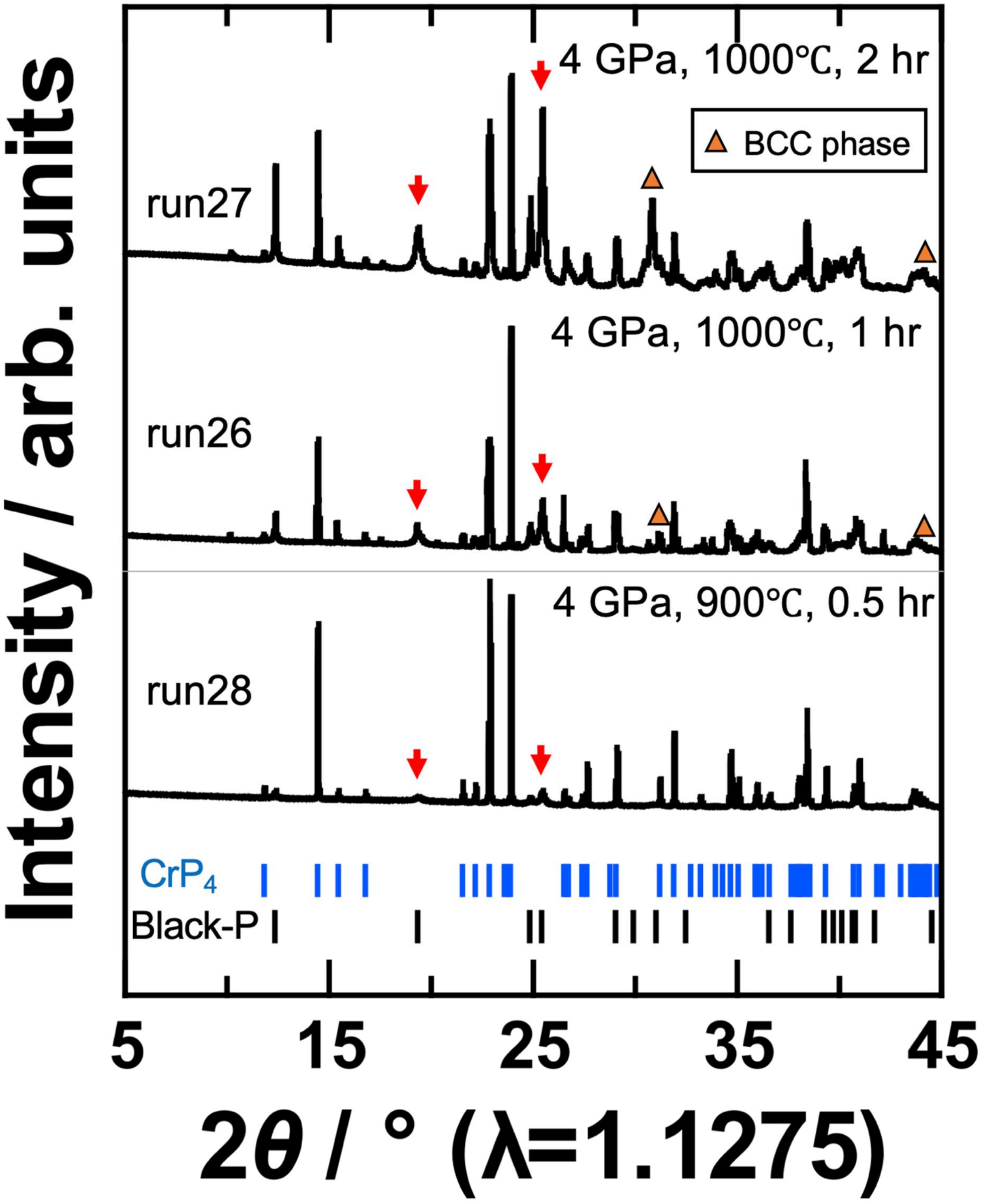

Figure 4-11 The synchrotron XRD pattern showing the (V,Cr,Mo)-phosphide sample synthesized at different conditions. The peaks for CrP_4-type structure and black phosphorus are also marked below.

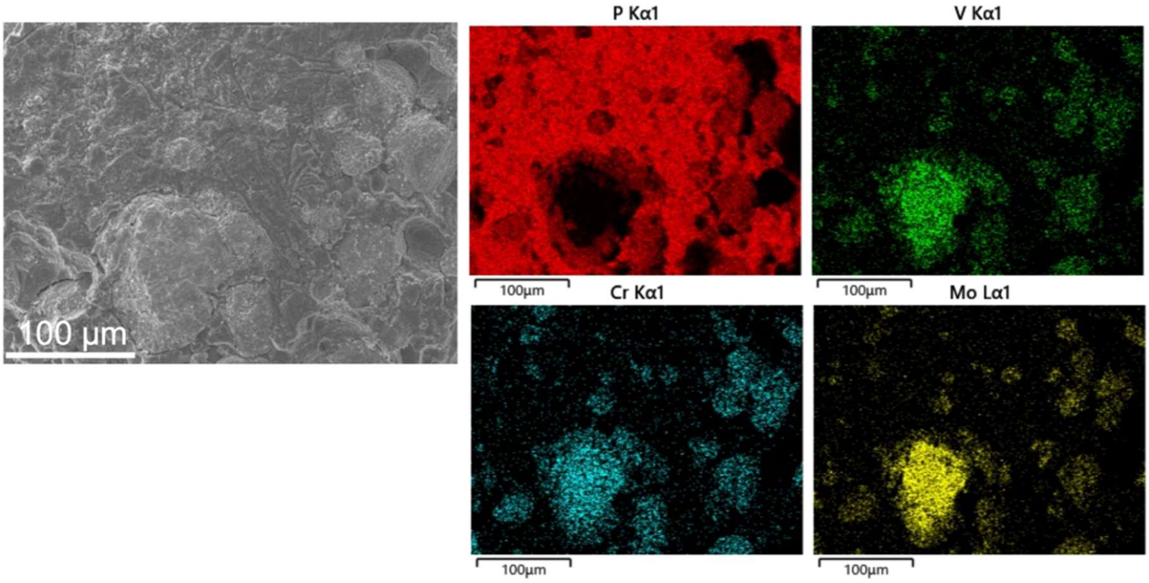

Figure 4-12 The SEM and EDS mapping of a fractured sample surface of run27. The mappings show that the sample has a metal element rich area, and the metal rich area has no phosphorus inclusion. Indicating a phase separation of the metal and phosphorus.

From the synthesis results mentioned above, the optimal synthesis conditions (single-phase, and no peak-splitting found in the XRD pattern) for (V,Cr,Mo)-phosphide was determined to be $P = 4$ GPa, $T = 900$ °C, and $t = 0.5$ hours (run28 in Figure 4-11). The following characterization was done using this sample, which is nearly a CrP_4-type single phase product with a small amount of black phosphorus.

The SEM image taken on a fractured piece of the sample (run28 in Figure 4-11) is presented in Figure 4-13. The EDS result taken on a comparably flat surfaces is shown in Table 4-8. The EDS mappings (Figure 4-13) show that V, Cr, and Mo are uniformly distributed throughout the sample. The composition of transition metals is almost equimolar and the overall composition of metal to phosphorus is approximately 1:4, suggesting a $(V,Cr,Mo)P_4$ composition.

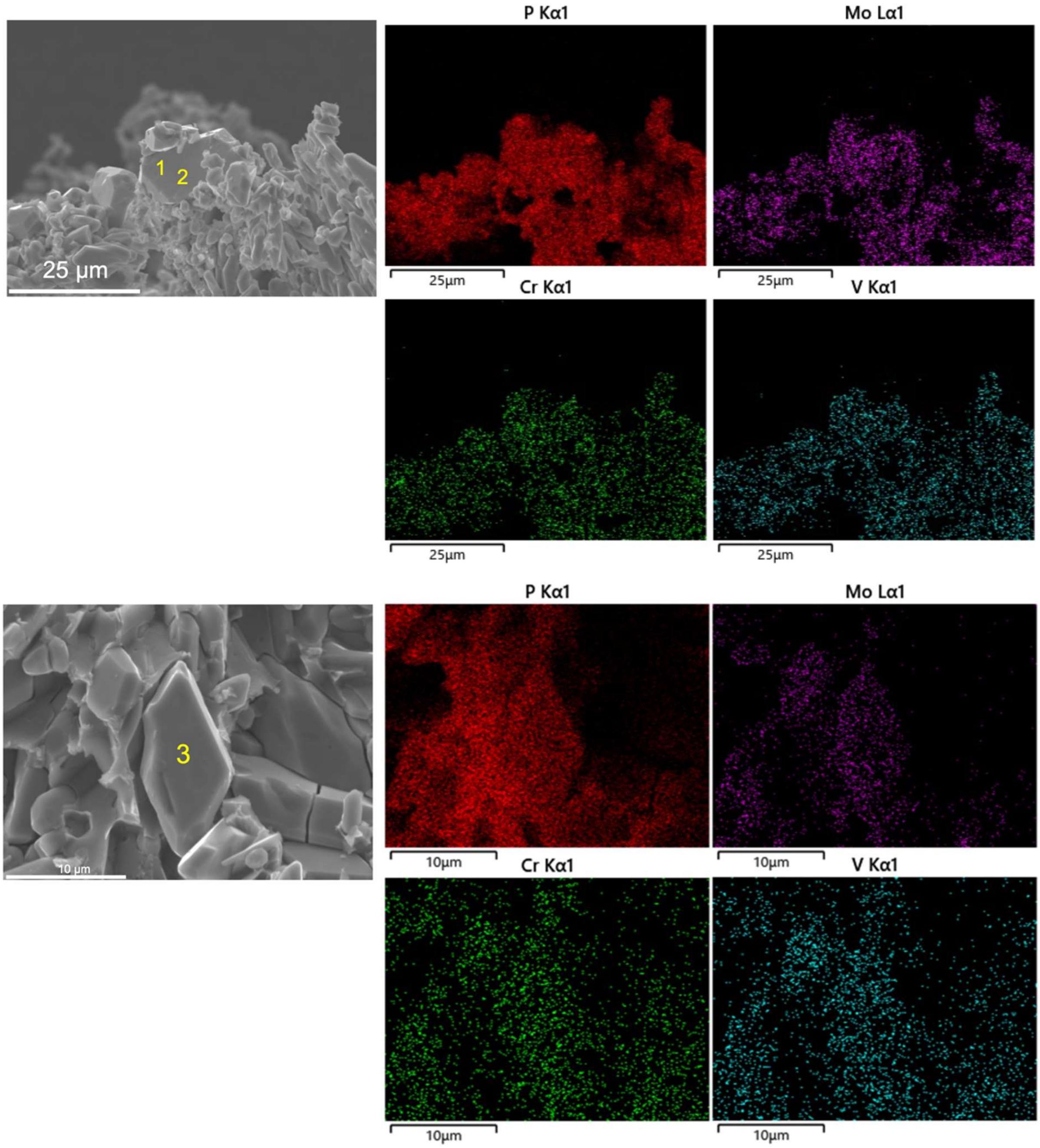

Figure 4-13 SEM and EDS characterization of the high-pressure synthesized sample at different area in the sample. The EDS analysis results are shown in Table 4-8.

Table 4-8 Point analysis result of synthesized sample (refer to Figure 4-13).

Point	V/at.%	Cr/at.%	Mo/at.%	P/at.%
1	6.37	6.76	7.30	79.56
2	6.23	6.66	7.84	79.27
3	7.33	8.00	5.19	79.48
Avg.	6.64	7.14	6.78	79.44

To confirm the homogeneity of the sample, STEM characterization was performed. The HAADF-STEM image on the [001] projection of the sample is shown in Figure 4-14a, accompanied by contrast analysis results presented in Figure 4-14b and Figure 4-14c. Compared to vanadium and chromium, molybdenum is larger in atomic size and has a higher atomic number (the atomic radii for V, Cr, and Mo are 1.71 Å, 1.66 Å, and 1.90 Å, respectively) [79]. Generally, larger atoms have difficulties in integrating into the lattice of smaller atoms, often leading to the formation of a secondary phase or partial precipitation resulting in clustering and inhomogeneity. Given the higher atomic number of Mo, its columns should be distinguishable in the atomic-scale STEM images if there is clear clustering in the sample. However, the intensities of the signals remain constant across all points, suggesting a homogenous distribution of Mo throughout the structure. The gradual decrease in intensity observed in the STEM image is attributed to the varying sample thickness, with the left side being thicker than the right. Despite the size difference among V, Cr, and Mo, these transitional metals are uniformly incorporated into the same structure, as corroborated by the EDS analysis. This all confirms the sample is a homogeneous CrP_4-type phosphide $(V,Cr,Mo)P_4$.

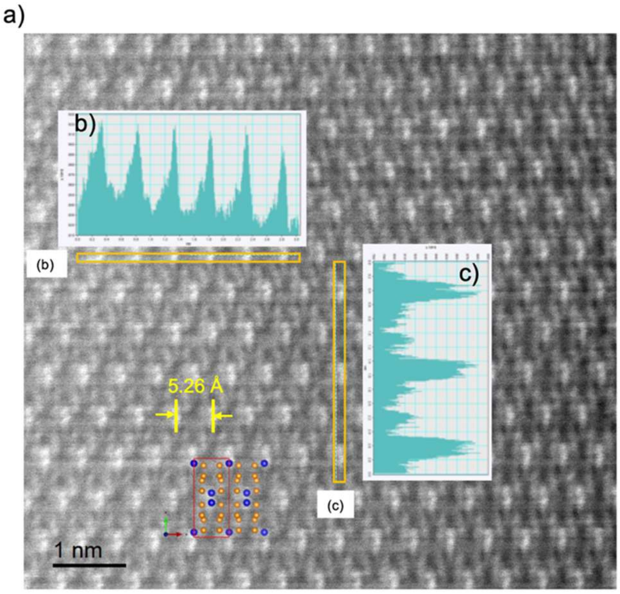

Figure 4-14 The STEM analysis of a) [001] projection HAADF image of (V,Cr,Mo)P_4 and the corresponding contrast profiles of transition metal sites in b) horizontal direction and c) in the vertical direction (the analysis lines are also marked in the HAADF image). The intensity of the contrast profiles represents the position of atoms; a metal-metal distance of 5.26 Å corresponds to the *a*-axis direction and is consistent with the lattice parameter for (V,Cr,Mo)P_4. The crystal structures corresponding to the projected directions are also shown in the images (orange: phosphorus; blue: transition metals).

Based on these characterization results, and assuming the transition metal ratio is 1:1:1, i.e., equimolar, Figure 4-15 is the result of Rietveld refined XRD pattern. The XRD pattern can be refined well with a CrP_4-type structure and the calculated and observed profile has R_{wp} = 4.966 %, R_{p} = 3.771 %, R_{B} = 2.773 % and R_F = 1.795 % with goodness of fit S = 2.0729. The cell parameters are listed in Table 4-9, where a = 5.25845(6) Å, b = 10.95557(11) Å, c = 5.82652(5) Å, β = 110.7770(6) °, and V = 313.833(6) Å^3. The atomic coordinates and isotropic atomic displacement parameters are listed in Table 4-10.

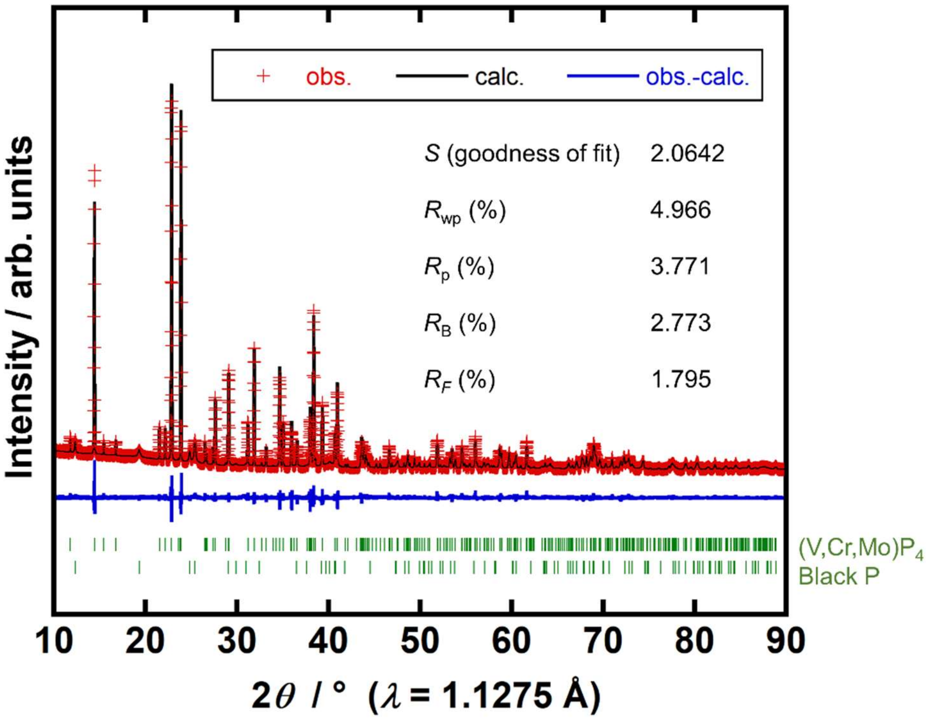

Figure 4-15 Rietveld refinement of the synchrotron XRD pattern at 293 K. The green markers from top to down represent (V,Cr,Mo)P_4, and black phosphorus, respectively. Their mass fractions are (V,Cr,Mo)P_4: 84.6%; black phosphorus: 15.4%.

Table 4-9 Cell parameters for the Rietveld-refined (V,Cr,Mo)P_4.

Compound	(V,Cr,Mo)P_4
Formula Weight (g/mol)	190.197
Space Group	*C*2/*c* (No.15)
a (Å)	5.25845(6)
b (Å)	10.95557(11)
c (Å)	5.82652(5)
β (°)	110.7770(6)
V (Å^3)	313.833(6)
Z	4
D_{calc} (g/cm^3)	4.0254

Table 4-10 Atomic position, occupancies, and isotropic atomic displacement parameters for (V,Cr,Mo)P_4.

Atom	Site	Occ.[a]	x	y	z	B (Å^2)
P1	8f	1	0.2240(2)	0.40903(10)	0.3213(2)	0.25(2)
P2	8f	1	0.2755(2)	0.22230(10)	0.1889(2)	=P1
V/Cr/Mo	4e	0.3333/0.3333/0.3334	0	0.06109(8)	1/4	0.08(2)

[a] the occupancy of phosphorus is fixed to 1, and the metal site is assumed to be equimolar.

4.3 Pseudo-quaternary and -quinary phosphide

The search for pseudo-quaternary and -quinary phosphide was also undertaken. List of the conditions are shown in Table 4-11. However, currently, the included phases in the patterns are too complicated and cannot be identified (e.g., Figure 4-16 present one of the sample runs). The probable reason for this complexity may be attributed to the use of starting metal material, which necessitate pre-treatment into alloy form, as discussed in previous sections. Nevertheless, further investigation is required.

Table 4-11 List of different experiment conditions done for synthesizing pseudo-quaternary and -quinary phosphide.

	Run#	starting metal form	metal:phosphorus ratio	Pressure / GPa	temperature / °C	time / hour
(V, Cr, Mn, Mo)-P	17	Mixed powder	1:5	5	1200	1
(V, Cr, Mn, Fe, Mo)-P	2	Mixed powder	1:4	5	1200	1
(V, Cr, Mn, Fe, Mo)-P	3	Mixed powder	1:4	5	1000	1
(V, Cr, Mn, Fe, Mo)-P	4	Mixed powder	1:4	5	1400	1

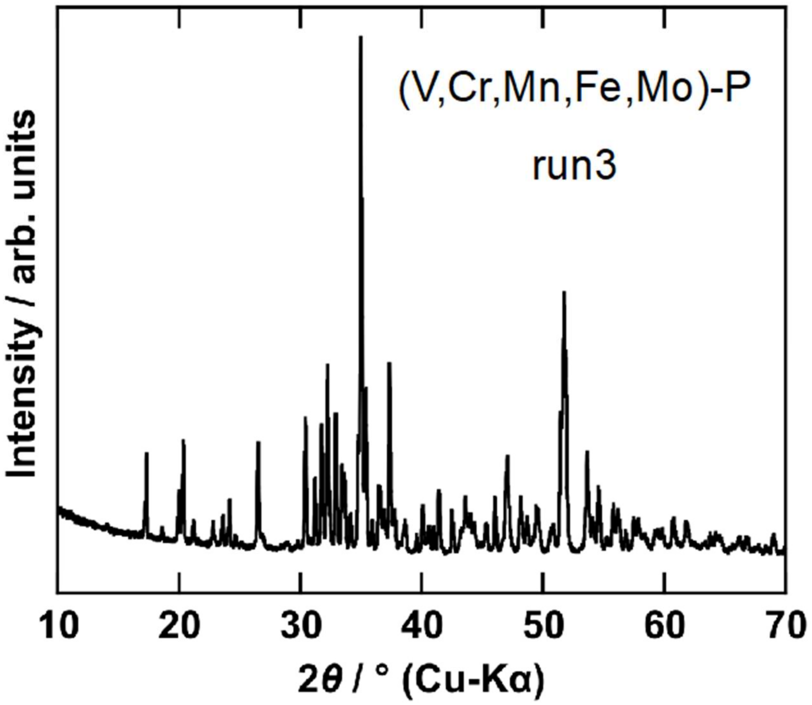

Figure 4-16 The XRD pattern of a five-metal component phosphide synthesized under high-pressure.

4.4 Multicomponent effect on crystal structure of CrP_4-type phosphides

The multicomponent effect on the lattice parameters and volume of the CrP_4-type phosphides under ambient pressure and room temperature conditions is compared. To understand their relationships, the crystal structure of the CrP_4-type phosphide is explained. The discussion on the lattice parameters begins with the binary phosphides VP_4, CrP_4 and MoP_4.

The CrP_4-type crystal structure viewed from different angles and directions, is presented in Figure 4-17. The CrP_4 -type structure is a stacking of two-dimensional black phosphorus layers, the armchair direction of black phosphorus is aligned in the *a*-axis (Figure 4-17a), and the transition metal atoms are incorporated in between the layers of black phosphorus. They are octahedrally bonded to phosphorus and form an octahedron. Each octahedron is edge-shared with one another along the *c*-axis (Figure 4-17b), creating a zigzag octahedron chain.

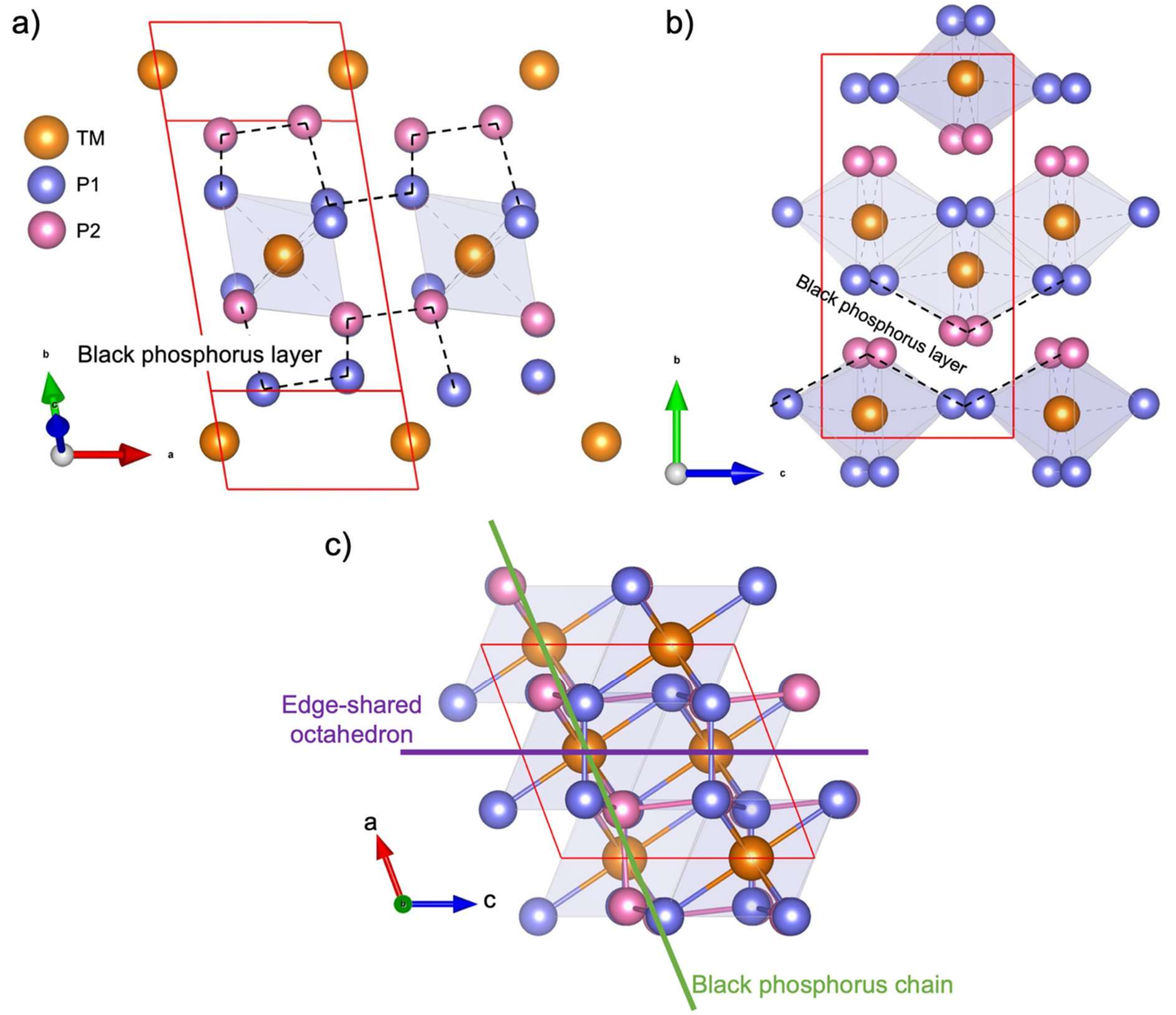

Figure 4-17 The CrP_4-type crystal structure viewing from different angle and direction. a) Viewing at an angle showing the black phosphorus layer. b) Viewing from *a*-axis direction. c) viewing from *b*-axis direction. The direction of black phosphorus chain (shown in (a)) and the edge-shared octahedron (shown in (b)) are also marked in (c). The transition metal (TM) is marked in orange, and the phosphorus P1 and P2 sites are marked in blue and pink, respectively.

The Rietveld refinement results of the binary phosphides (VP_4, CrP_4, and MoP_4) are shown in Figure 4-18 to Figure 4-20 (refinement details are shown in Table 4-12 and Table 4-13). The lattice parameters of the CrP_4-type phosphides at room temperature (298 K) and ambient pressure are summarized in Table 4-14 and illustrated in Figure 4-21. The unit cell volumes of endmember binary phosphides increase in the order of CrP_4, VP_4, and MoP_4 which can be explained by the size differences among V, Cr, and Mo. However, the lattice parameters of MoP_4 do not follow the size relationship. MoP_4 has the longest *a*- and *b*-axis among endmember binary phosphides, but *c*-axis and β-angle of MoP_4 are shorter than VP_4.

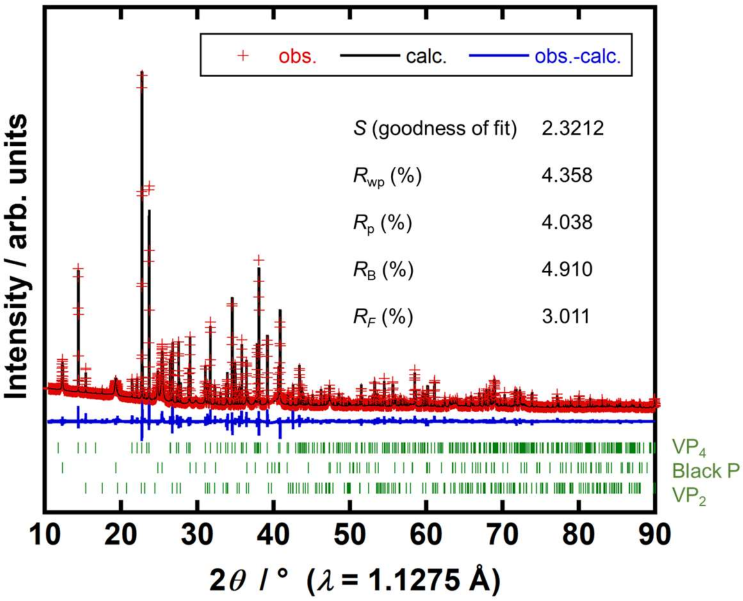

Figure 4-18 Rietveld refinement of VP_4 synchrotron XRD pattern at 293 K. The green markers from top to down represent VP_4, black phosphorus, and VP_2 respectively. Their mass fractions are VP_4: 51.7%; black phosphorus: 36.4%; VP_2: 11.9%.

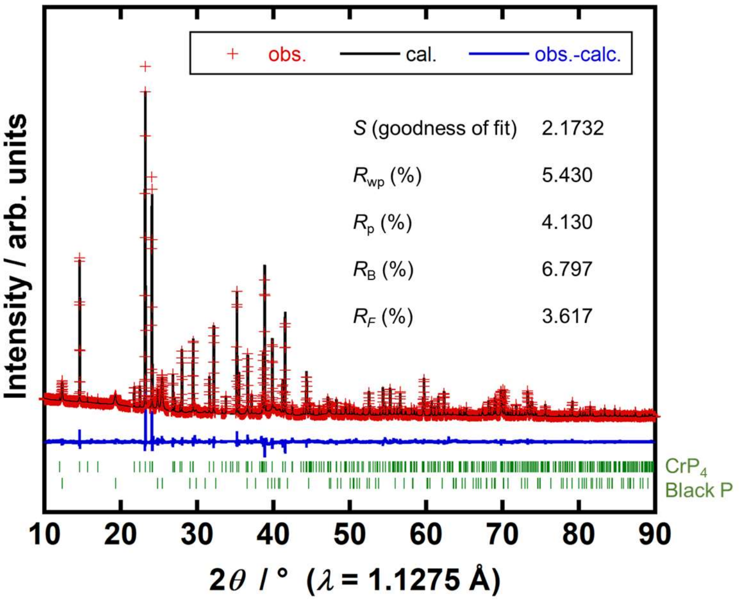

Figure 4-19 Rietveld refinement of CrP_4 synchrotron XRD pattern at 293 K. The green markers from top to down represent CrP_4, and black phosphorus, respectively. Their mass fractions are CrP_4: 73.4%; black phosphorus: 26.6%.

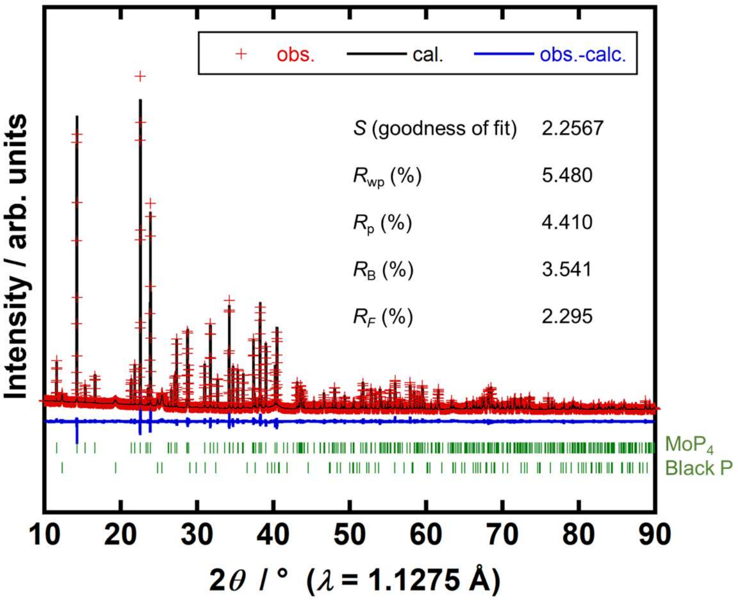

Figure 4-20 Rietveld refinement of MoP_4 synchrotron XRD pattern at 293 K. The green markers from top to down represent MoP_4, and black phosphorus, respectively. Their mass fractions are MoP_4: 79.1%; black phosphorus: 20.9%.

Table 4-12 Cell Parameters for the Rietveld-refined VP_4, CrP_4, and MoP_4.

Compound	VP_4	CrP_4	MoP_4
Formula Weight (g/mol)	174.837	175.891	219.855
Space Group	*C*2/*c* (No.15)	*C*2/*c* (No.15)	*C*2/*c* (No.15)
a (Å)	5.26467(3)	5.19374(3)	5.31242(2)
b (Å)	10.98681(6)	10.76544(6)	11.14933(4)
c (Å)	5.87317(4)	5.77146(4)	5.82273(3)
β (°)	110.8640(4)	110.6378(4)	110.6397(3)
V ($Å^3$)	317.439(3)	301.991(3)	322.740(2)
Z	4	4	4
Dcalc (g/cm^3)	3.6583	3.8686	4.5247

Table 4-13 Atomic position, occupancies, and isotropic atomic displacement parameters for VP_4, CrP_4, and MoP_4.

VP_4	Atom	Site	Occ.[a]	x	y	z	B (Å^2)
	P1	8f	1	0.2238(3)	0.40952(11)	0.3223(3)	0.58(3)
	P2	8f	1	0.2755(3)	0.22335(11)	0.1885(3)	0.62(3)
	V	4e	1	0	0.06276(12)	¼	0.55(3)
CrP_4	Atom	Site	Occ.[a]	x	y	z	B (Å^2)
	P1	8f	1	0.2258(3)	0.41156(12)	0.3216(3)	0.68(3)
	P2	8f	1	0.2741(3)	0.22117(13)	0.1898(3)	0.74(3)
	Cr	4e	1	0	0.06240(13)	¼	0.70(3)
MoP_4	Atom	Site	Occ.[a]	x	y	z	B (Å^2)
	P1	8f	1	0.2211(2)	0.40522(9)	0.3161(2)	0.66(2)
	P2	8f	1	0.2782(2)	0.22184(10)	0.1895(2)	0.74(2)
	Mo	4e	1	0	0.05885(5)	¼	0.48(1)

[a] the occupancy is fixed to 1.

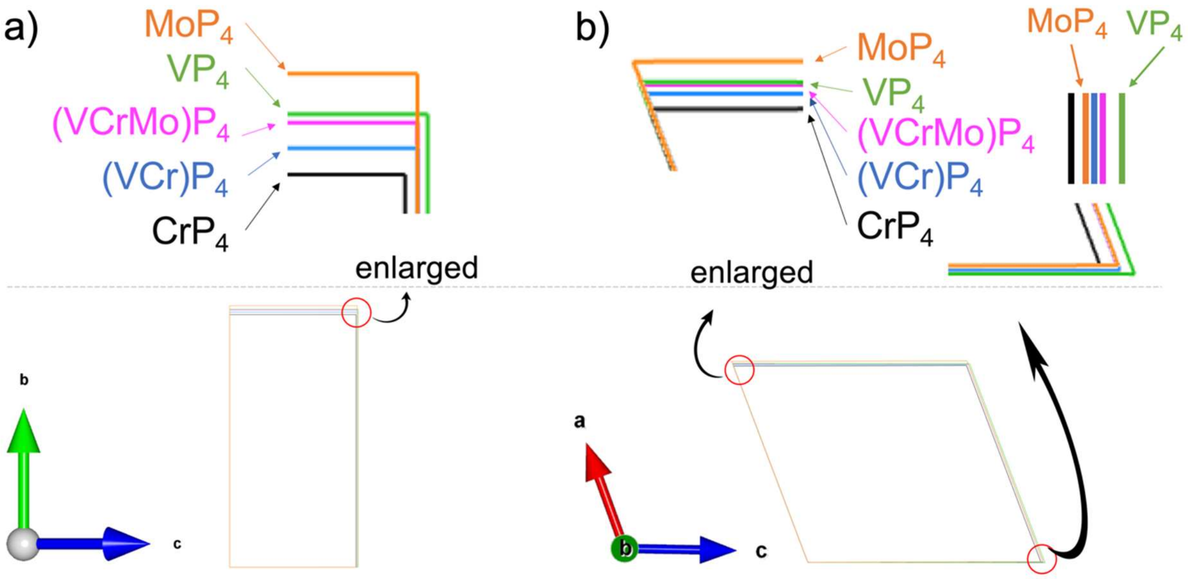

Figure 4-21 Graph showing the unit cell size relationships between the different CrP$_4$-type binary phosphides. The unit cells are illustrated using VESTA program [13] and the unit cells are aligned to bottom-left corner. The unit cells are enlarged to show the size and angle differences between each phosphide. Each figure corresponds to the view from a) *a*-axis and b) *b*-axis directions.

Table 4-14 Summarized lattice parameters and cell volume of the multicomponent phosphides and its end-member phosphides.

	a / Å	*b* / Å	*c* / Å	*β* / °	V / Å^3	*ref.*
VP_4	5.26467(3)	10.98681(6)	5.87317(4)	110.8640(4)	317.439(3)	This study
	5.263	10.98	5.871	110.88	317	[80]
	5.259(4)	10.997(7)	5.879(6)	110.87(7)	317.7(2)	[81]
CrP_4	5.19374(3)	10.76544(6)	5.77146(4)	110.6378(8)	301.990(3)	This study
	5.1914(5)	10.7600(8)	5.7712(6)	110.648(6)	301.67(6)	[78]
	5.1944(3)	10.7736(5)	5.7758(3)	110.606(2)	301.76(3)	[82]
MoP_4	5.31242(2)	11.14922(3)	5.82273(3)	110.6397(3)	322.740(2)	This study
	5.313(2)	11.139(7)	5.820(2)	110.64(4)	322.4(4)	[78]
	5.3131(6)	11.1588(9)	5.7343(6)	110.638(12)	323.70(6)	[83]
$(V,Cr)P_4$	5.23133(5)	10.86133(8)	5.82576(6)	110.7800(6)	309.483(5)	[84]
	5.229	10.876	5.822	110.751	309.71	*a*
$(V,Cr,Mo)P_4$	5.25845(6)	10.95557(11)	5.82652(5)	110.7770(6)	313.833(6)	This study
	5.257	10.967	5.822	110.714	314.06	*a*

[a] Value calculated from the average of the end-member binary phosphides.

The structural difference of the binary endmember phosphides is compared in more detail. Table 4-15 summarizes the bond lengths and angles of the binary phosphides. The enlarged figure showing the connected edge-sharing octahedra aligns along the *c*-axis is presented in Figure 4-22. VP_4 has a longer *c*-axis but shorter *a*- and *b*-axis than MoP_4 (Figure 4-21 and Table 4-14), indicating that the zigzag connected octahedron in VP_4 is elongated in the *c*-axis direction and shrinks in the *a*, *b*-axes directions. As seen from the M-P1-M (θ4) angle relationship between the phosphides, the larger atom results in a more 'bended' zigzag octahedra chain. The volumes of the octahedra in VP_4 and MoP_4 are almost the same. The M-P distances represent the octahedra bonds, and from longest to shortest, VP_4>MoP_4>CrP_4. Despite Mo having the largest atomic size, MoP_4 has a shorter octahedron bonding distance than that of VP_4. Assuming the ideal octahedron angle is about 90°, the larger P-M-P angles deviating from 90° represent a more distorted octahedron. So, MoP_4 has the most distorted octahedra. Even with a larger atomic size, the octahedra volume of MoP_4 remains almost the same as that of VP_4 while the octahedron is more distorted. Thus, it is possible that the size of Mo is the limit for the octahedra that can be tolerated in the CrP_4-type structure. As a result, this structural difference gives MoP_4 the observed lattice parameter differences that cannot be explained by the element size relationship. Nevertheless, as shown in Table 4-14, the volume and lattice parameters of the multicomponent phosphides, $(V,Cr)P_4$ and $(V,Cr,Mo)P_4$ present to be the average of the endmembers. Meaning that there is no significant multicomponent effect in the multicomponent phosphides.

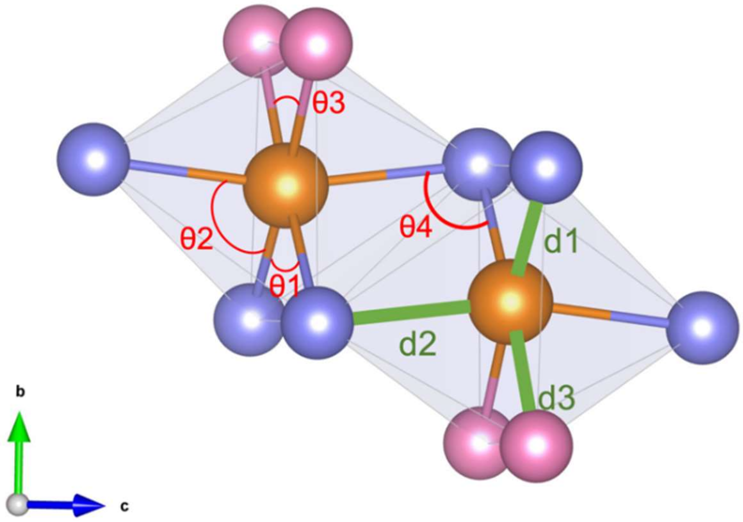

Figure 4-22 The enlarge part of the structure showing the edge-shared octahedrons, the bonding distance labeled d1-d3, and the angles labeled θ1-θ4 correspond to Table 4-15.Table 4-15. The M-M distance in Table 4-15Table 4-15 is the distance of the metals between the edge-shared octahedra. The transition metals (TM) are colored orange, and the phosphorus P1 and P2 are colored blue and pink, respectively.

Table 4-15 Bond lengths and angles between phosphorus (P1 and P2) and transition metal (M) of the phosphides VP_4, CrP_4, and MoP_4.

		VP_4	CrP_4	MoP_4
bond length / Å				
(d1)	M-P1 (×2)	2.3604(17)	2.2911(17)	2.3831(12)
(d2)	M-P1 (×2)	2.4321(16)	2.3953(15)	2.4698(10)
(d3)	M-P2 (×2)	2.3918(17)	2.3278(17)	2.4446(13)
	M-M	3.2447(10)	3.1832(10)	3.1934(5)
angle / °				
(θ1)	P1-M-P1	88.95(9)	89.76(9)	88.10(6)
(θ2)	P1-M-P1	94.79(5)	94.46(5)	97.72(4)
(θ3)	P2-M-P2	84.93(9)	85.49(9)	83.99(6)
(θ4)	M-P1-M	85.21(5)	85.54(5)	82.28(4)
octahedra volume / $Å^3$		18.1298	16.8936	18.8703

4.5 Thermal expansion and compression behaviors

4.5.1 Thermal stability and expansion

In Chapter 4.4, the structural dissimilarity among the binary, pseudo-binary, and pseudo-ternary CrP_4-type phosphides at room temperature was understood through the difference in their edge-shared octahedron. It should be noted that the structure of the CrP_4 -type phosphide has a monoclinic unit cell and the characteristic black phosphorus layer structure as well as the transition metal edge-sharing octahedron chain are aligned at an angle β (monoclinic unit cell angle). Understanding the structural behavior three-dimensionally becomes extremely difficult. For simplicity, the structure is examined from the characteristic black phosphorus layer. Here, the temperature-dependent structural behavior of the binary, pseudo-binary and pseudo-ternary CrP_4-type phosphides is also reviewed based on the change in their characteristic black phosphorus layers as a function of temperature. Particularly, the behaviors of the multicomponent pseudo-binary and pseudo-ternary CrP_4-type phosphides, i.e. $(V,Cr)P_4$ and $(V,Cr,Mo)P_4$, are understood based on those of the endmembers binary phosphides.

From the low-temperature XRD data (Figure 4-23 and Figure 4-24), the XRD profile of the binary, pseudo-binary and pseudo-ternary CrP_4-type phosphides did not show any appearance of additional peaks as the temperature changed. The normalized change of the axes with respect to the temperature is calculated and plotted in Figure 4-25. The smooth change throughout the temperature range without discontinuity indicates that the structure did not undergo any phase transformation at the measured temperature range. In Figure 4-26 the temperature-dependent volume and lattice parameters of the phosphides are plotted together. The volume, *a*- and *b*-axis show the same order of MoP_4>VP_4>(V,CrMo)P_4>(V,Cr)P_4>CrP_4 from largest to smallest. However, the *c*-axis and *β*-angle have a different relationship. CrP_4 is observed to have high temperature dependency, and its lattice parameters change the most. (V,CrMo)P_4 and (V,Cr)P_4 on the other hand, have almost no temperature dependency compare to CrP_4.

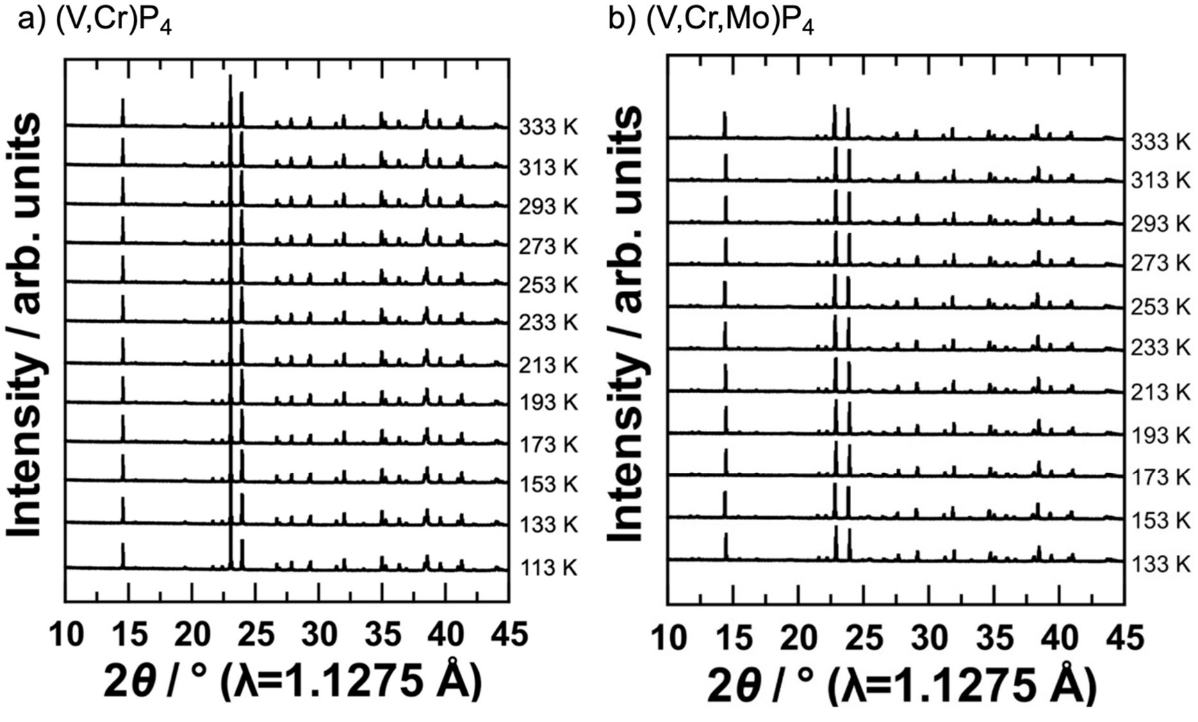

Figure 4-23 *In-situ* low-temperature synchrotron XRD pattern of a) (V,Cr)P_4 and b) (V,Cr,Mo)P_4. No additional peaks are observed during cooling; the synthesized samples are stable to low temperature.

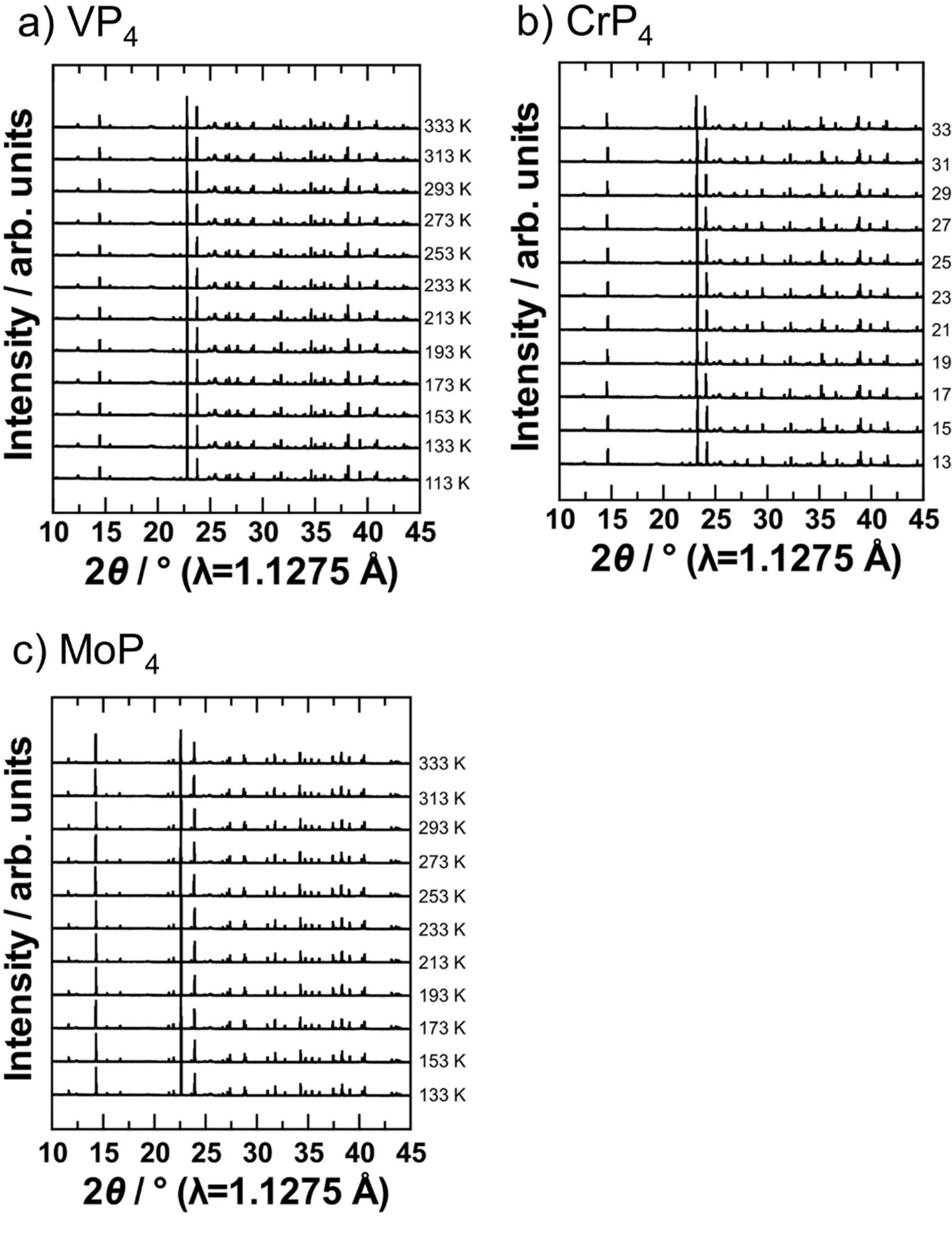

Figure 4-24 The low-temperature synchrotron XRD pattern of a) VP$_4$, b) CrP$_4$ and c) MoP$_4$. No additional peaks are observed during cooling.

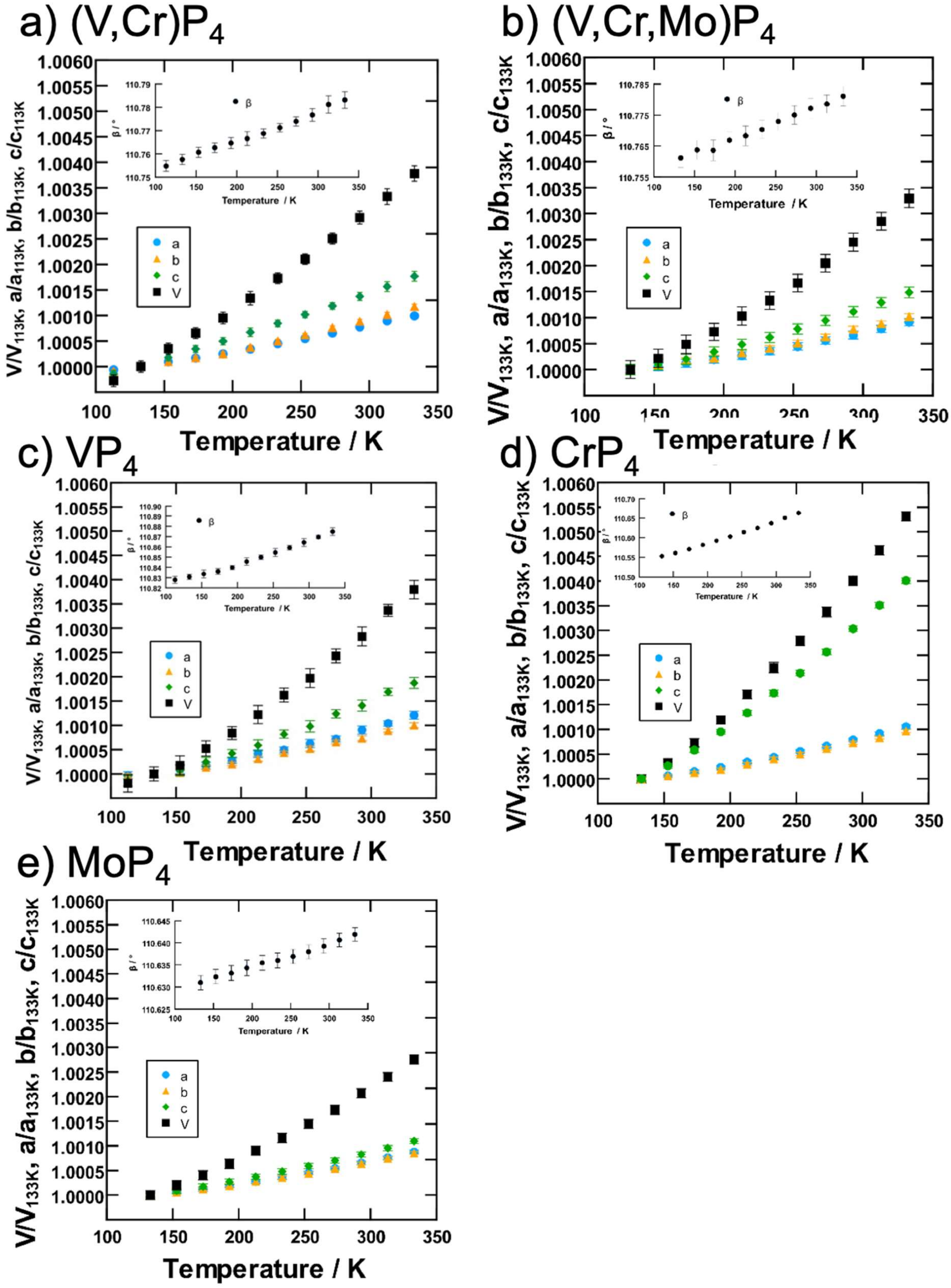

Figure 4-25 The temperature-dependent normalized axis change of a) (V,Cr)P_4, b) (V,Cr,Mo)P_4, c) VP_4, d) CrP_4 and e) MoP_4. The inset is the temperature dependent change of *β*-angle.

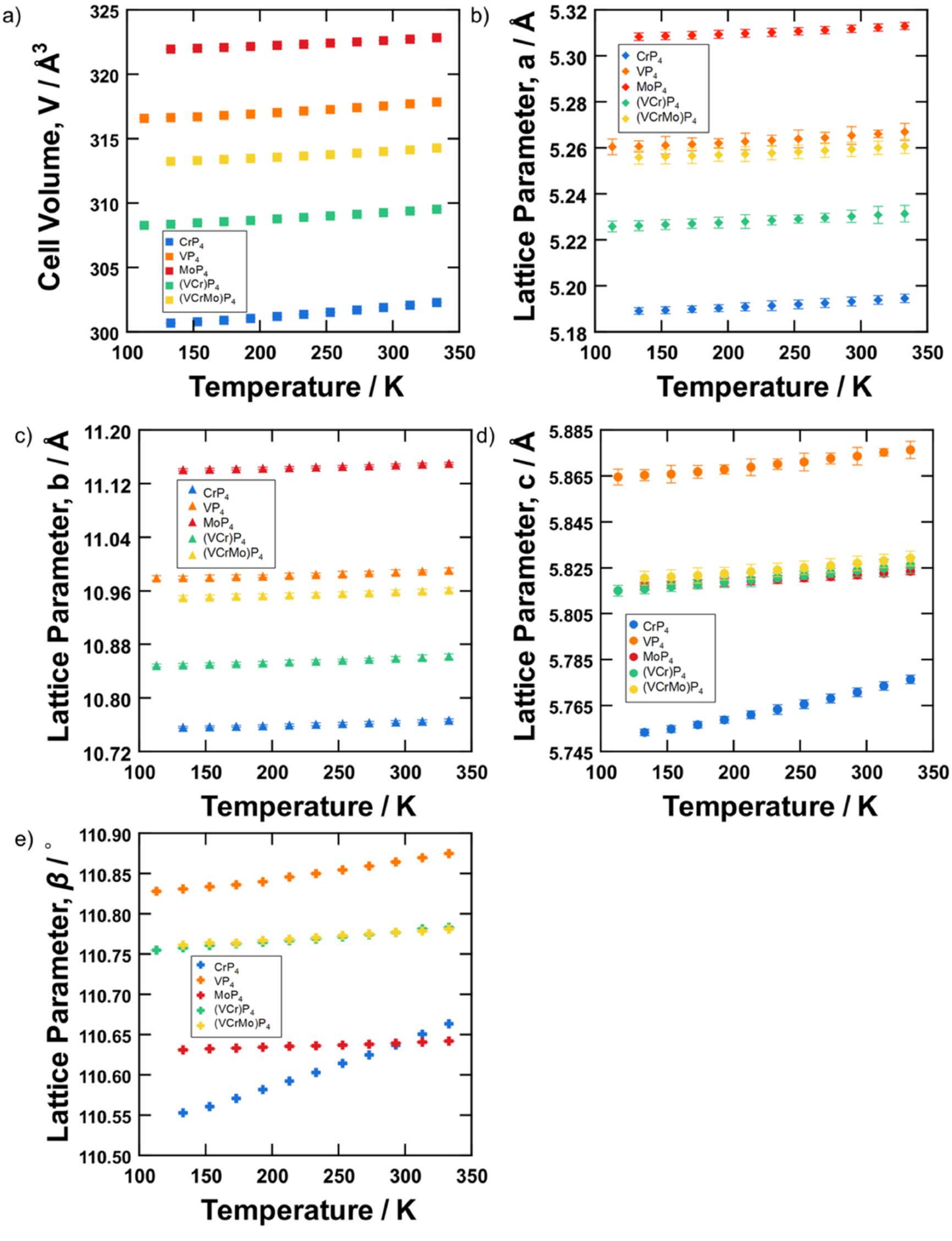

Figure 4-26 Temperature-dependent lattice parameter behaviors of the endmembers and the multicomponent phosphide. The figures represent the comparison of their a) cell volume, b) *a*-axis, c) *b*-axis, d) *c*-axis, and e) angle *β*.

The coefficient of thermal expansion (CTE, *α*) has been calculated using the approach described in Chapter 2.3. The CTE values are plotted in Figure 4-27. The CTE values at 293 K for the binary, pseudo-binary and pseudo-ternary CrP_4-type phosphides are summarized in Table 4-16. The general CTE equations for all the axes and volume of the phosphides are shown in Table 4-17. The *c*-axis has the highest CTE than the *a*- and *b*-axis, and the *a*- and *b*-axis have close CTE values. This indicates that the *c*-axis is more expandable than the *a*- and *b*-axis. This thermal expansion behavior is the change in the zigzag-aligned edge-shared octahedron described in Figure 4-17b. The black phosphorus armchair chain that aligns in the *a*-axis direction and the black phosphorus stacking layers (*b*-axis) shown in Figure 4-17a have less change.

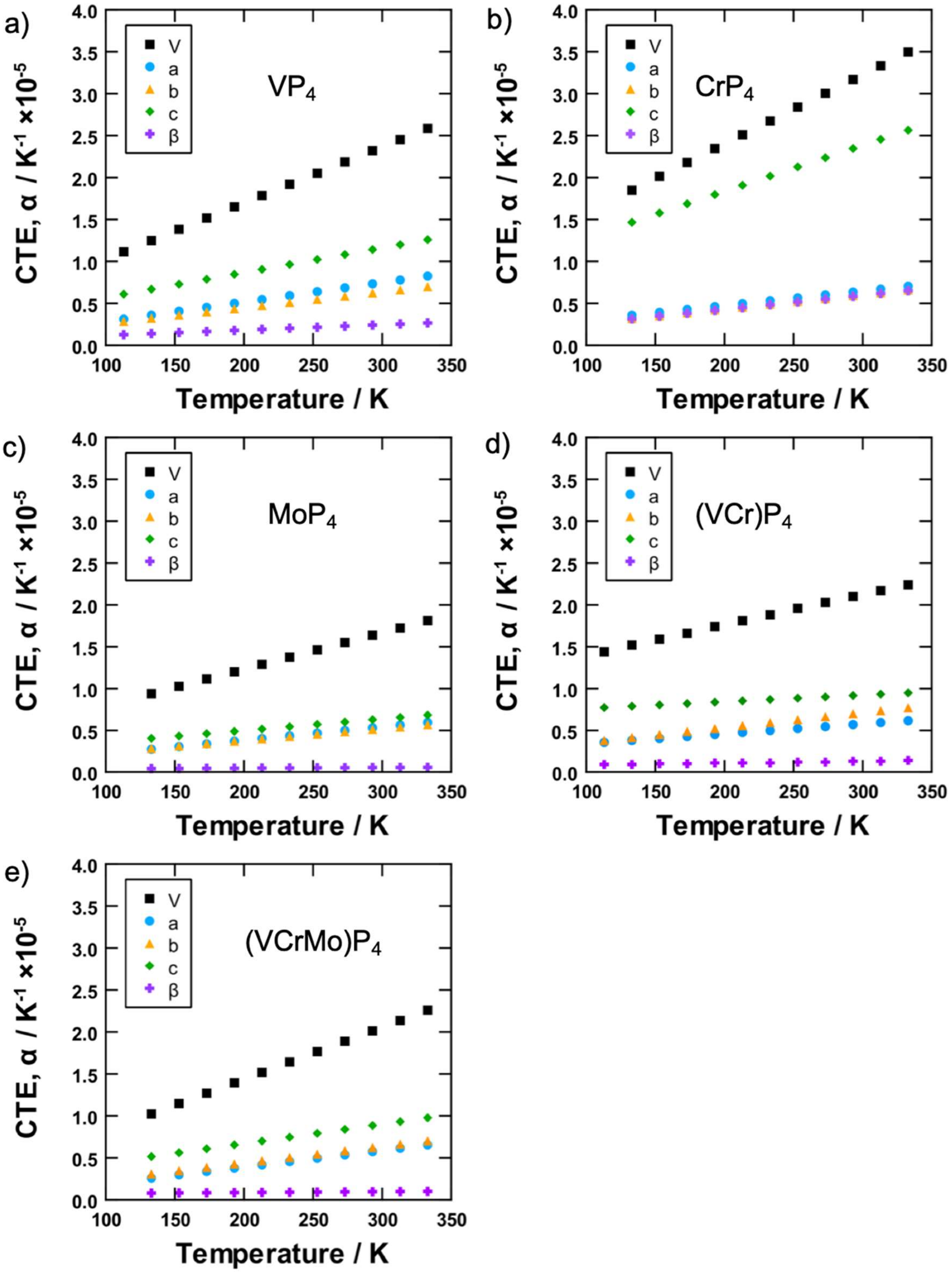

Figure 4-27 The plot of temperature dependent CTE change of the phosphides. a) VP_4, b) CrP_4, c) MoP_4, d) the pseudo-binary $(V,Cr)P_4$, and e) the pseudo-ternary $(V,Cr,Mo)P_4$

Table 4-16 The calculated coefficient of thermal expansion (CTE) at 293 K for VP_4, CrP_4, MoP_4, $(V,Cr)P_4$ and $(V,Cr,Mo)P_4$.

	CTE, α x 10^{-5} K^{-1}				
	α_V	α_a	α_b	α_c	α_β
VP_4	2.32	0.73	0.62	1.14	0.24
CrP_4	3.17	0.63	0.59	2.35	0.58
MoP_4	1.64	0.53	0.51	0.63	0.05
$(V,Cr)P_4$	2.10	0.57	0.70	0.92	0.13
$(V,Cr,Mo)P_4$	2.01	0.57	0.62	0.89	0.10

Table 4-17 Summary of general CTE expressions for *a*-, *b*-, *c*- axes, β angle, and volume:

$(V,Cr)P_4$

Volume CTE: $\alpha_V = 1.034(4) \times 10^{-5} + 3.64(2) \times 10^{-8} \times T$

a- axis CTE: $\alpha_a = 2.244(3) \times 10^{-6} + 1.180(13) \times 10^{-8} \times T$

b- axis CTE: $\alpha_b = 1.808(3) \times 10^{-6} + 1.776(14) \times 10^{-8} \times T$

c- axis CTE: $\alpha_c = 6.845(3) \times 10^{-6} + 7.944(12) \times 10^{-9} \times T$

β angle CTE: $\alpha_\beta = 6.3958(2) \times 10^{-7} + 2.18641(8) \times 10^{-9} \times T$

$(V,Cr,Mo)P_4$

Volume CTE: $\alpha_V = 2.006(7) \times 10^{-6} + 6.183(3) \times 10^{-8} \times T$

a- axis CTE: $\alpha_a = -4.32(6) \times 10^{-8} + 1.9747(3) \times 10^{-8} \times T$

b- axis CTE: $\alpha_b = 4.611(7) \times 10^{-7} + 1.9721(3) \times 10^{-8} \times T$

c- axis CTE: $\alpha_c = 2.0767(12) \times 10^{-6} + 2.3112(5) \times 10^{-8} \times T$

β angle CTE: $\alpha_\beta = 6.66045(8) \times 10^{-7} + 1.01769(3) \times 10^{-9} \times T$

VP_4

Volume CTE: $\alpha_V = 2.245(8) \times 10^{-6} + 6.693(3) \times 10^{-8} \times T$

a- axis CTE: $\alpha_a = 2.45(9) \times 10^{-8} + 2.3303(4) \times 10^{-8} \times T$

b- axis CTE: $\alpha_b = 3.636(6) \times 10^{-7} + 1.8775(3) \times 10^{-8} \times T$

c- axis CTE: $\alpha_c = 2.165(2) \times 10^{-6} + 2.9540(8) \times 10^{-8} \times T$

β angle CTE: $\alpha_\beta = 4.1614(8) \times 10^{-7} + 6.3626(3) \times 10^{-9} \times T$

CrP_4

Volume CTE: $\alpha_V = 7.55(2) \times 10^{-6} + 8.237(6) \times 10^{-8} \times T$

a- axis CTE: $\alpha_a = 1.2781(6) \times 10^{-6} + 1.729(3) \times 10^{-8} \times T$

b- axis CTE: $\alpha_b = 9.355(6) \times 10^{-7} + 1.7052(2) \times 10^{-8} \times T$

c- axis CTE: $\alpha_c = 7.376(7) \times 10^{-6} + 5.488(3) \times 10^{-8} \times T$

β angle CTE: $\alpha_\beta = 8.911(5) \times 10^{-7} + 1.6855(2) \times 10^{-8} \times T$

The temperature dependent CTE values between the phosphides are compared. In Figure 4-28, the CTE of the phosphides is plotted by volume and lattice parameter. Between the phosphides *a*- and *b*-axis have different trends/orders of CTE values. However, the volumetric CTE behavior of the phosphides shows the same trend as *c*-axis. Indicating that the volumetric CTE behavior is mainly described by the behavior of the *c*-axis. Although not exactly the same trend, the CTE of the β-angle has the order of $CrP_4 > VP_4 > (V,Cr)P_4 > (V,CrMo)P_4 > MoP_4$ from the largest to the smallest CTE value, which is almost the same as the order observed in the *c*-axis and the volume. From a crystal structure point of view shown in Figure 4-17, the change in *c*-axis is the change between each black phosphorus chain and the edge-shared octahedron. Thus, the β-angle has a direct relationship with the *c*-axis.

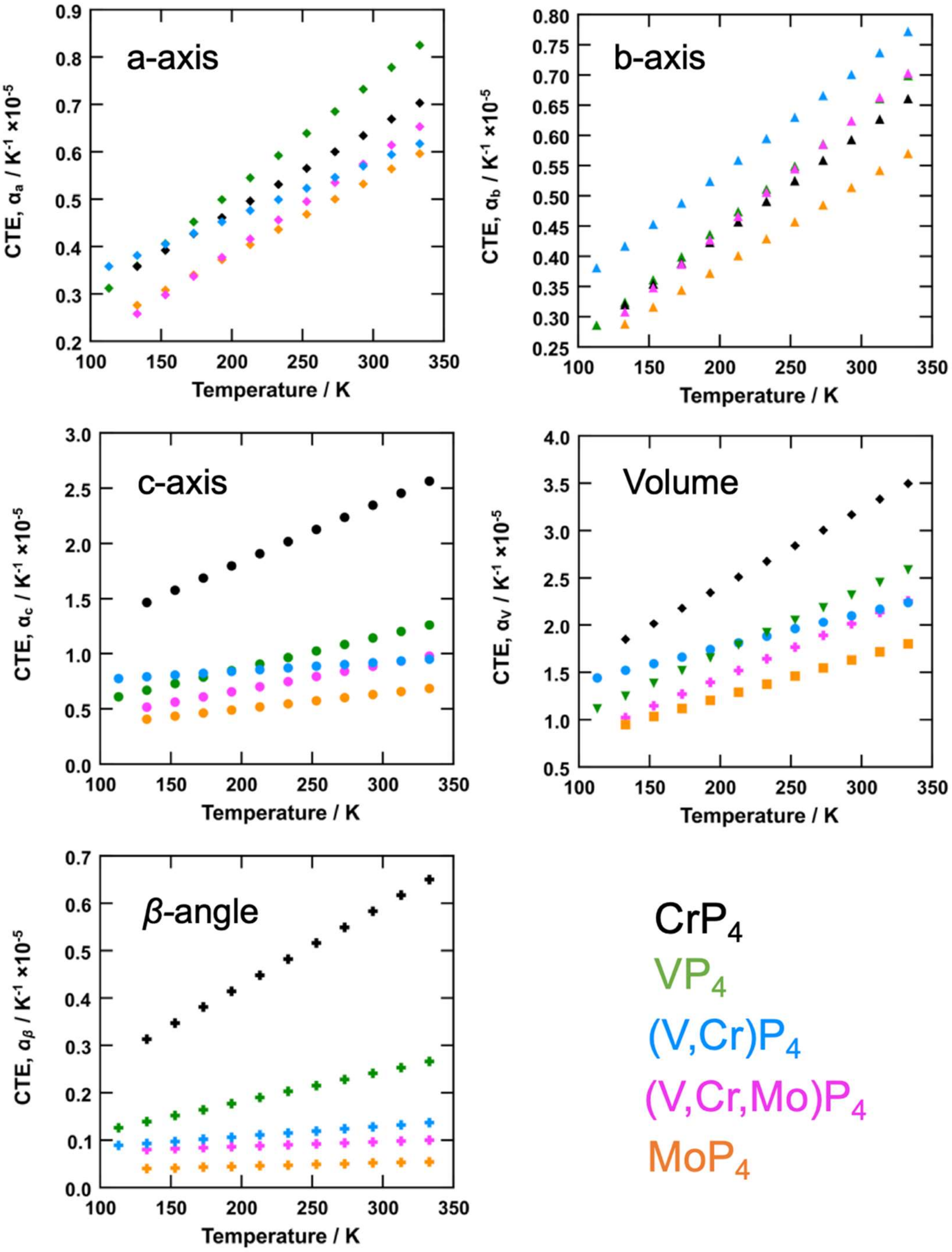

Figure 4-28 Temperature dependent CTE of the phosphides plotted by the volume and lattice parameters. The black, green, blue, pink, and orange markers represent CrP_4, VP_4, $(V,Cr)P_4$, $(V,Cr,Mo)P_4$ and MoP_4, respectively.

The volume metric CTE behavior is summarized in Figure 4-29. CrP_4 has the highest volumetric CTE values. $(V,Cr)P_4$ has lower CTE at high temperature and approaches the average value at low temperatures. The $(V,Cr)P_4$ has lower volumetric CTE than its binary counterparts (VP_4 and CrP_4) values at high temperatures (above 233K). $(V,Cr,Mo)P_4$ has lower than average CTE values throughout the experimental temperature range. This result shows that the thermal expansion behaviors of multicomponent phosphides are not the average of its endmember binary phosphides.

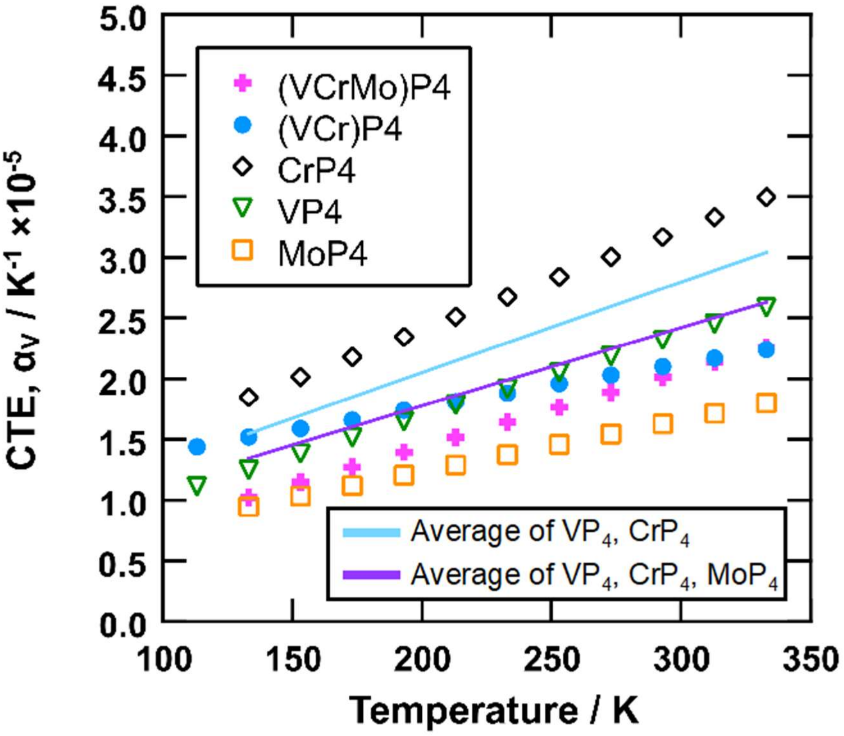

Figure 4-29 The temperature dependent volumetric CTE behavior of the phosphides. The blue and purple line represent the average values of the binary phosphides.

It is difficult to understand the reason for the observed multicomponent effect in the thermal expansion behavior of the multicomponent phosphides. However, the change in the crystal structure between the binary phosphides is further examined. In Figure 4-30 and Figure 4-31, it shows the temperature-dependent normalized change of bond lengths and bond angles, respectively. The insets in the upper left corner present the positions for each bond and angle.

The black phosphorus armchair chain (black phosphorus armchair direction) is the chain lies in the *a*-axis direction, $\theta 5$ and $\theta 6$ in Figure 4-31; *h*, *i*, and *j* in Figure 4-30 represent the bond angles and bond lengths of a black phosphorus armchair chain. Each chain is connected by a bond with bond length *k* at an angle $\theta 7$ as presented in the inset of the figures.

Starting from looking at the change in their angles. In Figure 4-30, for all the phosphides during cooling, $\theta 7$ that connects each black phosphorus armchair chain shrinks more than $\theta 5$ and $\theta 6$. The armchair direction ($\theta 5$ and $\theta 6$) has less deformation throughout the temperature range. This means that the thermal expansion behavior of the CrP_4-type phosphide is most dominant between each black phosphorus chain. The black phosphorus armchair chains approach each other when the temperature lowers.

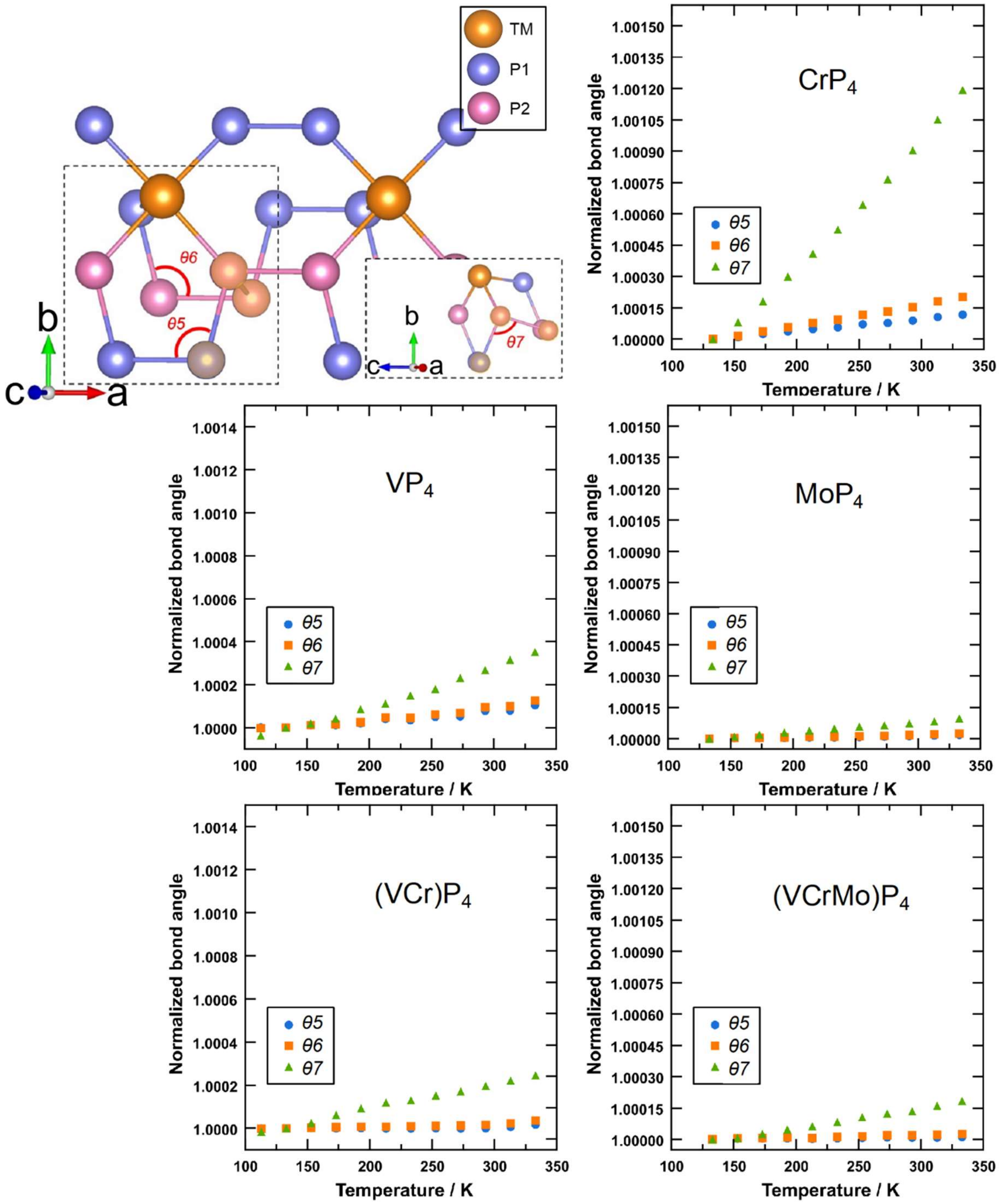

Figure 4-30 The temperature dependent normalized change in the angles in the black phosphorus layer of the phosphides. The data are normalized to 133 K. The transition metals (TM) are colored orange, and the phosphorus P1 and P2 are colored blue and pink, respectively.

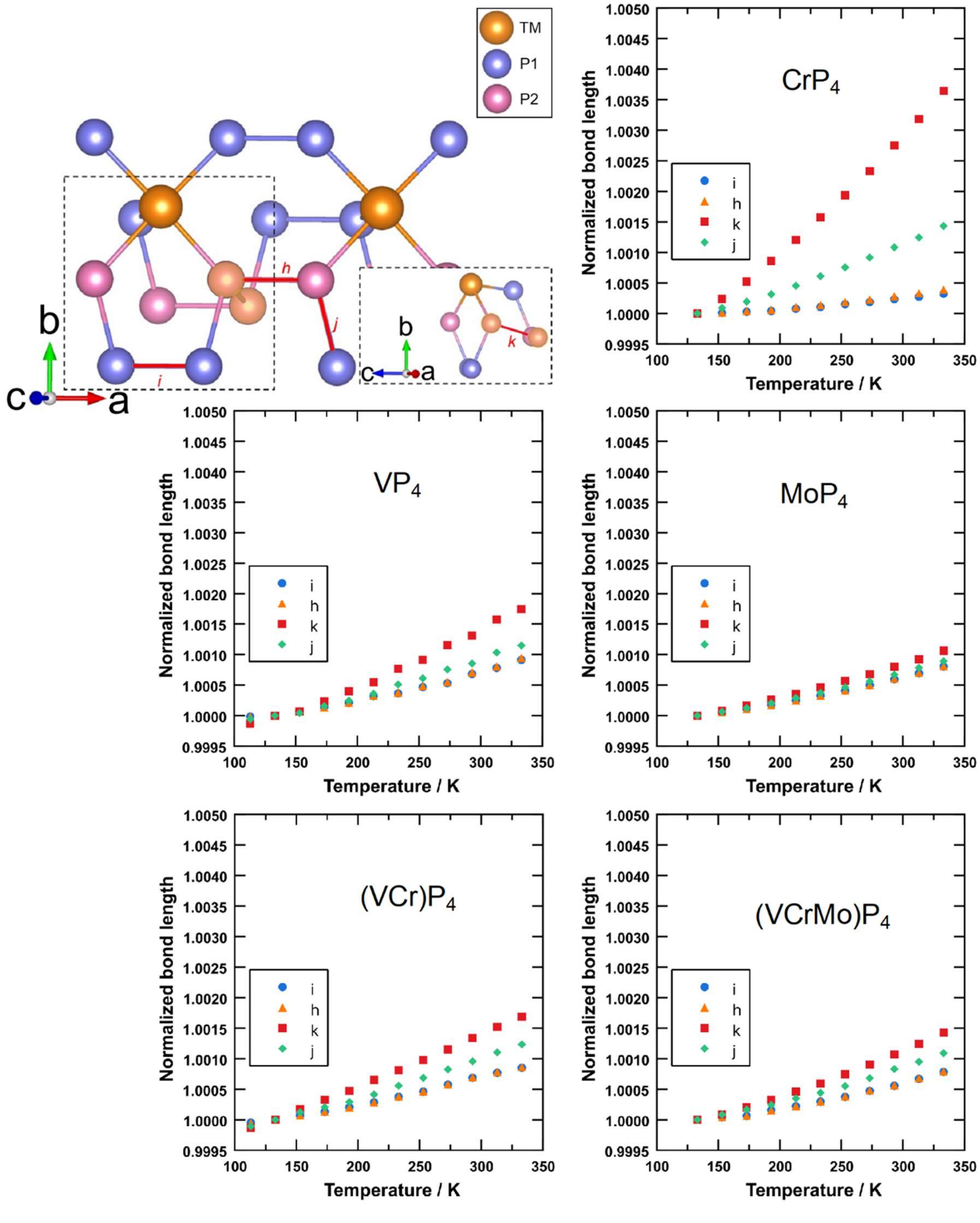

Figure 4-31 The temperature dependent normalized change in the bonding distance in the black phosphorus layer of the phosphides. The data are normalized to 133K. The transition metals (TM) are colored orange. The phosphorus P1 and P2 are colored blue and pink, respectively.

From the change in bond length. In Figure 4-31, the bond length *k*, which represents the bond connecting each armchair chain, shrinks more than *h*, *i*, and *j*. This again means that the black phosphorus armchair chain becomes closer together at low temperature. Since the $\theta 7$ (mentioned previously) and the bond *k* lie in the *c*-axis, this causes the large anisotropy behavior observed in the *c*-axis as will be discussed later.

Between the binary phosphides, CrP_4 is observed to have the most shrinkage in its length *k*. MoP_4 on the other hand shows almost no anisotropy change compared to other phosphides. This is expected from the structural discussion mentioned in Chapter 4.4, where the structure of MoP_4 is shown to be more distorted, thus having less space for the atom to move.

VP_4 compared to CrP_4 has a lower change in *k*, however, the bond length *i* and *h* in VP_4 change more than CrP_4. The *i* and *h* in MoP_4 also has more change than in CrP_4.

It is hard to conclude how the difference of *i* and *k* between the phosphide can affect the *a*-axis of the structure because the angles $\theta 5$, $\theta 6$ (Figure 4-30) and bond length *j* are also 'components' effecting the *a*-axis. But since $\theta 5$ and $\theta 6$ of VP_4 and MoP_4 only changed slightly and are lower than CrP_4, the thermal behavior 'components' can be summarized roughly.

From the bond length behavior in each binary phosphide, the amount of expansion in the *a*- and *c*-axis for VP_4 and CrP_4 is:

	a-axis	*c*-axis
VP_4	More than CrP_4	Less than CrP_4
CrP_4	Almost no change	Large change

Considering the pseudo-binary phosphide (V,Cr)P_4 having both the thermal expansion characteristics of VP_4 and CrP_4, the result is expected to show two competing expansion components, one in the *c*-axis and the other one in the *a*-axis.

In Figure 4-32, the normalized temperature dependent axis relationship of the phosphides is plotted by their lattice parameters. Recalling the black phosphorus layers are interconnected with the transition metal octahedron, the competing thermal expansion in *a*- and *c*-axis will further distort the octahedron. To accommodate the distortion, the thermal expansion in the *b*-axis is forced to be changed. This results in a larger thermal expansion found in the *b*-axis of (V,Cr)P_4 compared to its binary endmembers, and leads to the observed multicomponent effect in the CTE behaviors. This is also the same for the pseudo-ternary (V,Cr,Mo)P_4, but MoP_4 has a small thermal expansion behavior, thus the expansion in (V,Cr,Mo)P_4 is lower than (V,Cr)P_4.

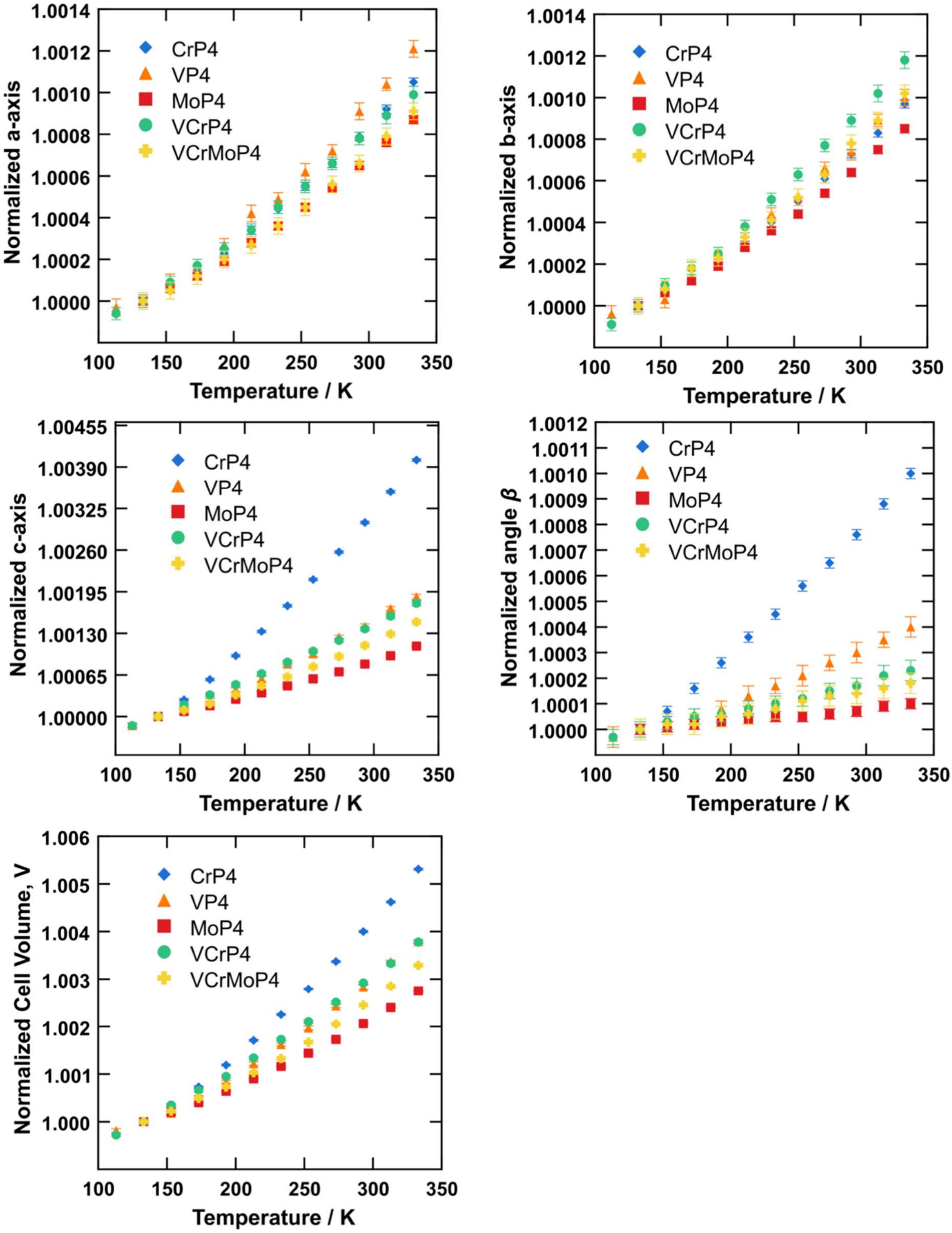

Figure 4-32 The normalized temperature dependent axis change plotted by their lattice parameters.

4.5.2 Compression behaviors

The *in-situ* compression and decompression XRD patterns for (V,Cr,Mo)P_4 and (V,Cr)P_4 are shown in Figure 4-33. The *in-situ* compression XRD pattern for the binary phosphides is shown in Figure 4-34. The compression experiment on the phosphides did not reveal any additional peaks, indicating no phase transition to denser phase within the measured pressure range. The pressure-dependent normalized lattice parameters and volume are shown in Figure 4-35. The bulk modulus was calculated from the measured pressure and volume data. The values are summarized in Table 4-18. VP_4 and CrP_4 have close bulk modulus. MoP_4 is the most incompressible among the phosphides. (V,Cr)P_4 has almost the same bulk modulus as its binary endmembers. With the inclusion of Mo, the bulk modulus of (V,Cr,Mo)P_4 becomes larger than (V,Cr)P_4. This is due to the larger bulk modulus of MoP_4. The average bulk modulus of (V,Cr,Mo)P_4 calculated from its binary endmember phosphides is K_0 = 120.0 GPa. Considering the experimental measurement error, this value is almost the same as the experiment result of K_0 = 122.1(7) GPa.

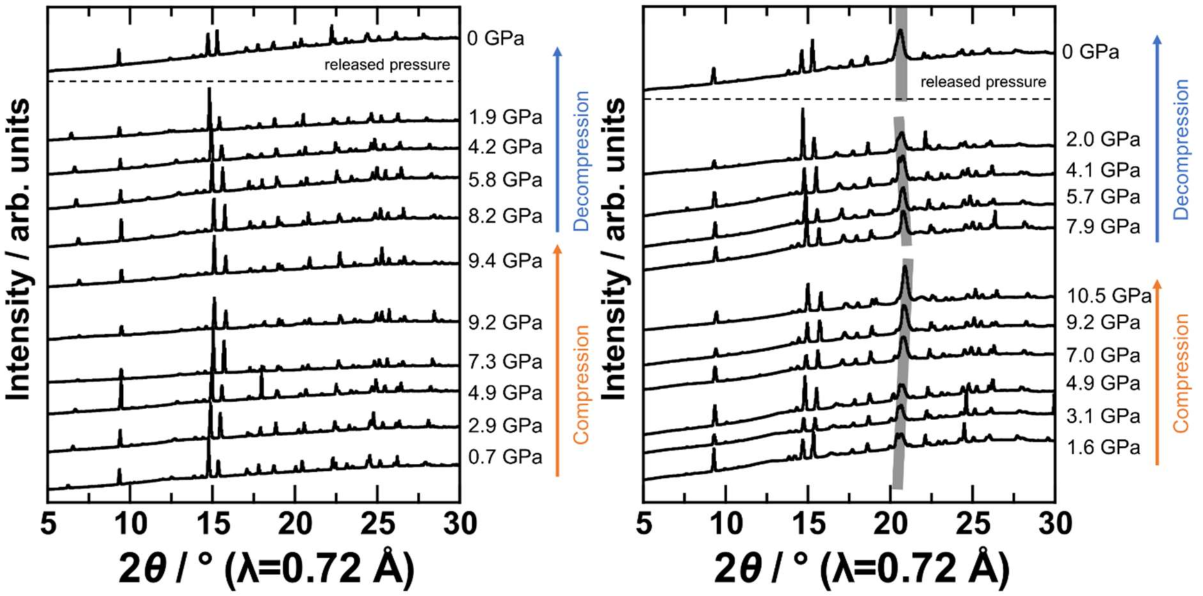

Figure 4-33 *In-situ* compression XRD pattern of (V,Cr)P_4 (left) and (V,Cr,Mo)P_4 (right) with P~ 2 GPa stepwise starting from P~ 1 GPa to maximum P~ 10 GPa and decompression down to ambient pressure. The grey-masked area is the peak of SUS gasket.

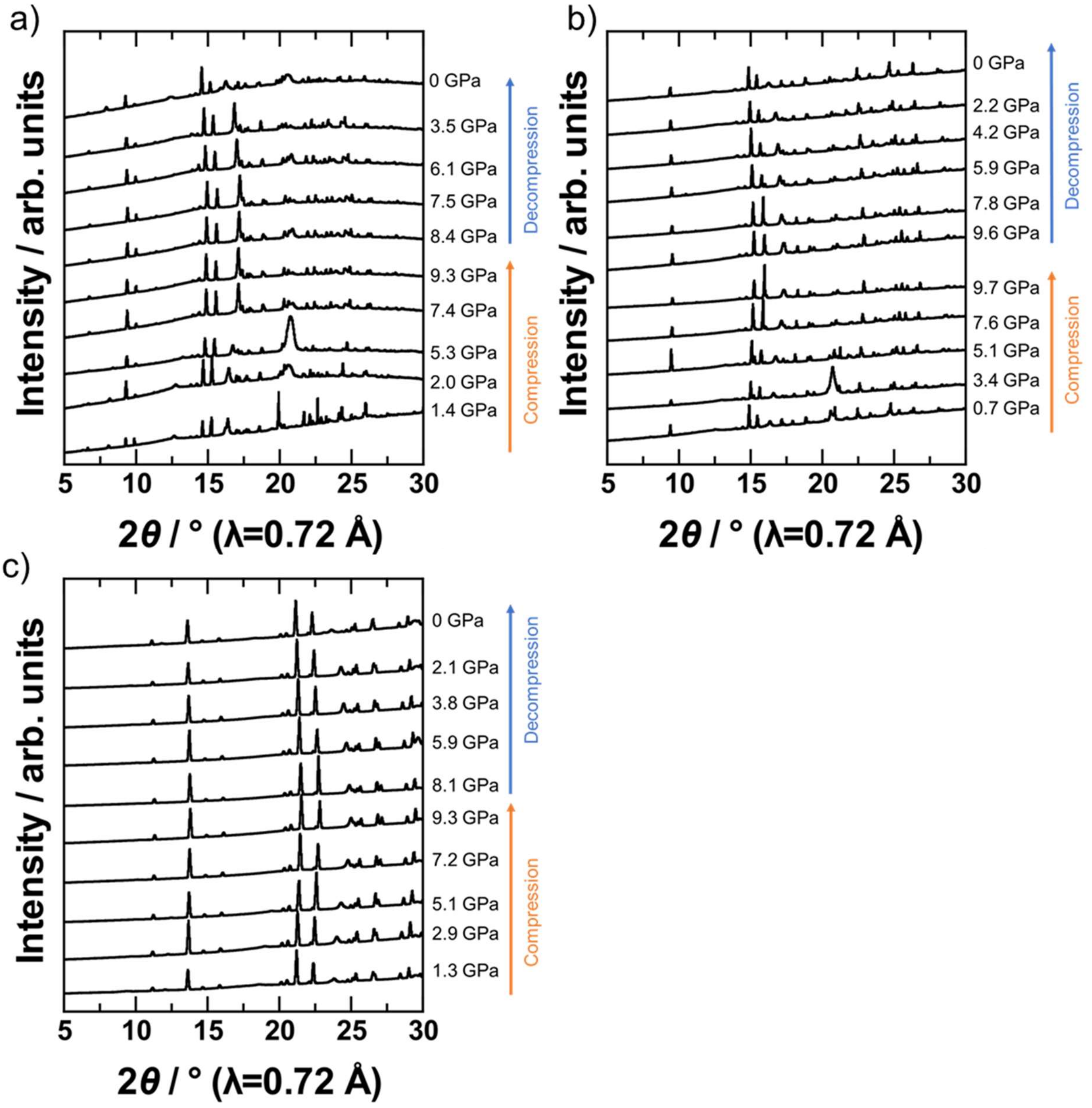

Figure 4-34 Synchrotron in-situ compression XRD pattern of a) VP_4, b) CrP_4, and c) MoP_4. The broad peaks observed around 20-23° in VP_4 and CrP_4 correspond to gasket.

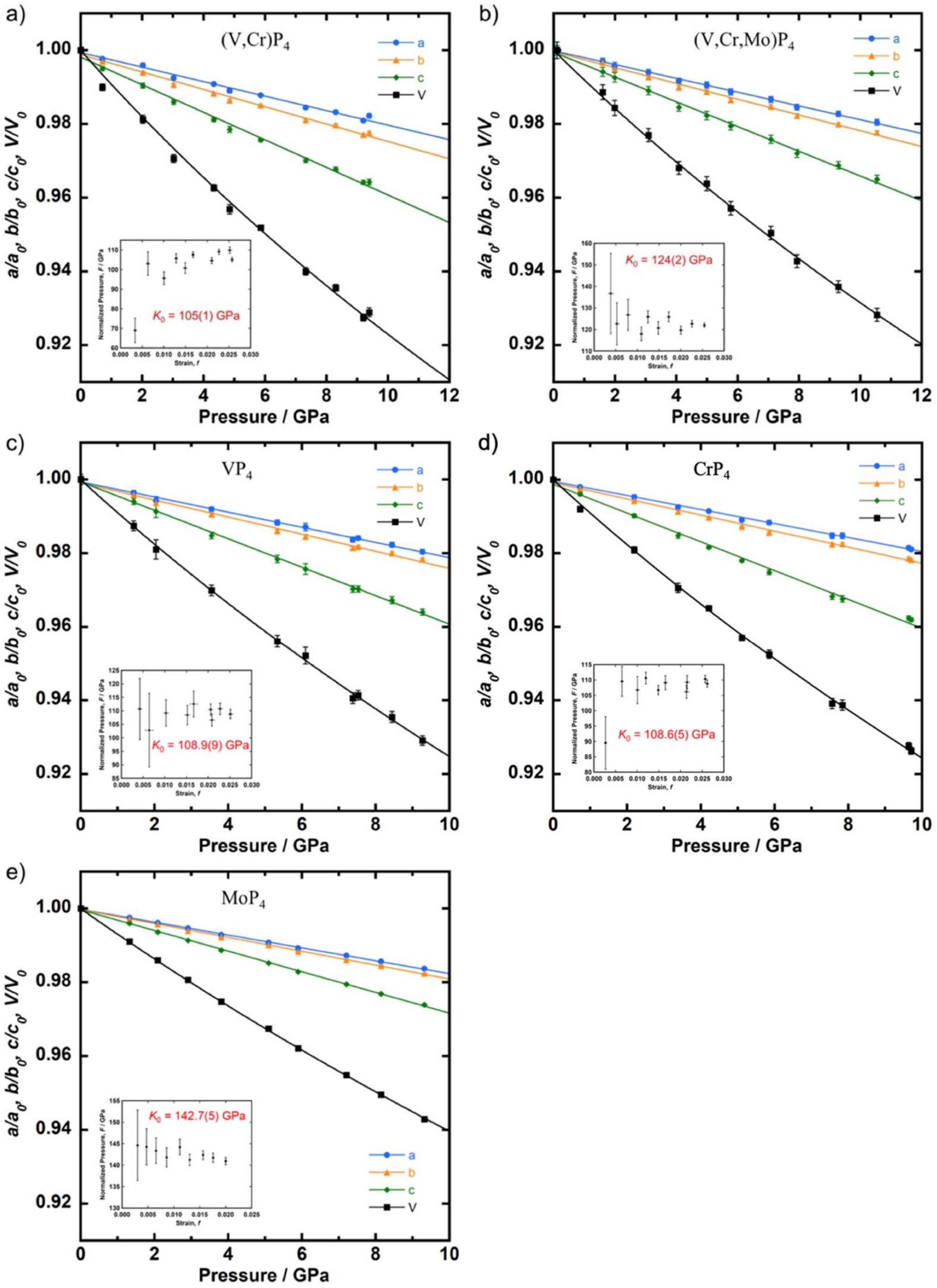

Figure 4-35 The compressibility and anisotropic behavior of a) (V,Cr)P$_4$, b) (V,Cr,Mo)P$_4$, c) VP$_4$, d) CrP$_4$, and e) MoP$_4$. The line on volume compression is fitted using second-order Birch-Murnaghan EOS. The lines on *a*-, *b*-, and *c*-axis are fitted using linear equation. The inset is the *F*-*f* plots for the corresponding phosphide compression results.

Table 4-18 Summarized zero-pressure bulk modulus and the slope of *a*-, *b*-, and *c*-axis.

		slope determined from fitting linear equation:		
	K_0 / GPa	*a*-axis / GPa^{-1}	*b*-axis / GPa^{-1}	*c*-axis / GPa^{-1}
VP_4	109.4(6)	486(11)	431(12)	259(4)
CrP_4	108.7(5)	524(10)	457(10)	256(6)
MoP_4	141.8(3)	572(6)	531(7)	357(3)
$(VCr)P_4$	106(1)	508(17)	425(13)	268(7)
$(VCrMo)P_4$	122.1(7)	535(9)	466(11)	298(6)

The axial anisotropic behaviors of both $(V,Cr,Mo)P_4$ and $(V,Cr)P_4$ show the same trend of axial compression behavior where the *c*-axis is more compressible than the *a*- and *b*-axis. The *a*- and *b*-axis have close compressibility, but *b*-axis is more compressible than the *a*-axis. In terms of the endmember binary phosphides, the *a*- and *b*- axis of CrP_4 are less compressible than VP_4, but the *c*-axis of CrP_4 is more compressible than VP_4. MoP_4 is the most incompressible and has smaller anisotropy. This gives $(V,Cr,Mo)P_4$ a higher bulk modulus than $(V,Cr)P_4$. All axes of $(V,Cr,Mo)P_4$ are less compressible than $(V,Cr)P_4$ (The slope determined from fitting linear equation are summarized in Table 4-18). This trend of the pressure-dependent axial anisotropy behavior of $(V,Cr,Mo)P_4$ and $(V,Cr)P_4$ is the same as that of their temperature-dependent axial anisotropy discussed in previous section (Chapter 4.5.1).

4.6 Conclusion

Adding elements into CrP_4, the result shows that $(V,Cr)P_4$, $(V,Cr,Mn)P_4$ and $(V,CrMo)P_4$ crystalized into the same CrP_4-type structure. Stating the feasibility of using high-pressure technique for the synthesis of multicomponent phosphides. Meanwhile, to synthesize homogeneous multicomponent phosphides, it is important to use pre-alloy starting metal sample for high pressure synthesis. Optimizing the pressure and temperature conditions for the multicomponent phosphide is also important. At present, the pseudo-quaternary and -quinary phosphide still need further investigation.

By examining the crystal structure of the binary phosphides, MoP_4 has highly distorted Mo octahedra. This structural singularity in MoP_4 gives the abnormal lattice parameter that cannot be explained by the atomic size relationship for MoP_4. However, the lattice parameter of the multicomponent phosphides $(V,Cr)P_4$ and $(V,Cr,Mo)P_4$ is the average of its endmember phosphides.

The volumetric thermal expansion behavior of the CrP_4-type structure is primarily attributed to the thermal expansion along the *c*-axis. At high temperatures, the CTE value of $(V,Cr)P_4$ is lower than VP_4 and CrP_4. $(V,Cr,Mo)P_4$ has lower CTE than $(V,Cr)P_4$ because the MoP_4 has the lowest coefficient of thermal expansion among endmember binary phosphides. $(V,Cr,Mo)P_4$ also has lower than average CTE values throughout the experiment temperature range. These results present that the multicomponent phosphides have multicomponent effect in their thermal expansion behavior. The thermal expansion behaviors of the phosphides are understood through examine the behavior of the characteristic black phosphorus layer. The expansion of VP_4 in its *a*-axis and the expansion of CrP_4 in its *c*-axis present to be affecting the observed abnormal behaviors of the multicomponent phosphides.

Regarding compression behavior, the *c*-axis is found to be more compressible than the *a*- and *b*-axis in the CrP_4-type structure, consistent with their thermal expansion behaviors. MoP_4 exhibits the highest bulk modulus, making $(V,Cr,Mo)P_4$ more incompressible than $(V,Cr)P_4$. The bulk modulus of the multicomponent phosphide is the average of their endmember, indicating no significant multicomponent effect in the compression behavior of multicomponent phosphide.

Chapter 5 Summary

The main objective of this thesis is to synthesize equimolar multicomponent nitride and phosphides using high-pressure technique and establish their synthesis conditions. The evaluation of the synthesized multicomponent ceramics is conducted using synchrotron X-ray technique. The study also investigated the multicomponent effect in terms of lattice parameters, coefficient of thermal expansion, and bulk modulus. This research aims to contribute to the understanding of the synthesis and properties of equimolar multicomponent compounds, providing insights into their structural behaviors under temperature and pressure conditions.

5.1 Multicomponent oxide and nitride

In the high-pressure synthesis of multicomponent nitrides using an alloy starting sample and NH_4Cl, the resulting composition showed low V and Cr content. This discrepancy was attributed to the formation of particularly stable chloride compounds, that influenced the synthesis of multicomponent nitride. Despite attempts to introduce excess amount of V and Cr, the final product exhibited low Cr composition. However, the synthesis did yield fine cubic crystals. The multicomponent nitride, close to a pseudo-ternary composition and adopting a NaCl-type structure, was examined. Its lattice parameter and bulk modulus were found to be the average of the constituent endmembers Nevertheless, to understand how different elements can impact the thermal behavior of the multicomponent nitride, further investigating of all endmembers binary nitrides is necessary.

5.2 Multicomponent phosphide

In the synthesis of (V,Cr)P_4, (V,Cr,Mo)P_4 using an alloy starting material, longer heating time for (V,Cr,Mo)P_4 resulted in alloy precipitation, indicating the instability of multicomponent phosphide under high-temperature conditions. The multicomponent phosphides adopted the same CrP_4-type crystal structure. Comparing the lattice parameters of the binary endmember phosphides, MoP_4 exhibited large distortion in its transition metal octahedron. This characteristic of MoP_4 may also attribute to the observed lower thermal expansion and higher bulk modulus for MoP_4. When examine the lattice parameter of the multicomponent phosphides, they can be explained by the average of their endmembers.

The thermal expansion behaviors of CrP_4-type structure have larger CTE values in *c*-axis than *a*- and *b*-axis. (V,Cr)P_4 exhibited lower thermal expansion at high temperature, lower than VP_4 and CrP_4. The CTE values for (V,Cr,Mo)P_4 were consistently lower than the average throughout the experimental temperature range.

Regarding compressibility, MoP_4 showed the highest bulk modulus, resulting in a larger bulk modulus for (V,Cr,Mo)P_4 than (V,Cr)P_4. The axial anisotropic behaviors of both pseudo-ternary (V,Cr,Mo)P_4 and pseudo-binary (V,Cr)P_4 show the same trend of compression behavior where the *c*-axis is more compressible than *a*- and *b*-axis. The *a*- and *b*-axis have close compressibility, while the *b*-axis is more compressible than the *a*-axis. This compression behavior was the same as the binary phosphides, which indicates the common anisotropic compression behavior of the CrP_4-type structure.

5.3 High-pressure synthesis of multicomponent ceramics and the multicomponent effects

The synthesis conditions for multicomponent nitride and phosphide under high pressure have been successfully established in this study. The high-pressure technique proves to be a power tool in synthesizing multicomponent ceramics. Regardless of the synthesis difficulties in nitride and phosphide material at ambient pressure, multicomponent nitride and phosphides are successfully synthesized using a large volume press. High-pressure technique is also capable of synthesizing different multicomponent ceramics with different crystal structures, from simple cubic structure to complicated monoclinic structure. Nevertheless, it should be noted that an alloy starting material is required for the synthesis. When starting materials such as chlorides are used, the affinity between metal element and chlorine should be considered. Finally, the optimization of the pressure and temperature condition is important.

The evaluation using synchrotron XRD is a useful and powerful method for characterizing high-pressure synthesized multicomponent ceramics. The results of the multicomponent effect on lattice parameter, thermal stability and expansion, and compression behaviors, are summarized in Table 5-1. Although information on endmember binary nitrides is lacking for multicomponent nitride, multicomponent oxide and phosphides exhibit a multicomponent effect in their thermal expansion behavior.

While the underlaying reasons for the observed thermal expansion behavior are challenging to elucidate, it is suggested that the thermal expansion behavior may be different between multicomponent oxide and phosphide. There is a possibility that the high thermal expansion in multicomponent oxide is the result from the Jahn-Teller effect due to CoO. For the multicomponent phosphide, the difference in the thermal expansion behaviors found in VP_4 and CrP_4 might have caused the $(V,Cr)P_4$ to behave differently than the average. With the addition of Mo, the CTE values are effectively suppressed and $(V,Cr,Mo)P_4$ has lower CTE than the average. To draw more conclusive insights into multicomponent effects in multicomponent ceramics, additional investigations will be necessary.

Table 5-1 Summary on the multicomponent effect in lattice parameter, thermal expansion, and compression behaviors between the multicomponent oxide, nitride, and phosphide.

	Lattice parameter	Thermal expansion	compression
oxide	No(?)	Yes	No
nitride	No	-	No(?)
phosphide	No	Yes	No

Chapter 6 References

[1] T.P. Pearsall, R.W. Hopson, Growth and characterization of lattice-matched epitaxial films of Ga x In1− x As/InP by liquid-phase epitaxy, J Appl Phys 48 (1977) 4407–4409. https://doi.org/10.1063/1.323399.

[2] S.-W. Cheong, J.D. Thompson, Z. Fisk, Properties of La2CuO4 and related compounds, Physica C Supercond 158 (1989) 109–126. https://doi.org/10.1016/0921-4534(89)90306-7.

[3] B. Cantor, I.T.H. Chang, P. Knight, A.J.B. Vincent, Microstructural development in equiatomic multicomponent alloys, Materials Science and Engineering A 375–377 (2004) 213–218. https://doi.org/10.1016/j.msea.2003.10.257.

[4] J.-W. Yeh, S.-K. Chen, S.-J. Lin, J.-Y. Gan, T.-S. Chin, T.-T. Shun, C.-H. Tsau, S.-Y. Chang, Nanostructured High-Entropy Alloys with Multiple Principal Elements: Novel Alloy Design Concepts and Outcomes, Adv Eng Mater 6 (2004) 299–303. https://doi.org/10.1002/adem.200300567.

[5] C.M. Rost, E. Sachet, T. Borman, A. Moballegh, E.C. Dickey, D. Hou, J.L. Jones, S. Curtarolo, J.-P. Maria, Entropy-stabilized oxides, Nat Commun 6 (2015) 8485. https://doi.org/10.1038/ncomms9485.

[6] G.J. Piermarini, S. Block, J.D. Barnett, Hydrostatic limits in liquids and solids to 100 kbar, J Appl Phys 44 (1973) 5377–5382. https://doi.org/10.1063/1.1662159.

[7] H.K. Mao, J. Xu, P.M. Bell, Calibration of the ruby pressure gauge to 800 kbar under

quasi-hydrostatic conditions, J Geophys Res 91 (1986) 4673. https://doi.org/10.1029/jb091ib05p04673.

[8] A. P. Hammersley, FIT2D V9.129 Reference Manual V3.1, ESRF Internal Report ESRF98HA01T (1998).

[9] A. P. Hammersley, S. O. Svensson, M. Hanfland, A. N. Fitch, D. Häusermann, Two-Dimensional Detector Software: From Real Detector to Idealised Image or Two-Theta Scan, High Press Res 14 (1996) 235–248.

[10] N. Watanabe, T. Nagae, Y. Yamada, A. Tomita, N. Matsugaki, M. Tabuchi, Protein crystallography beamline BL2S1 at the Aichi synchrotron, J Synchrotron Radiat 24 (2017) 338–343. https://doi.org/10.1107/S1600577516018579.

[11] Y. Seto, D. Nishio-Hamane, T. Nagai, N. Sata, Development of a software suite on X-ray diffraction experiments, Review of High Pressure Science and Technology/Koatsuryoku No Kagaku To Gijutsu 20 (2010) 269–276. https://doi.org/10.4131/jshpreview.20.269.

[12] F. Izumi, K. Momma, Three-dimensional visualization in powder diffraction, Solid State Phenomena 130 (2007) 15–20. https://doi.org/10.4028/www.scientific.net/SSP.130.15.

[13] K. Momma, F. Izumi, VESTA 3 for three-dimensional visualization of crystal, volumetric and morphology data, J Appl Crystallogr 44 (2011) 1272–1276. https://doi.org/10.1107/S0021889811038970.

[14] E. Kulik, V. Murzin, S. Kawaguchi, N. Nishiyama, T. Katsura, Thermal expansion of

coesite determined by synchrotron powder X-ray diffraction, Phys Chem Miner 45 (2018) 873–881. https://doi.org/10.1007/s00269-018-0969-7.

[15] N.A. Gaida, K. Niwa, T. Sasaki, M. Hasegawa, Phase relations and thermoelasticity of magnesium silicide at high pressure and temperature, J Chem Phys 154 (2021) 144701. https://doi.org/10.1063/5.0044648.

[16] Derek Taylor, Thermal Expansion Data: I. Binary Oxides with the Sodium Chloride and Wurtzite Structures, MO, British Ceramic Transactions and Journal 83 (1984) 5–9.

[17] J. Tan, S. Zhang, S. Wang, W. Wang, X. Zheng, J. Zhao, W. Li, X. Mao, K. Liu, X. Zhou, Y. Zhao, C. Jin, X. Yu, Stoichiometric δ-NbN: The Most Incompressible Cubic Transition Metal Mononitride, Phys Status Solidi B Basic Res 254 (2017). https://doi.org/10.1002/pssb.201700063.

[18] D. Dzivenko, A. Zerr, N. Guignot, M. Mezouar, R. Riedel, Compressibility of cubic vanadium mononitride, EPL (Europhysics Letters) 92 (2010) 66001. https://doi.org/10.1209/0295-5075/92/66001.

[19] I. Milošev, H.H. Strehblow, B. Navinšek, Comparison of TiN, ZrN and CrN hard nitride coatings: Electrochemical and thermal oxidation, Thin Solid Films 303 (1997) 246–254. https://doi.org/10.1016/S0040-6090(97)00069-2.

[20] A. Zakutayev, Design of nitride semiconductors for solar energy conversion, J Mater Chem A Mater 4 (2016) 6742–6754. https://doi.org/10.1039/c5ta09446a.

[21] K. Inumaru, T. Nishikawa, K. Nakamura, S. Yamanaka, High-Pressure Synthesis of

Superconducting Molybdenum Nitride δ-MoN by in Situ Nitridation, Chemistry of Materials 20 (2008) 4756–4761. https://doi.org/10.1021/cm800820d.

[22] B.C. Frazer, Magnetic Structure of <math display="inline"> <mrow> <msub> <mrow> <mi mathvariant="normal">Fe</mi> </mrow> <mrow> <mn>4</mn> </mrow> </msub> </mrow> </math> N, Physical Review 112 (1958) 751–754. https://doi.org/10.1103/PhysRev.112.751.

[23] A.D. Pogrebnjak, I.V. Yakushchenko, A.A. Bagdasaryan, O.V. Bondar, R. Krause-Rehberg, G. Abadias, P. Chartier, K. Oyoshi, Y. Takeda, V.M. Beresnev, O.V. Sobol, Microstructure, physical and chemical properties of nanostructured (Ti–Hf–Zr–V–Nb)N coatings under different deposition conditions, Mater Chem Phys 147 (2014) 1079–1091. https://doi.org/10.1016/j.matchemphys.2014.06.062.

[24] S.-C. Liang, D.-C. Tsai, Z.-C. Chang, H.-S. Sung, Y.-C. Lin, Y.-J. Yeh, M.-J. Deng, F.-S. Shieu, Structural and mechanical properties of multi-element (TiVCrZrHf)N coatings by reactive magnetron sputtering, Appl Surf Sci 258 (2011) 399–403. https://doi.org/10.1016/j.apsusc.2011.09.006.

[25] K.-H. Cheng, C.-H. Lai, S.-J. Lin, J.-W. Yeh, Structural and mechanical properties of multi-element (AlCrMoTaTiZr)Nx coatings by reactive magnetron sputtering, Thin Solid Films 519 (2011) 3185–3190. https://doi.org/10.1016/j.tsf.2010.11.034.

[26] D. Moskovskikh, S. Vorotilo, V. Buinevich, A. Sedegov, K. Kuskov, A. Khort, C. Shuck, M. Zhukovskyi, A. Mukasyan, Extremely hard and tough high entropy nitride ceramics,

Sci Rep 10 (2020) 19874. https://doi.org/10.1038/s41598-020-76945-y.

[27] A. Zerr, G. Miehe, J. Li, D.A. Dzivenko, V.K. Bulatov, H. Höfer, N. Bolfan-Casanova, M. Fialin, G. Brey, T. Watanabe, M. Yoshimura, High-Pressure Synthesis of Tantalum Nitride Having Orthorhombic U_2S_3 Structure, Adv Funct Mater 19 (2009) 2282–2288. https://doi.org/10.1002/adfm.200801923.

[28] F. Kawamura, H. Yusa, T. Taniguchi, Synthesis of rhenium nitride crystals with MoS<sub>2</s structure, Appl Phys Lett 100 (2012) 2–5. https://doi.org/10.1063/1.4729586.

[29] S. Wang, X. Yu, Z. Lin, R. Zhang, D. He, J. Qin, J. Zhu, J. Han, L. Wang, H.K. Mao, J. Zhang, Y. Zhao, Synthesis, crystal structure, and elastic properties of novel tungsten nitrides, Chemistry of Materials 24 (2012) 3023–3028. https://doi.org/10.1021/cm301516w.

[30] S.D. Kloß, S. Wandelt, A. Weis, W. Schnick, Accessing Tetravalent Transition-Metal Nitridophosphates through High-Pressure Metathesis, Angewandte Chemie 130 (2018) 3246–3249. https://doi.org/10.1002/ange.201712006.

[31] N.A. Gaida, T. Sasaki, Z. Liu, K. Niwa, M. Hirozawa, T. Ohsuna, M. Hasegawa, Nanowire crystals of tantalum nitride grown in ammonium halide fluxes at high pressures, Appl Phys Lett 116 (2020) 2–7. https://doi.org/10.1063/1.5140856.

[32] T. Sasaki, T. Ikoma, K. Sago, Z. Liu, K. Niwa, T. Ohsuna, M. Hasegawa, High-Pressure Synthesis and Crystal Structure of MoC-Type Tungsten Nitride by Nitridation with

Ammonium Chloride, Inorg Chem 58 (2019) 16379–16386. https://doi.org/10.1021/acs.inorgchem.9b01945.

[33] B. Cheng, H. Lou, A. Sarkar, Z. Zeng, F. Zhang, X. Chen, L. Tan, K. Glazyrin, H.-P. liermann, J. Yan, L. Wang, R. Djenadic, H. Hahn, Q. Zeng, Lattice distortion and stability of (Co0.2Cu0.2Mg0.2Ni0.2Zn0.2)O high-entropy oxide under high pressure, Mater Today Adv 8 (2020) 100102. https://doi.org/10.1016/j.mtadv.2020.100102.

[34] A. Sarkar, R. Djenadic, N.J. Usharani, K.P. Sanghvi, V.S.K. Chakravadhanula, A.S. Gandhi, H. Hahn, S.S. Bhattacharya, Nanocrystalline multicomponent entropy stabilised transition metal oxides, J Eur Ceram Soc 37 (2017) 747–754. https://doi.org/10.1016/j.jeurceramsoc.2016.09.018.

[35] J. Chen, W. Liu, J. Liu, X. Zhang, M. Yuan, Y. Zhao, J. Yan, M. Hou, J. Yan, M. Kunz, N. Tamura, H. Zhang, Z. Yin, Stability and Compressibility of Cation-Doped High-Entropy Oxide MgCoNiCuZnO $_5$, The Journal of Physical Chemistry C 123 (2019) 17735–17744. https://doi.org/10.1021/acs.jpcc.9b04992.

[36] P. Karen, A. Kjekshus, Q. Huang, V.L. Karen, The crystal structure of magnesium dicarbide, J Alloys Compd 282 (1999) 72–75. https://doi.org/10.1016/S0925-8388(98)00828-7.

[37] T. Pan, G.W.D. Spratt, L. Tang, D.E. Laughlin, Magnetic properties and microstructure of evaporated Co oxide tape media, J Magn Magn Mater 155 (1996) 309–311. https://doi.org/10.1016/0304-8853(95)00749-0.

[38] Z. Feng, V.S. Babu, J. Zhao, M.S. Seehra, Effect of magnetic dilution on magnetic ordering in Ni *p* Mg1− *p* O, J Appl Phys 70 (1991) 6161–6163. https://doi.org/10.1063/1.350030.

[39] H.M. Shao, K. Zhou, Y. Rui, J.C. Shen, X.N. Xu, H.L. Ji, X.X. Yao, L.J. Shen, Z. Wu, Z.J. Li, G.N. Zhang, G.C. Che, Z.X. Zhao, Synthesis and X-ray powder diffraction analysis of the high-Tc superconductor HgBa2Ca2Cu3O8+δ, Solid State Commun 92 (1994) 595–599. https://doi.org/10.1016/0038-1098(94)00516-8.

[40] O. GARCIAMARTINEZ, R. ROJAS, E. VILA, J. DEVIDALES, Microstructural characterization of nanocrystals of ZnO and CuO obtained from basic salts, Solid State Ion 63–65 (1993) 442–449. https://doi.org/10.1016/0167-2738(93)90142-P.

[41] M.D. Rechtin, B.L. Averbach, Tetragonal Elongation in CoO Near the Néel Point, Phys Rev Lett 26 (1971) 1483–1485. https://doi.org/10.1103/PhysRevLett.26.1483.

[42] S. Greenwald, The antiferromagnetic structure deformations in CoO and MnTe, Acta Crystallogr 6 (1953) 396–398. https://doi.org/10.1107/s0365110x53001101.

[43] K. Tomiyasu, T. Inami, N. Ikeda, Magnetic structure of CoO studied by neutron and synchrotron x-ray diffraction, Phys Rev B 70 (2004) 184411. https://doi.org/10.1103/PhysRevB.70.184411.

[44] D. Berardan, A.K. Meena, S. Franger, C. Herrero, N. Dragoe, Controlled Jahn-Teller distortion in (MgCoNiCuZn)O-based high entropy oxides, J Alloys Compd 704 (2017) 693–700. https://doi.org/10.1016/j.jallcom.2017.02.070.

[45] Z. Rák, J.P. Maria, D.W. Brenner, Evidence for Jahn-Teller compression in the (Mg Co Ni Cu Zn)O entropy-stabilized oxide: A DFT study, Mater Lett 217 (2018) 300–303. https://doi.org/10.1016/j.matlet.2018.01.111.

[46] R. Gupta, M. Gupta, Bulk modulus of second-order pressure derivative for nanomaterials, Bulletin of Materials Science 44 (2021) 218. https://doi.org/10.1007/s12034-021-02503-5.

[47] D.C. Gupta, P. Rana, Study of semiconducting nanomaterials under pressure, J Mol Model 18 (2012) 3341–3350. https://doi.org/10.1007/s00894-011-1347-2.

[48] W. Jifang, E.S. Fisher, M.H. Manghnzmi, Elastic Constants of Nickel Oxide, Chinese Physics Letters 8 (1991) 153–156. https://doi.org/10.1088/0256-307X/8/3/012.

[49] H. Karzel, W. Potzel, M. Köfferlein, W. Schiessl, M. Steiner, U. Hiller, G.M. Kalvius, D.W. Mitchell, T.P. Das, P. Blaha, K. Schwarz, M.P. Pasternak, Lattice dynamics and hyperfine interactions in ZnO and ZnSe at high external pressures, Phys Rev B 53 (1996) 11425–11438. https://doi.org/10.1103/PhysRevB.53.11425.

[50] K. Becker, F. Ebert, Die Kristallstruktur einiger binärer Carbide und Nitride, Zeitschrift Für Physik 31 (1925) 268–272. https://doi.org/10.1007/BF02980580.

[51] X. Feng, K. Bao, Q. Tao, L. Li, Z. Shao, H. Yu, C. Xu, S. Ma, M. Lian, X. Zhao, Y. Ge, D. Li, D. Duan, P. Zhu, T. Cui, Role of TM–TM Connection Induced by Opposite d-Electron States on the Hardness of Transition-Metal (TM = Cr, W) Mononitrides, Inorg Chem 58 (2019) 15573–15579. https://doi.org/10.1021/acs.inorgchem.9b02634.

[52] A. V. Linde, R.-M. Marin-Ayral, F. Bosc-Rouessac, V. V. Grachev, Effect of nitrogen to niobium atomic ratio on superconducting transition temperature of δ-NbN x powders, International Journal of Self-Propagating High-Temperature Synthesis 19 (2010) 9–16. https://doi.org/10.3103/s1061386210010024.

[53] G. Linker, R. Smithey, O. Meyer, Superconductivity in MoN films with NaCl structure, Journal of Physics F: Metal Physics 14 (1984) L115–L119. https://doi.org/10.1088/0305-4608/14/7/005.

[54] H. Yusa, F. Kawamura, T. Taniguchi, N. Hirao, Y. Ohishi, T. Kikegawa, High-pressure synthesis and compressive behavior of tantalum nitrides, J Appl Phys 115 (2014). https://doi.org/10.1063/1.4867986.

[55] F. Rivadulla, M. Bãobre-López, C.X. Quintela, A. Pĩeiro, V. Pardo, D. Baldomir, M.A. López-Quintela, J. Rivas, C.A. Ramos, H. Salva, J.S. Zhou, J.B. Goodenough, Reduction of the bulk modulus at high pressureinCrN, Nat Mater 8 (2009) 947–951. https://doi.org/10.1038/nmat2549.

[56] S. Wang, X. Yu, J. Zhang, M. Chen, J. Zhu, L. Wang, D. He, Z. Lin, R. Zhang, K. Leinenweber, Y. Zhao, Experimental invalidation of phase-transition-induced elastic softening in CrN, Phys Rev B Condens Matter Mater Phys 86 (2012). https://doi.org/10.1103/PhysRevB.86.064111.

[57] S. Wang, D. Antonio, X. Yu, J. Zhang, A.L. Cornelius, D. He, Y. Zhao, The Hardest Superconducting Metal Nitride, Sci Rep 5 (2015). https://doi.org/10.1038/srep13733.

[58] M. Sun, H. Liu, J. Qu, J. Li, Earth-Rich Transition Metal Phosphide for Energy Conversion and Storage, Adv Energy Mater 6 (2016). https://doi.org/10.1002/aenm.201600087.

[59] M. Sharon, G. Tamizhmani, Transition metal phosphide semiconductors for their possible use in photoelectrochemical cells and solar chargeable battery (Saur Viddyut Kosh V), J Mater Sci 21 (1986) 2193–2201. https://doi.org/10.1007/BF00547969.

[60] Y. Zhang, L. Yan, W. Wu, G. He, J. Zhang, Z. Ni, X. Jiang, M. Qin, F. Jin, J. Yuan, B. Zhu, Q. Chen, L. Zhou, Y. Li, J. Luo, K. Jin, Single-crystalline transition metal phosphide superconductor WP studied by Raman spectroscopy and first-principles calculations, Phys Rev B 105 (2022) 174511. https://doi.org/10.1103/PhysRevB.105.174511.

[61] O. Tegus, E. Brück, K.H.J. Buschow, F.R. de Boer, Transition-metal-based magnetic refrigerants for room-temperature applications, Nature 415 (2002) 150–152. https://doi.org/10.1038/415150a.

[62] Y. Andersson, H. Sørensen, A. Kjekshus, E. Näsäkkälä, The Crystal Structure of Pd15P2., Acta Chem Scand 31a (1977) 354–358. https://doi.org/10.3891/acta.chem.scand.31a-0354.

[63] S. Lange, M. Bawohl, R. Weihrich, T. Nilges, Mineralization Routes to Polyphosphides: Cu_2P_{20} and Cu_5InP_{16}, Angewandte Chemie International Edition 47 (2008) 5654–5657. https://doi.org/10.1002/anie.200705540.

[64] S.L. Brock, K. Senevirathne, Recent developments in synthetic approaches to transition metal phosphide nanoparticles for magnetic and catalytic applications, J Solid State Chem 181 (2008) 1552–1559. https://doi.org/10.1016/j.jssc.2008.03.012.

[65] E. Muthuswamy, P.R. Kharel, G. Lawes, S.L. Brock, Control of Phase in Phosphide Nanoparticles Produced by Metal Nanoparticle Transformation: Fe_2P and FeP, ACS Nano 3 (2009) 2383–2393. https://doi.org/10.1021/nn900574r.

[66] P.E.R. Blanchard, A.P. Grosvenor, R.G. Cavell, A. Mar, X-ray Photoelectron and Absorption Spectroscopy of Metal-Rich Phosphides M_2P and M_3P (M = Cr−Ni), Chemistry of Materials 20 (2008) 7081–7088. https://doi.org/10.1021/cm802123a.

[67] H. Barz, H.C. Kut, G.P. Meisnert, Z. Fiskt, B.T. Matthias, Ternary transition metal phosphides: High-temperature superconductors (superconductivity), 1980. https://www.pnas.org.

[68] I. Shirotani, M. Takaya, I. Kaneko, C. Sekine, T. Yagi, Superconductivity of MRuP and MNiP (M=Mo or W) prepared at high pressure, Solid State Commun 116 (2000) 683–686. https://doi.org/10.1016/S0038-1098(00)00393-8.

[69] J. Kolny-Olesiak, Recent Advances in the Colloidal Synthesis of Ternary Transition Metal Phosphides, Zeitschrift Fur Naturforschung - Section A Journal of Physical Sciences 74 (2019) 709–719. https://doi.org/10.1515/zna-2019-0133.

[70] G. Li, Y. Feng, Y. Yang, X. Wu, X. Song, L. Tan, Recent advances in transition metal phosphide materials: Synthesis and applications in supercapacitors, Nano Materials

Science (2023). https://doi.org/10.1016/j.nanoms.2023.03.003.

[71] J.H. Pöhls, A. Faghaninia, G. Petretto, U. Aydemir, F. Ricci, G. Li, M. Wood, S. Ohno, G. Hautier, G.J. Snyder, G.M. Rignanese, A. Jain, M.A. White, Metal phosphides as potential thermoelectric materials, J Mater Chem C Mater 5 (2017) 12441–12456. https://doi.org/10.1039/c7tc03948d.

[72] D.C.S. Souza, V. Pralong, A.J. Jacobson, L.F. Nazar, A Reversible Solid-State Crystalline Transformation in a Metal Phosphide Induced by Redox Chemistry, Science (1979) 296 (2002) 2012–2015. https://doi.org/10.1126/science.1071079.

[73] V. Pralong, D.C.S. Souza, K.T. Leung, L.F. Nazar, Reversible lithium uptake by CoP3 at low potential: role of the anion, Electrochem Commun 4 (2002) 516–520. https://doi.org/10.1016/S1388-2481(02)00363-6.

[74] S. Fiechter, H. Tributsch, M. Evain, R. Brec, γ-FeP4, a new photosensitive semiconductor, Mater Res Bull 22 (1987) 543–549. https://doi.org/10.1016/0025-5408(87)90266-2.

[75] Y. Xie, H.L. Su, X.F. Qian, X.M. Liu, Y.T. Qian, A Mild One-Step Solvothermal Route to Metal Phosphides (Metal=Co, Ni, Cu), J Solid State Chem 149 (2000) 88–91. https://doi.org/10.1006/jssc.1999.8499.

[76] R. Rühl, W. Jeitschko, Stacking variants of MnP4: preparation and structure of 6-MnP4, Acta Crystallogr B 37 (1981) 39–44. https://doi.org/10.1107/s056774088100215x.

[77] U. Flörke, W. Jeitschko, Preparation and properties of new modifications of RuP4 and

OsP4 with CdP4-type structure, Journal of the Less Common Metals 86 (1982) 247–253. https://doi.org/10.1016/0022-5088(82)90210-7.

[78] W. Jeitschko, P.C. Donohue, The high pressure synthesis, crystal structure, and properties of CrP4 and MoP4, Acta Crystallogr B 28 (1972) 1893–1898. https://doi.org/10.1107/s0567740872005187.

[79] E. Clementi, D.L. Raimondi, W.P. Reinhardt, Atomic Screening Constants from SCF Functions. II. Atoms with 37 to 86 Electrons, J Chem Phys 47 (1967) 1300–1307. https://doi.org/10.1063/1.1712084.

[80] R. Kanno, N. Kinomura, M. Koizumi, High Pressure Synthesis of VP4, in: High Pressure Science and Technology : Proceedings of the 7th International AIRAPT Conference : (Organised Jointly with the EHPRG), Le Creusot, France, July 30-August 3, 1979 / Edited by B. Vodar and Ph. Marteau, Vol.1, Pergamon Press, 1979: pp. 583–584.

[81] W. Jeitschko, U. Flörke, U.D. Scholz, Ambient pressure synthesis, properties, and structure refinements of VP4 and CoP2, J Solid State Chem 52 (1984) 320–326. https://doi.org/10.1016/0022-4596(84)90015-X.

[82] C. Li, X. Liu, Z. Yu, W. Wu, L. Zhang, C. Zhou, J. Zhao, Y. Guo, J. Luo, The Remarkable Anisotropic Compressibility and Metallic Cr-Cr Chains in Topological Semimetal CrP4 under High Pressure, Phys Status Solidi B Basic Res 258 (2021) 1–5. https://doi.org/10.1002/pssb.202000544.

[83] A.H. Mayo, J.A. Richards, H. Takahashi, S. Ishiwata, High-pressure synthesis of a massive and non-symmorphic Dirac semimetal candidate MoP4, J Physical Soc Japan 90 (2021) 1–5. https://doi.org/10.7566/JPSJ.90.123704.

[84] C.-C. Chang, T. Sasaki, N.A. Gaida, K. Niwa, M. Hasegawa, High-pressure synthesis and low-temperature thermal expansion behavior of homogeneous phosphorus-rich pseudo-binary compound (V0.5Cr0.5)P4, Ceram Int 49 (2023) 40990–40994. https://doi.org/10.1016/j.ceramint.2023.09.176.